UNIVERSITY OF WARMIA AND MAZURY IN OLSZTYN

Technical Sciences

23(1) 2020

OLSZTYN 2020

Editorial Board

Ceslovas Aksamitauskas (Vilnius Gediminas Technical Univetsity, Lithuania), Olivier Bock (Institut National de L'Information Géographique et Forestiére, France), Stefan Cenkowski (University of Manitoba, Canada), Adam Chrzanowski (University of New Brunswick, Canada), Davide Ciucci (University of Milan-Bicocca, Italy), Sakamon Devahastin (King Mongkut's University of Technology Thonburi in Bangkok, Thailand), German Efremov (Moscow Open State University, Russia), Mariusz Figurski (Military University of Technology, Poland), Maorong Ge (Helmholtz--Zentrum Potsdam Deutsches GeoForschungsZentrum, Germany), Dorota Grejner-Brzezinska (The Ohio State University, USA), Janusz Laskowski (University of Life Sciences in Lublin, Poland), Arnold Norkus (Vilnius Gediminas Technical University, Lithuania), Stanisław Pabis (Warsaw University of Life Sciences-SGGW, Poland), Lech Tadeusz Polkowski (Polish-Japanese Institute of Information Technology, Poland), Arris Tijsseling (Technische Universiteit Eindhoven, Netherlands), Vladimir Tilipalov (Kaliningrad State Technical University, Russia), Alojzy Wasilewski (Koszalin University of Technology, Poland)

Editorial Committee

Marek Markowski (Editor-in-Chief), Piotr Artiemjew, Kamil Kowalczyk, Wojciech Sobieski, Piotr Srokosz, Magdalena Zielińska (Assistant Editor), Marcin Zieliński

Features Editors

Piotr Artiemjew (Information Technology), Marcin Dębowski (Environmental Engineering), Zdzisław Kaliniewicz (Biosystems Engineering), Grzegorz Królczyk (Materials Engineering), Marek Mróz (Geodesy and Cartography), Ryszard Myhan (Safety Engineering), Wojciech Sobieski (Mechanical Engineering), Piotr Srokosz (Civil Engineering), Jędrzej Trajer (Production Engineering)

Statistical Editor
Paweł Drozda

Executive Editor
Mariola Jezierska

The Technical Sciences is indexed and abstracted in BazTech (http://baztech.icm.edu.pl) and in IC Journal Master List (http://journals.indexcopernicus.com)

The Journal is available in electronic form on the web sites
http://www.uwm.edu.pl/techsci (subpage Issues)
http://wydawnictwo.uwm.edu.pl (subpage Czytelnia)

The electronic edition is the primary version of the Journal

PL ISSN 1505-4675
e-ISSN 2083-4527

© Copyright by Wydawnictwo UWM ● Olsztyn 2020

Address
ul. Jana Heweliusza 14
10-718 Olsztyn-Kortowo, Poland
tel.: +48 89 523 36 61
fax: +48 89 523 34 38
e-mail: wydawca@uwm.edu.pl

Ark. wyd. 8,3, ark. druk. 7,0, nakład 75 egz.
Druk – Zakład Poligraficzny UWM, zam. 164

Contents

Technical Sciences, 2020, 23(1), 5–23

UNIWERSYTET WARMIŃSKO-MAZURSKI W OLSZTYNIE

Quarterly peer-reviewed scientific journal
ISSN 1505-4675
e-ISSN 2083-4527
TECHNICAL SCIENCES
Homepage: www.uwm.edu.pl/techsci/

doi: 10.31648/ts.5331

ANALYSIS OF HARMONIC REDUCTION METHODS FOR TRANSFORMER SUBSTATIONS

***Szymon Racewicz*[1], *Mateusz Rokicki*[2]**

[1]ORCID: 0000-0002-3426-9767
Department of Mechatronics and Technical-Computer Sciences Education
University of Warmia and Mazury in Olsztyn
[2]ORCID: 0000-0002-7604-8612
Maintenance Department
Michelin Polska SA, Olsztyn

Received 7 October 2019, accepted 20 February 2020, available online 9 March 2020.

K e y w o r d s: harmonic reduction; active filters; THD coefficient.

A b s t r a c t

This article presents an analysis of harmonic levels and methods for reducing harmonics in one of Michelin transformer substations. The electrical network in the substation consists of two transformers (1.6 MVA and 2.0 MVA) supplying a production line composed of several electrical devices using DC and AC motors. The influence of harmonic levels on substation operation was investigated by measuring the current and the load factors of the powered machines as well as coefficients THD_u, THD_i, D_u and D_i with the use of the Fluke 435II 3-phase energy quality analyzer and the PEL103 network parameter recorder. Based on the results of the measurements, four harmonic reduction methods (passive filters, active filters, 12-pulse rectifier and the Active Front End system) were proposed and tested in the study. The electrical network of the substation was modeled using Emerson Harmonics Estimator software. A financial analysis of potential investments was performed to select the optimal solution.

Correspondence: Szymon Racewicz, Katedra Mechatroniki i Edukacji Techniczno-Informatycznej, Wydział Nauk Technicznych, Uniwersytet Warmińsko-Mazurski, ul. Oczapowskiego 11, 10-719 Olsztyn, e-mail: szymon.racewicz@uwm.edu.pl

Introduction

Higher harmonics of voltages and currents are among the main disturbances occurring in electric power systems. They appear in power grids due to the constantly increasing number of electrical equipment with nonlinear characteristics and at the same time due to the decreasing tendency of resistive devices share (HANZELKA 2001). Even if a unit power of the device installed in the network is small like for example for lighting installations, the considering number of such devices can significantly decrease energy quality in the network by increasing the content of higher harmonics. Then low quality of the energy influences on other equipment present in the network (GIRGIS et al. 1992). For the last few decades the knowledge about the problems associated with harmonics has been improved significantly (MAZIN et al. 2011, HU et al. 2018, SHARMA et al. 2016, MOTTA, FAÚNDES 2016, VIVEK et al. 2016). Nevertheless, it allows us only to reduce the threats rather than to completely eliminate them.

This article is focused on the optimal selection of the higher harmonic reduction method for the P50 transformer substation operating in the Michelin tire factory in Olsztyn, in terms of the cost-performance ratio. The harmonic tests in the P50 substation have been carried out due to the substation self-ignition and fire, which took place in 2016. However, it was not a single case concerning only Poland. This problem was also identified in other company factories. It was presumed and then proved that the direct cause of the substations fires had been related to the exceed of the acceptable harmonic levels described in the standards PN-EN 50160: 2010 and PN-EN 61000-4-30: 2011. In the described case the long term higher harmonic presence in the network damaged and decreased the capacitance of certain capacitors used for reactive power compensation what resulted in a sudden reactive power rise and an overheat of the installation.

Fig. 1. Temperature of power contactor installed in capacitor bank

This hypothesis was also confirmed by the thermovision measurements which showed the increased current consumption flowing through the power contactors installed in the capacitor bank (Fig. 1). In order to improve the safety and to guarantee the substation reliability the level of higher harmonics present in the substation network was reduced significantly. For this purpose and in order to choose the best filtration method a number of measurements and tests have been carried out.

The efficiency of the filtration method has been evaluated by measuring certain coefficients like: the ratio of the n^{th} harmonic to the fundamental harmonics for voltage and current (D_u, D_i) given by equations 1 and 2 as well as the quotient of the harmonic effective value to the effective value of the fundamental harmonic for voltage and current (THD_u, THD_i) given by equations 3 and 4 (ARRILLAGA et al. 1985, HORSKA et al. 2014).

$$D_{u(n)} = \frac{U_{rms(n)}}{U_{rms(1)}} \cdot 100\% \tag{1}$$

$$D_{i(n)} = \frac{I_{rms(n)}}{I_{rms(1)}} \cdot 100\% \tag{2}$$

$$\text{THD}_u = \frac{\sqrt{\sum_{n=2}^{\infty} U_{(n)}^2}}{U_{(1)}} \cdot 100\% \tag{3}$$

$$\text{THD}_i = \frac{\sqrt{\sum_{n=2}^{\infty} I_{(n)}^2}}{I_{(1)}} \cdot 100\% \tag{4}$$

Practically, the upper limit of the summation in equations (3) and (4) is taken as $n = 50$ or even $n = 25$ when the risk of resonance for higher harmonics is small. Table 1. presents the limit values for individual voltage harmonics according to EN50160 and IEC61000 standards (ŻABICKI 2017, SAKTHIVEL et al. 2003). The limit values for individual current harmonics has been presented in (STEIN, ZIELIŃSKA 2016). According to the standards the limit for THD_u is 5% for medium voltage network and 8% for low voltage network. It should be also noted that the coefficients THD_u and THD_i give only an overall image of the harmonics present in the network what sometimes can lead to misinterpretation of the measurements results especially when the measurements are carried out during partial load of the network (Fig. 2). Therefore, it is then necessary to carry out the complete measurements including the equipment load analysis (HANZELKA 2001, KHADEM et al. 2015, GUPTA et al. 2015).

Table 1

Limit values for individual voltage harmonics according to EN50160 and IEC61000 standards

Odd harmonics				Even harmonics	
Not a multiplicity of 3		multiplicity of 3			
Order	amplitude [%]	order	amplitude [%]	order	amplitude [%]
5	6	3	5	2	2
7	5	9	1.5	4	1
11	3.5	15	0.5	6	0.5
13	3	21	0.5	8	0.5
17	2	–	–	10	0.5
19	1.5	–	–	12	0.5
23	1.5	–	–	14	0.5
25	1.5	–	–	16	0.5
–	–	–	–	18	0.5
–	–	–	–	20	0.5
–	–	–	–	22	0.5
–	–	–	–	24	0.5

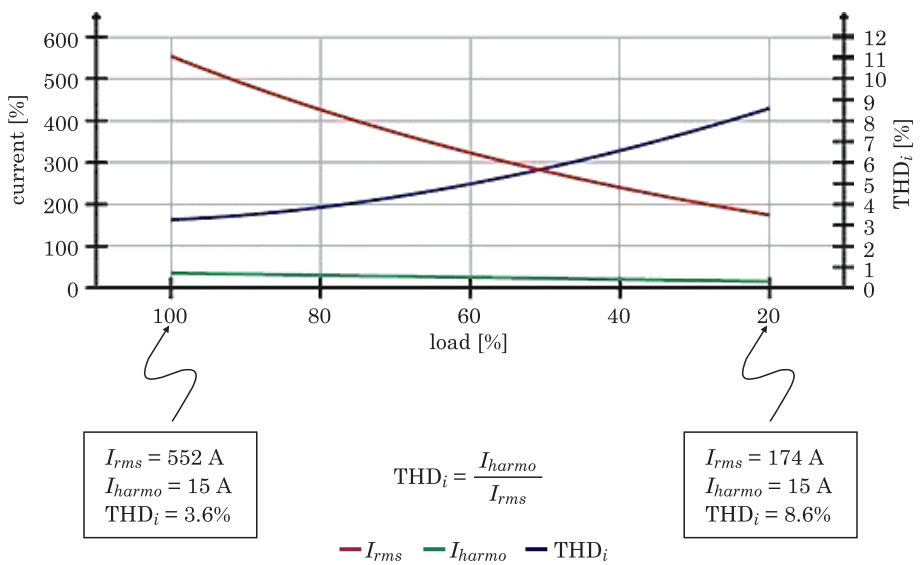

Fig. 2. Variation of THD$_i$ value for different loads

Research object

The P50 substation consists of two transformers (TR1 and TR2) which powers are 2 MVA and 1.6 MVA respectively. It supplies the extrusion line P01 which serves to mix three components to obtain a product for a tire tread as well as to reuse its own returns. The P01 line consists of: three extruders cold fed (supplied by the TR1) and heating rolling mill, plasticizer and extruder NAR1200 (supplied by the TR2). All of devices are driven by DC and AC motors of 2184 kW total power. The P01 line has been designed for continuous operation. Schematic of the P50 substation electrical network has been shown in Figure 3. In the network schematic the two capacitor banks C1 and C2 as well as other electric receivers (lighting, control systems, etc.) modeled by L1 and L2 have been shown.

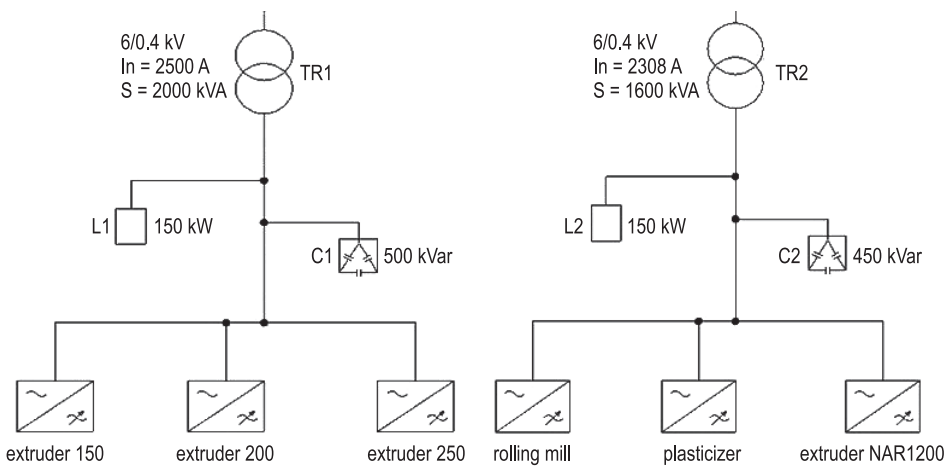

Fig. 3. Schematic of P50 transformer substation electrical network

Figure 4 shows currents consumed by the equipment installed in the P01 extrusion line. Taking into consideration the nominal values of the equipment motor currents one can calculate that the average load factor of the devices is not exceeding 50%. The load factor is closely related to the assortment currently produced by the extrusion line what in consequence causes variation of the THD coefficients. Therefore, the continuous monitoring of higher harmonic present in electric network is necessary.

The following figures (Figs. 5, 6, 7, 8) show courses of the coefficients THD_u, and THD_i captured for the extruder 150 during the test which has been carried out for two weeks as well as the values of the coefficients D_u, and D_i for subsequent odd harmonics up to 30^{th} picked for one of the stable operating state.

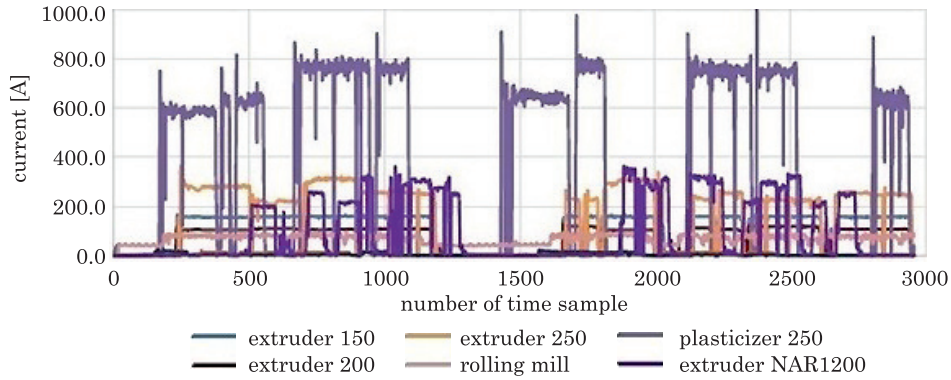

Fig. 4. Current consumed by the P01 line equipment (time sample ≈ 6.5 min)

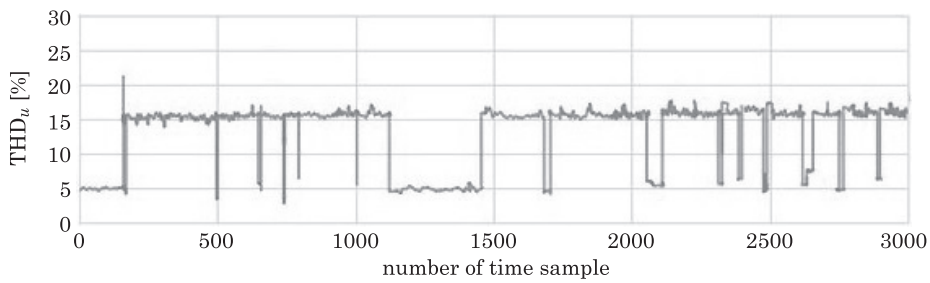

Fig. 5. Course of the THD$_u$ coefficient captured for the extruder 150 during two-week test without higher harmonics filtration (time sample ≈ 6.5 min)

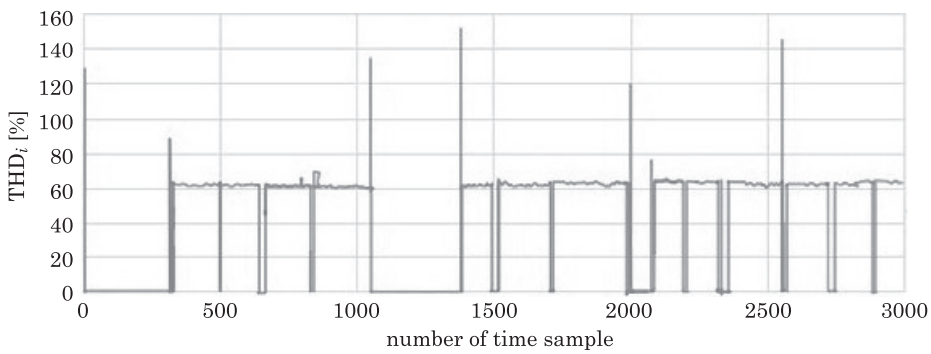

Fig. 6. Course of the THD$_i$ coefficient captured for the extruder 150 during two-week test without higher harmonics filtration (time sample ≈ 6.5 min)

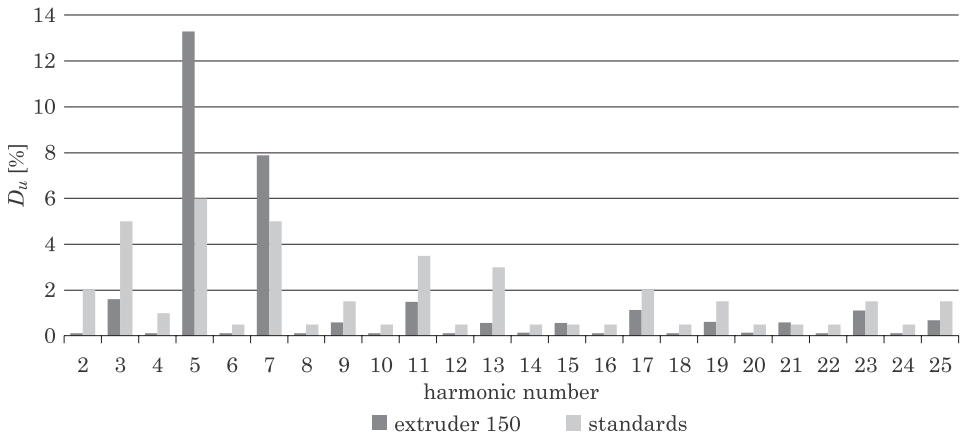

Fig. 7. Values of subsequent voltage harmonics produced by extruder 150 without higher harmonics filtration

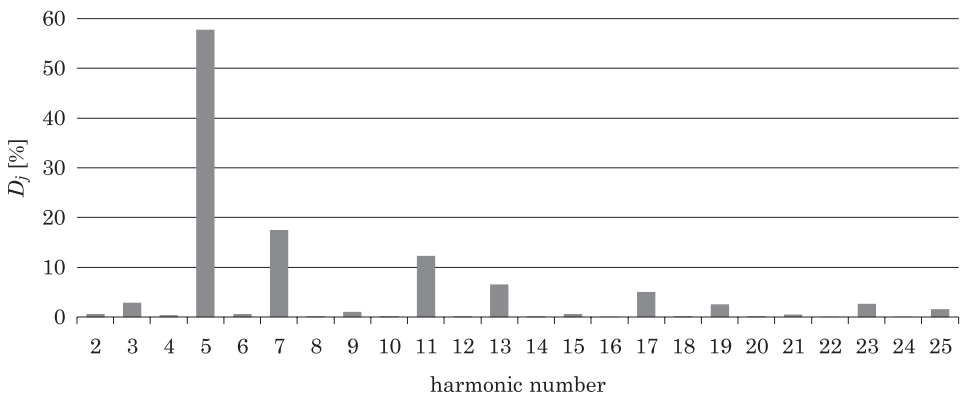

Fig. 8. Values of subsequent current harmonics produced by extruder 150 without higher harmonics filtration

Presented measurements have been performed using the 3-phase energy quality analyzer Fluke 435II with the i430-Flex current clamp and the network parameter recorder PEL103 Chauvin Arnoux. The energy quality analyzer Fluke 435II averages measurements every 6.5 minutes what gives one value sample. The maximum number of samples which can be recorded is 3000 what gives about 2 weeks of network parameters monitoring. Measurements carried out for the other devices installed in the P50 substation electrical network have also confirmed a similar over normed higher harmonics production what has had a destructive influence on the capacitor banks used for reactive power compensation. The spikes of the THD_i coefficient observed in the Figure 6 are related to the moments of turning the extruder 150 on while processing heavier assortment.

Simulation results

The evaluation of filtration quality for four types of solutions (passive filters, active filters, 12-pulse rectifiers, AFE) has been carried out using the predefined models available in the Emerson Harmonics Estimator simulation software. The measured machines loads have been introduced into the Emerson software individually for each machine as a percentage of nominal machine load. Simulation results have served to predict the potential level of higher harmonics presented at the secondary side of the transformers for different methods of harmonics reduction and to compare the methods with each other.

Passive filters

One of the most economical methods for limiting the negative influence of the electric drives present in the network is the use of passive filters which are individually designed for the particular type of drive and installed on the power supply side (RAJESHWARI, BAGWARI 2018, GADEKAR et al. 2016, BAITHA, GUPTA 2015). They are designed taking into account the nominal current of the drive. Their efficiency is high provided that they are installed close to the drive working with its nominal power for which the filter has been designed. The effectiveness of the passive filter (DC choke) depending on the machine load has been presented in Figure 9.

Figure 10 shows schematic of the P50 transformer substation electrical network equipped with passive filters (F1–F6) used for Emerson Harmonics Estimator software simulation. Simulation results have been presented in Figures 11 and 12.

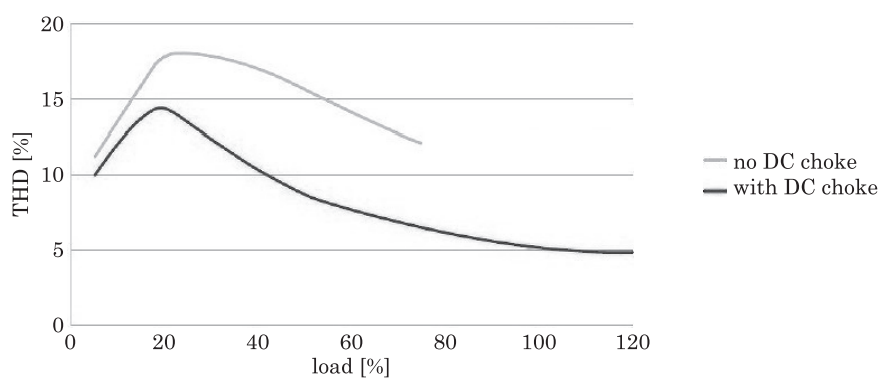

Fig. 9. Passive filter effectiveness depending on the machine load

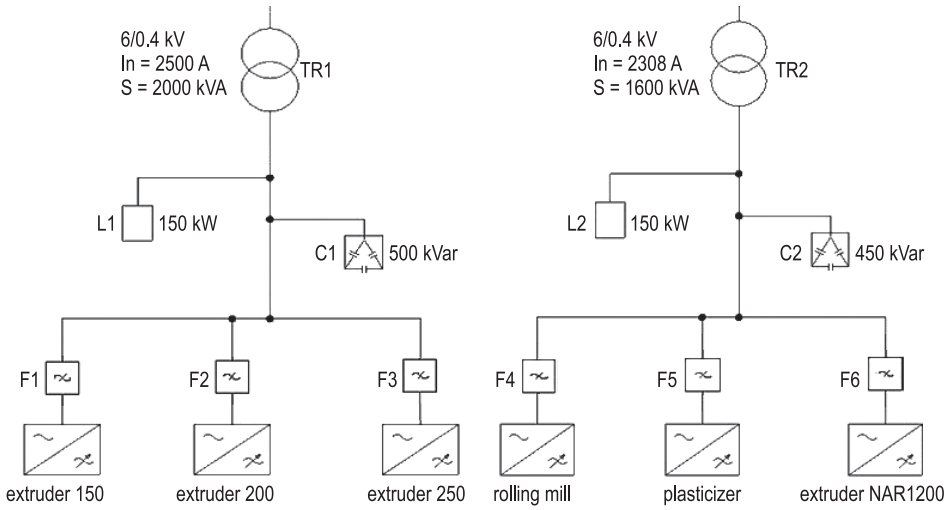

Fig. 10. Schematic of P50 transformer substation electrical network with passive filters

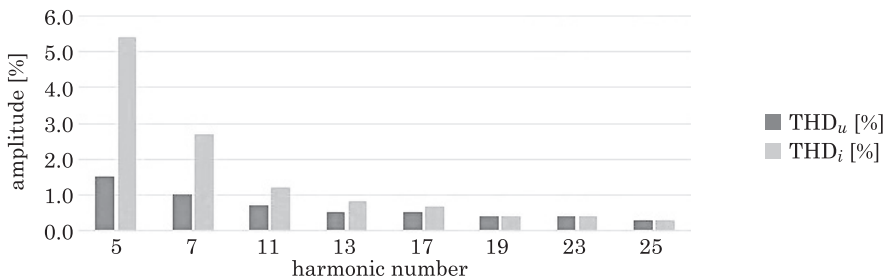

Fig. 11. Harmonic level estimation for transformer TR1 secondary side after passive filters application

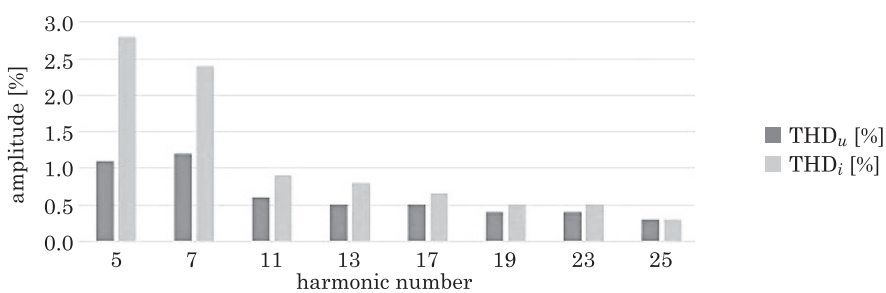

Fig. 12. Harmonic level estimation for transformer TR2 secondary side after passive filters application

Active filters

Active filters reduce the higher harmonics in electrical network by generating those harmonics which are consumed by nonlinear receivers (KARVE 2016, IZHAR et al. 2004, YARAHMADI et al. 2013). For example, if the receiver needs the fifth and seventh harmonics the active filter generates them what results in more sinusoidal shape of the network current.

Figure 13 shows schematic of the P50 transformer substation electrical network equipped with active filters (Active filter 1 and 2) used for Emerson Harmonics Estimator software simulation. Simulation results have been presented in Figures 14 and 15.

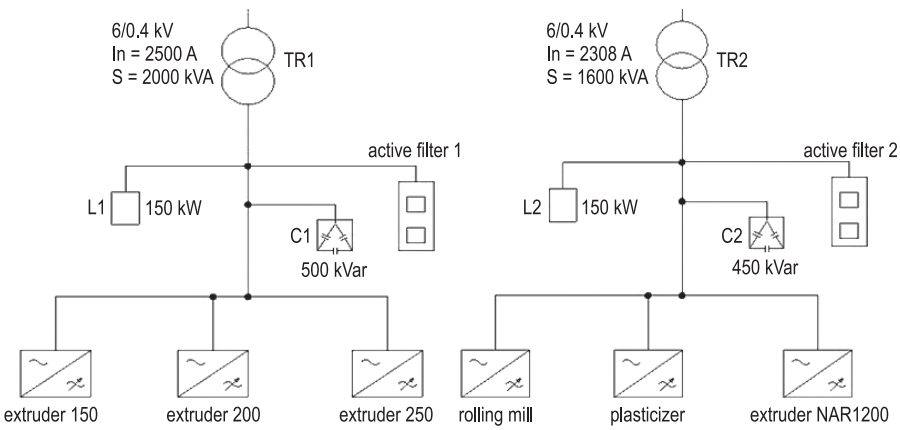

Fig. 13. Schematic of P50 transformer substation electrical network with active filters

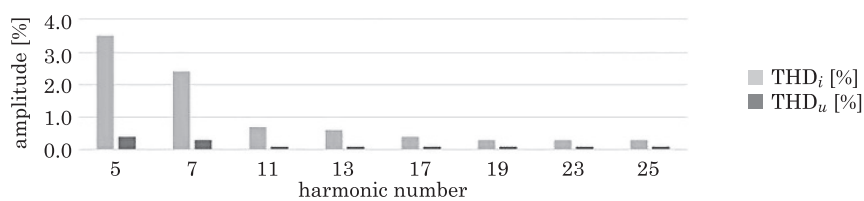

Fig. 14. Harmonic level estimation for transformer TR1 secondary side after active filters application

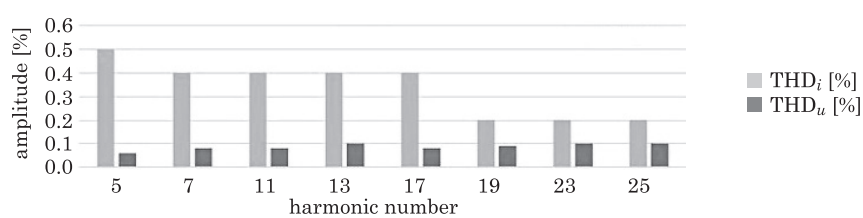

Fig. 15. Harmonic level estimation for transformer TR2 secondary side after active filters application

12-pulse rectifier

Multi-pulse rectifiers have been known for many years as the devices which minimize the higher harmonics generated by drive systems (KOCMAN et al. 2010, KIMET et al. 2019). According to the theory the multi-pulse rectifiers exclude certain harmonics due to the phase shift between the transformer windings (IWASZKIEWICZ et al. 2019, MYSIAK 2007). Increasing a number of secondary winding phases can be achieved in several ways but the simplest is to use a triangle-star system in which the number of secondary winding phases is 6. After rectification by two parallel rectifier system one can obtain a DC voltage.

Figure 16 shows schematic of the P50 transformer substation electrical network equipped with 12-pulse rectifier (R1–R6) used for Emerson Harmonics Estimator software simulation. Simulation results have been presented in Figures 17 and 18.

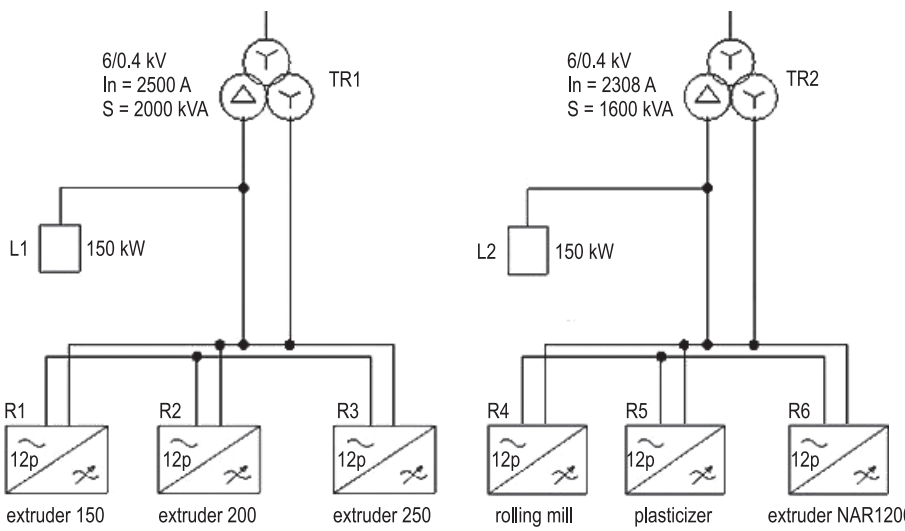

Fig. 16. Schematic of P50 transformer substation electrical network with 12-pulse rectifiers

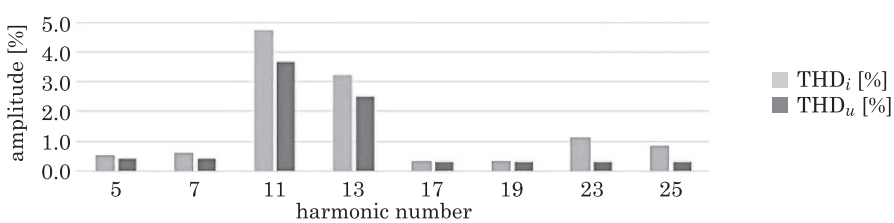

Fig. 17. Harmonic level estimation for transformer TR1 secondary side after 12-pulse rectifiers application

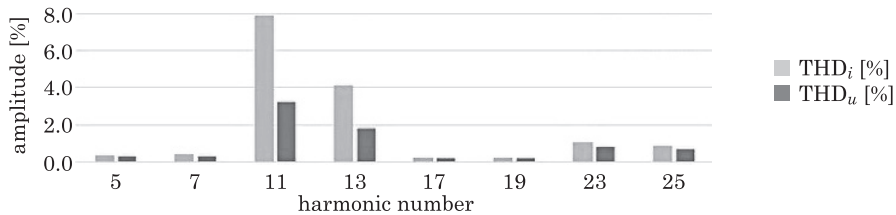

Fig. 18. Harmonic level estimation for transformer TR2 secondary side after 12-pulse rectifiers application

Active Front End

The AFE (Active Front End) technology is a solution which guarantees a very low THD coefficient (SALGADO-HERRERA et al. 2018, RODRÍGUEZ et al. 2004, ESPINOSA et al. 2014). It comprises a fully controlled IGBT transistor input bridge which is used as a supplementary converter called a regenerative drive. It has an energy return function. The inverter design includes then two separate power modules – motoring drive and regenerative drive – connected together by a common DC bus with a LCL network filter. Unfortunately, the cost of implementation of such solution is very high in a situation where the modernized electrical network consists in majority of DC drives as the AFE converters use only frequency speed control dedicated for AC drives. The one AFE can be also used for several different drives connected by a common DC bus as shown in Figure 19 but in the studied case an installation of the DC bus has been impossible due to lack of space.

Figure 20 shows schematic of the P50 transformer substation electrical network equipped with AFE systems (AFE1–AFE6) used for Emerson Harmonics Estimator software simulation. Simulation results have been presented in Figures 21 and 22.

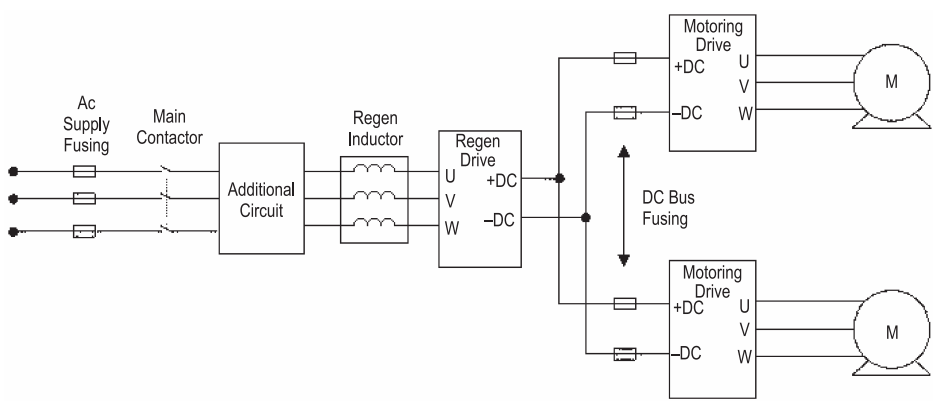

Fig. 19. Schematic of the AFE network with DC bus circuit for many machines

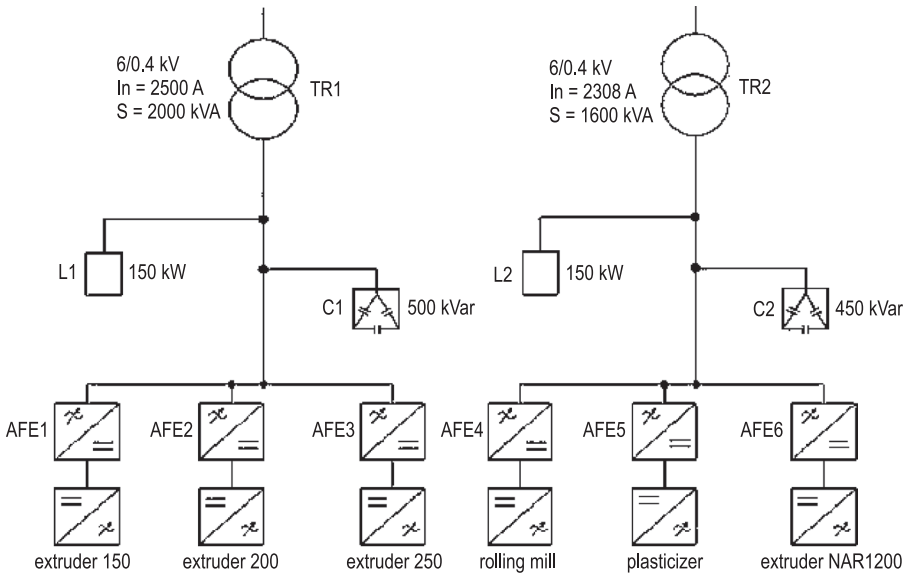

Fig. 20. Schematic of P50 transformer substation electrical network with AFE system

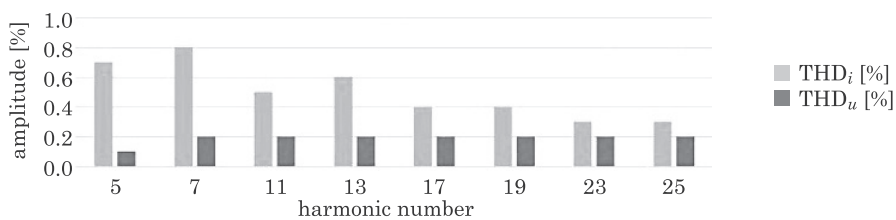

Fig. 21. Harmonic level estimation for transformer TR1 secondary side after AFE system application

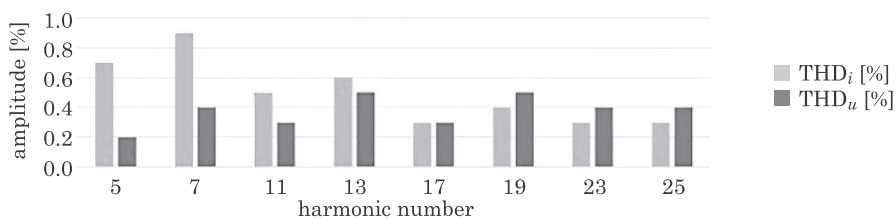

Fig. 22. Harmonic level estimation for transformer TR2 secondary side after AFE system application

Discussion of the results

Comparing the simulation results one can observe that the best quality of higher harmonic filtration is realized by the AFE system where all higher harmonics values have been reduced to below 1% (Figs. 21, 22). It is also the more expensive solution valued at 442 500 € what is mainly associated with the need to replace the DC motors by the AC motors. The second more expensive filtration method is the use of the 12-pulse rectifiers which also need some equipment replacement. It is valued at 300 000 € because of the need to replace the two of transformers (TR1 and TR2) by the ones with two secondary windings connected in star and triangle. The filtration quality is acceptable for the fifth and the seventh harmonics. Nevertheless, for the studied case the simulations have revealed also the presence of the eleventh and the thirteenth harmonics what is not favorable for the condition of the network (Figs. 17, 18). The least expensive solution for the higher harmonic filtration is the use of passive filters valued at 44 990 €. The main disadvantage of this method is related to an inability to adapt to the changing network conditions present in the P01 extrusion production line. Moreover, the filtration quality is several times lower than for the other methods (Figs. 11, 12). The last studied method, i.e. active filters ensures effective higher harmonics reduction (Figs. 14, 15) at a relatively low cost of investment (135 000 €).

All of above mentioned methods with their implementation cost and the filtration quality analysis for the fifth and the seventh harmonics have been collected in the Table 2 and compared in the Figures 23 and 24. The filtration quality has been presented in the Table 2 as the THD coefficient values respectively for voltage and current.

Finally, after above mentioned analysis the active filter technology has been chosen for the P01 extrusion line. More precisely, the active filters AccuSine PCS – Power Correction system – Model CE54 – Sizes 300A have been installed in the TR1 and the TR2 networks. More detailed information about the filters can be found in the technical documentation (*AccuSine* ® *Power* Correction… 2012). The active filter implementation has resulted in considerable higher harmonic reduction. Figures 25, 26, 27 and 28 show the measurements results of the THD_u, THD_i, D_u and D_i coefficients captured for the extruder 150 after the filters installation. In comparison to the Figures 5, 6, 7 and 8 one can observe the THD_u reduction from more than 15% to about 5% and the THD_i reduction from more than 60% to about 30%. Regarding D_u and D_i coefficients, particularly important is reduction of the 5^{th} and the 7^{th} harmonics which exceeded standard limits before filtration implementation.

Table 2

Comparison of implementation costs and filtration quality for various higher harmonic filtration methods

Transformer	TR1		TR2		Implementation cost [€]
Harmonics (THD) voltage/current [%]	5	7	5	7	
Without filtration	5.6/14.2	3.8/9.9	7.7/24.3	6.6/16.8	0
Passive filters	1.5/5.4	1/2.7	1.4/10	1.3/6.5	44 990
Active filters	0.4/3.5	0.3/2.4	0.06/0.5	0.08/0.4	135 000
12-pulse rectifier	0.4/0.5	0.4/0.6	0.25/0.3	0.25/0.4	300 000
AFE (Active Front End)	0.1/0.7	0.2/0.8	0.2/0.7	0.4/0.9	442 500

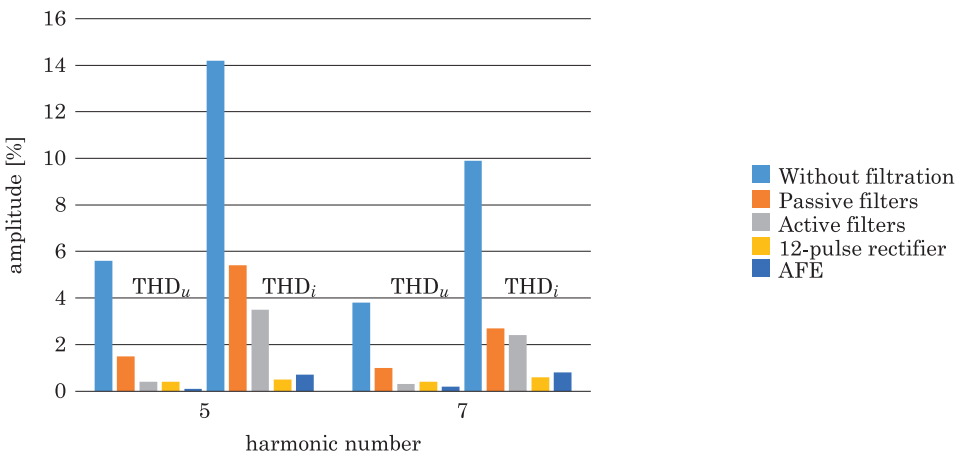

Fig. 23. Comparison of different methods filtration quality for transformer TR1 network

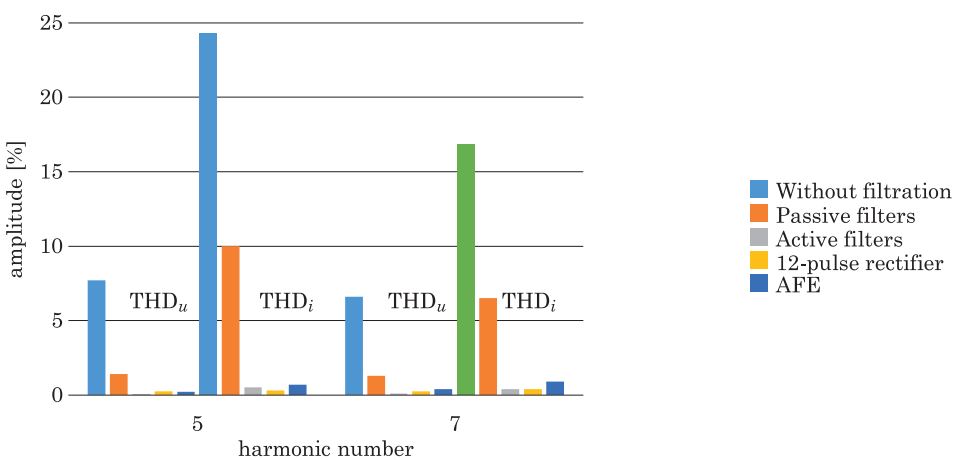

Fig. 24. Comparison of different methods filtration quality for transformer TR2 network

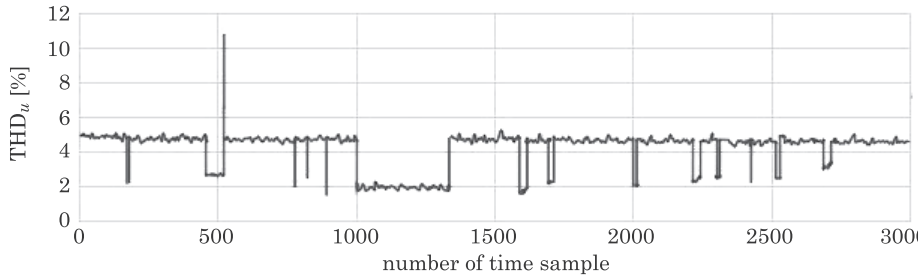

Fig. 25. Course of the THD$_u$ coefficient captured for the extruder 150 during two-week test with higher harmonics active filtration (time sample ≈ 6.5 min)

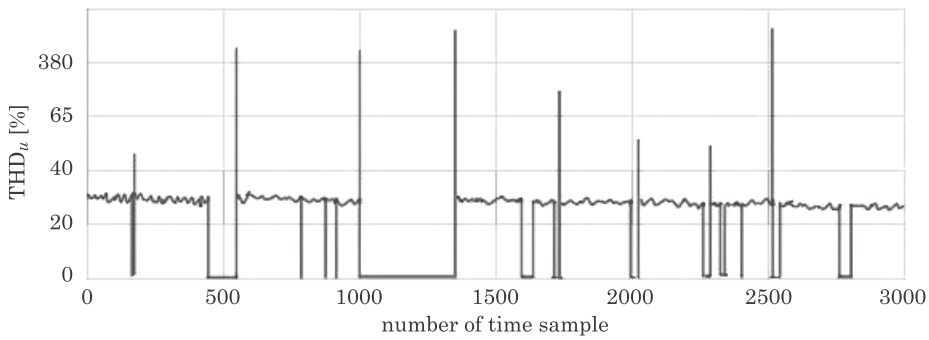

Fig. 26. Course of the THD$_i$ coefficient captured for the extruder 150 during two-week test with higher harmonics active filtration (time sample ≈ 6.5 min)

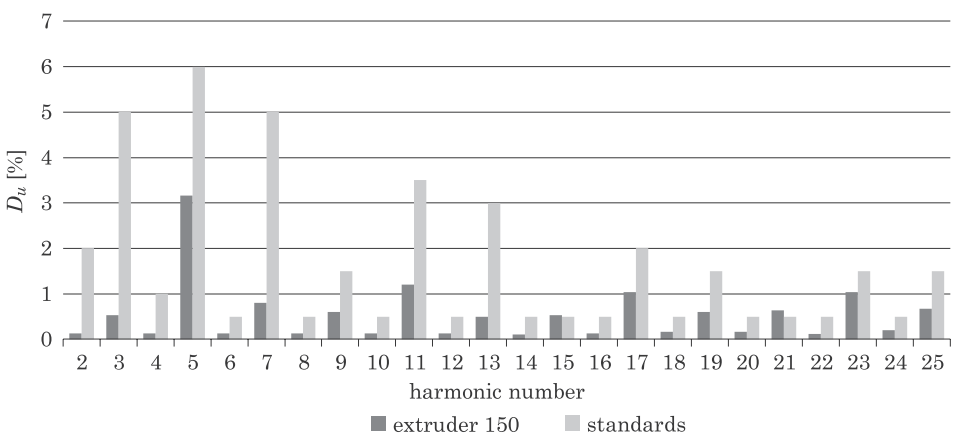

Fig. 27. Values of subsequent voltage harmonics produced by extruder 150 with higher harmonics active filtration

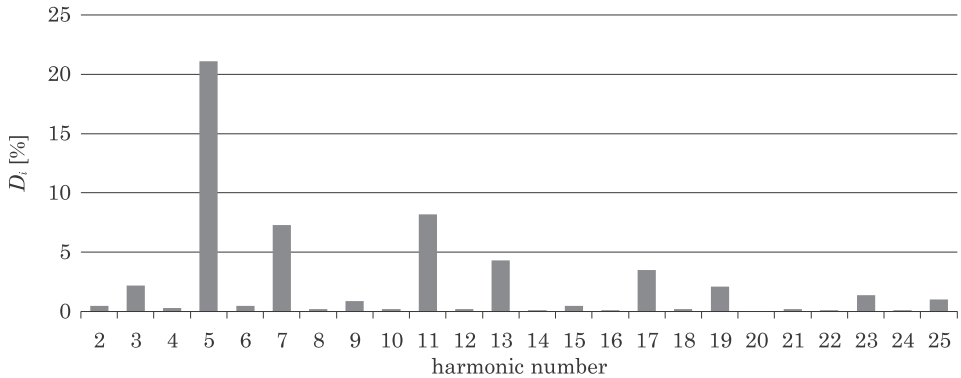

Fig. 28. Values of subsequent current harmonics produced by extruder 150 with higher harmonics active filtration

Conclusions

In the article the problem of higher harmonics presence in one of the transformer substation electrical network in the Michelin tire factory has been investigated. Increased reactive power consumption and a high temperature in the capacitor bank have led to the supposition that the capacitors have been successively damaged by the higher harmonics present in the network for a long time. This situation has finally resulted in the substation fire which took place in 2016. To prevent such situations in the future the series of measurements and tests have been carried out in order to apply the best higher harmonics filtration method.

The measurements have showed some exceeds of the permissible levels of the coefficients D_u, D_i, THD_u, and THD_i for individual devices while producing certain assortment of tire components. The simulations carried out in Emerson Harmonics Estymator software for four types of harmonics reduction methods (passive filters, active filters, 12-pulse rectifier and the AFE) have showed the potential possibilities and effectiveness of these solutions. After financial analysis of each solution implementation cost the active filtration has been proposed and implemented in P50 transformer substation what has reduced significantly the higher harmonics values (Figs. 25 and 26 in comparison to Figs. 5 and 6) and has improved the capacitor banks operating conditions. The temperature of the power contactors installed in the capacitor banks has been reduced from about 89.4°C-101.8°C to about 50,8°C-74,3°C depending on power contactor group and actual production.

References

ARRILLAGA J., BRADLEY D.A., BODGER P.S. 1985. *Power System Harmonics*. John Wiley. https://books.google.pl/books/about/Power_system_harmonics.html?id=st1SAAAAMAAJ&redir_esc=y.

BAITHA A., GUPTA N. 2015. *A Comparative Analysis of Passive Filters for Power Quality Improvement*. Proceedings of IEEE International Conference on Technological Advancements in Power and Energy, TAP Energy, p. 327–332. Institute of Electrical and Electronics Engineers Inc. https://doi.org/10.1109/TAPENERGY.2015.7229640.

ESPINOSA E., ESPINOZA J., ROHTEN J., RAMIREZ R., REYES M., MUNOZ J., MELIN P. 2014. *An Efficiency Comparison between a 18 Pulses Diode Rectifier and a Multi-Cell AFE Rectifier Operating with FCS – MPC*. IECON Proceedings (Industrial Electronics Conference), p. 1214–1220. Institute of Electrical and Electronics Engineers Inc. https://doi.org/10.1109/IECON.2014.7048657.

GADEKAR S., KULKARNI N., MHETRE S., KULKARNI H.H. 2016. *Design and Development of Passive Filter and Comparative Study of Simulation Results of Passive and Active Filter*. International Conference on Energy Systems and Applications, ICESA, p. 324–328. Institute of Electrical and Electronics Engineers Inc. https://doi.org/10.1109/ICESA.2015.7503364.

GIRGIS A.A., NIMS J.W., JACOMINO J., DALTON J.G., BISHOP A. 1992. *Effect of Voltage Harmonics on the Operation of Solid-State Relays in Industrial Applications*. IEEE Transactions on Industry Applications, 28(5): 1166–1173. https://doi.org/10.1109/28.158844.

GUPTA C., VARSHNEY A., VERMA N., SHUKLA S. 2015. *THD Analysis of Eleven Level Cascaded H-Bridge Multilevel Inverter with Different Types of Load Using in Drives Applications*. Proceedings – 2015 2nd IEEE International Conference on Advances in Computing and Communication Engineering, ICACCE, p. 355–359. Institute of Electrical and Electronics Engineers Inc. https://doi.org/10.1109/ICACCE.2015.61.

HANZELKA Z. 2001. *Jakość energii elektrycznej*. Część 4. *Wyższe harmoniczne napięć i prądów*. Elektroinstalator, 12: 1–31. http://twelvee.com.pl/pdf/Hanzelka/cz_4_pelna.pdf (access: 27.05.2019).

HORSKA J., MASLAN S., STREIT J., SIRA M. 2014. *A Validation of a THD Measurement Equipment with a 24-Bit Digitizer*. CPEM Digest (Conference on Precision Electromagnetic Measurements), p. 502–503. Institute of Electrical and Electronics Engineers Inc. https://doi.org/10.1109/CPEM.2014.6898479.

HU H., SHAO Y., TANG L., MA J., HE Z., GAO S. 2018. *Overview of Harmonic and Resonance in Railway Electrification Systems*. IEEE Transactions on Industry Applications, 54(5): 5227–5245. https://doi.org/10.1109/TIA.2018.2813967.

IWASZKIEWICZ J., MUC A., MYSIAK P. 2019. *A 12-Pulse Rectifier Using Coupled Reactors for Supplying Three-Inverters*. Renewable Energy and Power Quality Journal, 17: 589–592. https://doi.org/10.24084/repqj17.382.

IZHAR M., HADZER C.M., SYAFRUDIN M., TAIB S., IDRIS S. 2004. *An Analysis and Design of a Star Delta Transformer in Series with Active Power Filter for Current Harmonics Reduction*. National Power and Energy Conference, PECon 2004 – Proceedings, p. 94–97. https://doi.org/10.1109/PECON.2004.1461623.

KARVE S. 2016. *Jakość energii. Harmoniczne filtry aktywne*. Europejski Instytut Miedzi – Leonardo Energy, Wrocław. https://leonardo-energy.pl/wp-content/uploads/2016/05/EIM01210-Harmoniczne-filtry-aktywne.pdf.

KHADEM S.K., BASU M., KERRIGAN R., BASU B. 2015. *Power Quality Analysis of Energy Efficient Harmonic Loads*. Institute of Electrical and Electronics Engineers (IEEE) , 470–471. https://doi.org/10.1109/icce-berlin.2014.7034333.

KIM J., LAI J.S., LIU X. 2019. *Analysis of Harmonic Cancellation Performance of a Shunt Phase-Shift Transformer Rectifier*. In 2018 IEEE 4th Southern Power Electronics Conference, SPEC 2018. Institute of Electrical and Electronics Engineers Inc. https://doi.org/10.1109/SPEC.2018.8635850.

KOCMAN S., KOLAR V., VO T.T. 2010. *Elimination of Harmonics Using Multi-Pulse Rectifiers*. In ICHQP 2010 – 14th International Conference on Harmonics and Quality of Power. https://doi.org/10.1109/ICHQP.2010.5625408.

MAZIN H.E., XU W., HUANG B. 2011. *Determining the Harmonic Impacts of Multiple Harmonic-Producing Loads*. IEEE Transactions on Power Delivery, 26(2): 1187–1195. https://doi.org/10.1109/TPWRD.2010.2093544.

MOTTA L., FAÚNDES N. 2016. *Active / Passive Harmonic Filters: Applications, Challenges & Trends*. Proceedings of International Conference on Harmonics and Quality of Power, ICHQP, p. 657–662. IEEE Computer Society. https://doi.org/10.1109/ICHQP.2016.7783319.

MYSIAK P. 2007. *A 24-Pulse Diode Rectifier with Coupled Three-Phase Reactor*. Journal of the Chinese Institute of Engineers, Transactions of the Chinese Institute of Engineers,Series A/Chung-Kuo Kung Ch'eng Hsuch K'an, 30(7): 1197–1212. https://doi.org/10.1080/02533839.2007.9671347.

RAJESHWARI, BAGWARI A. 2018. *Voltage Harmonic Reduction Using Passive Filter Shunt Passive-Active Filters for Non-Linear Load*. Proceedings 7th International Conference on Communication Systems and Network Technologies, CSNT, p. 131–36. Institute of Electrical and Electronics Engineers Inc. https://doi.org/10.1109/CSNT.2017.8418524.

RODRÍGUEZ J., PONTT J., HUERTA R., NEWMAN P. 2004. *24-Pulse Active Front End Rectifier with Low Switching Frequency*. PESC Record – IEEE Annual Power Electronics Specialists Conference, 5: 3517–3523. https://doi.org/10.1109/PESC.2004.1355097.

SAKTHIVEL K.N., DAS S.K., KINI K.R. 2003. *Importance of Quality AC Power Distribution and Understanding of EMC Standards IEC 61000-3-2, IEC 61000-3-3 and IEC 61000-3-11*. Proceedings of the International Conference on Electromagnetic Interference and Compatibility, p. 423–30. Institute of Electrical and Electronics Engineers Inc. https://doi.org/10.1109/ICEMIC.2003.238094.

SALGADO-HERRERA N.M., ANAYA-LARA O., CAMPOS-GAONA D., MEDINA-RIOS A., TAPIA-SANCHEZ R., RODRIGUEZ-RODRIGUEZ J.R. 2018. *Active Front-End Converter Applied for the THD Reduction in Power Systems*. IEEE Power and Energy Society General Meeting. IEEE Computer Society. https://doi.org/10.1109/PESGM.2018.8586414.

AccuSine ® Power Correction System (PCS) Models: CE30 & CE54 Sizes: 50A, 100A, 300A Instruction Bulletin. 2012. Schneider Electric.

SHARMA H., RYLANDER M., DORR D. 2016. *Grid Impacts Due to Increased Penetration of Newer Harmonic Sources*. IEEE Transactions on Industry Applications, 52(1): 99–104. https://doi.org/10.1109/TIA.2015.2464175.

STEIN Z., ZIELIŃSKA M. 2016. *Analiza harmonicznych w prądzie zasilającym wybrane urządzenia średniej mocy*. Electrical Engineering, 86: 213–19.

VIVEK G., NAIR M.D., BARAI M. 2016. *Online Reduction of Fifth and Seventh Harmonics in Single Phase Quasi Square Wave Inverters*. 12th IEEE International Conference Electronics, Energy, Environment, Communication, Computer, Control (E3-C3), INDICON 2015. Institute of Electrical and Electronics Engineers Inc. https://doi.org/10.1109/INDICON.2015.7443721.

YARAHMADI S., MARKADE G.A., SOLTANI J. 2013. *Current Harmonics Reduction of Non-Linear Load by Using Active Power Filter Based on Improved Sliding Mode Control*. PEDSTC 2013 – 4th Annual International Power Electronics, Drive Systems and Technologies Conference, p. 524–528. https://doi.org/10.1109/PEDSTC.2013.6506763.

ŻABICKI D. 2017. *Jakość energii elektrycznej według normy PN-EN 50160*. Elektroinstalator, 6.

Technical Sciences, 2020, 23(1), 25–51

UNIWERSYTET WARMIŃSKO-MAZURSKI W OLSZTYNIE

Quarterly peer-reviewed scientific journal
ISSN 1505-4675
e-ISSN 2083-4527
TECHNICAL SCIENCES
Homepage: www.uwm.edu.pl/techsci/

doi: 10.31648/ts.4863

TIME CONSUMPTION IN CALCULATIONS OF HYDRAULIC AND GEOMETRICAL TORTUOSITY IN GRANULAR BEDS

Wojciech Sobieski[1], Amir Raoof[2], Alraune Zech[3]

[1]ORCID: 0000-0003-1434-5520
Department of Mechanical Engineering and Fundamentals of Machine Design
University of Warmia and Mazury in Olsztyn, Poland
[2]ORCID: 0000-0003-1613-6546
Environmental Hydrogeology, Department of Earth Sciences
Utrecht University, Netherlands
[3]ORCID: 0000-0002-8783-6198
Environmental Hydrogeology, Department of Earth Sciences
Utrecht University, Netherlands

Received 20 December 2019, accepted 6 April 2020, available online 27 April 2020.

Keywords: granular porous media, geometric tortuosity, hydraulic tortuosity, Path Tracking Method, Discrete Element Method, Lattice Boltzmann Method.

Abstract

Tortuosity is one of the most elusive porous media parameters due to its subjective estimation. Here, we compare two approaches for obtaining tortuosity in granular porous media to investigate their capabilities and limitations. First, we determine the hydraulic tortuosity based on the calculated components of the velocity field obtained from flow simulations using the Lattice Boltzmann Method (LBM). Second, we directly determine the geometric tortuosity by making use of the Path Tracking Method (PTM) which only requires the geometric properties of the porous medium. In both cases, we apply the same geometrical structure which is a virtually generated 3D granular bed using the Discrete Element Method consisting of 50 particles. Our results show that the direct PTM is much faster and more precise than the indirect approach based on the calculated velocity field. Therefore, PTM may provide a tool for calculating tortuosity for large 3D granular systems where indirect methods are limited due to the required computational power and time. While LBM considers

Correspondence: Wojciech Sobieski, Katedra Mechaniki i Podstaw Konstrukcji Maszyn, Wydział Nauk Technicznych, Uniwersytet Warmińsko-Mazurski, ul. M. Oczapowskiego 11, 10-957 Olsztyn, phone +48 (89) 523 32 40, e-mail: wojciech.sobieski@uwm.edu.pl.

various routes across the porous media implicitly, PTM identifies them explicitly. As a result, PTM requires a statistical post-processing. As an advantage, this can provide further information than just domain scale average values.

Introduction

Granular porous media is ubiquitous in nature and is applied widely in industry, as fuel cells and chemical reactors. Thus, predicting its physical properties is highly desirable. Of particular interest are systems with a solid phase and one or more fluid phases occupying the pore space.

The growing interest in multiphase systems triggered the development of hybrid numerical methods. Table 1 provides a selected overview of such methods in the context of porous media. Conceptually, hybrid methods couple a numerical code to track the solid phase with a solver for fluid movement within the pore space. Different components are either weakly or strongly coupled; meaning that:

– data is passed only from one method to the other once, no back transfer;

– data is transferred back and forth between both components, usually in an external calculation loop (e.g. within one time step).

The strong coupling usually requires significant adaptions to both numerical codes. Hybrid models often feature Open Source software (*Free Software Foundation* 2020).

The application of hybrid models is computationally demanding. Simulation times of days, weeks or even months are not unusual which limits their applications, particularly in the context of non-deterministic granular media. The problem amplifies when data transfer or geometry conversion is needed.

Hybrid methods are used to investigate the geometrical structure of granular porous media. In such a case, one method serves to generate the geometry of the porous body; usually a random algorithm or a Discrete Element Method (DEM) is applied. The second method is used to characterize features and parameters of the pore space; often Finite Volume Method (FVM) or Lattice Boltzmann Method (LBM) are in use.

Of particular interest for us is the tortuosity, which characterizes the prolongation of flow paths due to the granular porous structure. It is often associated to how intertwined paths through the granular media are. This geometrical parameter is a significant characteristic of granular medium, but at the same time difficult to obtain.

Tortuosity (τ[-]) is defined as the ratio of an average path length (L_p [m]) in the void space of a porous medium to the thickness of the porous body (L_0 [m]) (Bear 1972):

$$\tau = \frac{L_p}{L_0} \tag{1}$$

Table 1

Hybrid models used for granular porous media and to simulate fluid flow

Source	Methods (software)	Application
FENG et al. (2007)	DEM & LBM	particle transport in turbulent fluid flows
ROJEK (2007)	DEM & FEM (Simpact)	rock cutting
CHEN (2009)	DEM (YADE, PFC2D) & FVM (OpenFoam)	fluid flow through an assembly of particles
SOBIESKI (2009)	DEM (PFC3D, YADE) & PTM	geometrical structure of granular beds
VILLARD et al. (2009)	FEM & DEM	earth structures reinforced by geosynthetic
ERATH (2010)	FEM & BEM	numerical analysis of coupling
DUDA et al. (2011)	LBM	fluid flow through a porous medium (with self-generated geometry)
WU et al. (2011)	FEM & FVM-VOF	moving obstacle in fluid
CATALANO (2012)	DEM (YADE) & PFV (own model)	biphasic granular media
KOMORÓCZI et al. (2012)	DEM & SPH	boudinage, hydro-fracturing
STRÁNSKÝ, JIRÁSEK (2012)	FEM (OOFEM) & DEM (YADE)	cantilever shock analysis
XIANG et al. (2012)	FEM & DEM; (FEMDEM)	breakwater modelling
GALINDO-TORRES (2013)	DEM & LBM	fluid-solid interaction with particles of general shapes
SRIVASTAVA et al. (2013)	FEM & DEM	fluid-particle interactions
SUN et al. (2013)	DEM (OVAL) &-LBM	permeability evolutions inside a dilatants shear band
ZHAO, SHAN (2013)	FVM (OpenFOAM) & DEM (LAMMPS, LIGGGHTS)	fluid-particle interaction
MAREK (2014)	DEM & IBM	fluid flow through an assembly of Raschig rings (with self-generated geometry)
NORDBOTTEN (2014)	FEM (Visage) & FVM (Eclipse)	Hydro-mechanical simulation in porous media
AFKHAMI et al. (2015)	LES (Fluent) & DEM (EDEM)	particle interaction and agglomeration in a turbulent channel flow
MARKL (2015)	LBM (waLBerla) & DEM (pe)	beam melting
QIU (2015)	DEM & LBM	fluid flow through porous media
ZENG, YAO (2015)	DFM & FEM	fractured porous media
MAHABADI et al. (2016)	FEM-DEM; (Irazu)	rocks mechanics
MARKAUSKAS et al. (2016)	DEM & SPH and DEM & FVM (Fluent)	particle-fluid Poiseuille flow in a channel

cont. Table 1

SAKAI (2016)	SPH & MPS	fluidisation, circulating flow, screw conveyor, twin-screw kneader
TRYKOZKO et al. (2016)	FVM	fluid flow through a porous medium (with self-generated geometry)
AL-ARKAWAZI et al. (2017)	DEM (SIGRAME) & FVM (Code_Saturne)	fluidisation

DEM – Discrete Element Method, FVM – Finite Volume Method, IBM – Immersed Boundary Method, PFV – Pore-scale Finite Volume, LES – Large Eddy Simulation, FEM – Finite Element Method, LBM – Lattice Boltzmann Method, BEM – Boundary Element Method, SPH – Smoothed Particle Hydrodynamics, DFM – Discrete Fractured Model, PTM – Path Tracking Method.

The definition holds for tortuosity calculations in 2D or 3D space. Note that L_p is at minimum the length of L_0. Thus, physically reasonable values of τ are always higher or equal one. The above definition requires the existence of free passages through the porous body. We limit our investigation to granular media where pore space forms a connected network through which fluid flow is possible independent of the domain size and the particle distribution.

In general, the tortuosity of a specific granular medium is either calculated based on the pore channels geometry (geometrical tortuosity, τ^g) or based on the ratios of velocity components in a creeping fluid flow (hydraulic tortuosity, τ^h). Other kinds of tortuosity are also known, e.g. diffusional (GHAREDAGHLOO et al. 2018) or electric tortuosity (SAOMOTO, KATAGIRI 2015). In some works, the Minkowski space is applied to analyse the tortuosity of porous media (CIESZKO, KRIESE 2006, CIESZKO 2009). The geometrical tortuosity can be determined by direct calculations, following the definition in Equation 1. One of these methods is the Path Tracking Method (SOBIESKI 2009, SOBIESKI et al. 2012). Hydraulic tortuosity requires the application of hybrid methods (Tab. 1), combining geometry generation and flow simulations. Besides standard techniques as Finite Difference, Finite Element or Finite Volume Methods, the Lattice Boltzmann Method is particularly attractive in the context of porous media due to its simple geometry specification. Geometries as well as velocity fields may as well be determined by experimental techniques, such as Particle Image Velocimetry (PIV) (WILLERT, GHARIB 1991).

KOPONEN et al. (1996, 1997) proposed to calculate the hydraulic tortuosity as

$$\tau^h = \frac{\sum v}{\sum v_x} \tag{2}$$

where:

v_x – the velocity component in the direction of macroscopic flow in the porous material [m/s],

v – the absolute velocity magnitude [m/s].

The sums go over the entire pore space. The specification of τ^h (Eq. 2) follows the conceptualization of tortuosity in a capillary tube model by CARMAN (1937). However, τ^h as in Equation 2 has no direction connection with the actual flow path and is determined solely through fluctuations of the local flow field around the average flux in main flow direction.

KOPONEN et al. (1996) investigated the lattice gas flow through 2D random porous media where the macroscopic parameters of the fluid are simple functions of the lattice gas distribution function. The work of KOPONEN et al. (1997) and following work based on the same methodology (DUDA et al., 2011, NABOVATI, SOUSA 2007) are limited to flow in 2D random porous media with rectangular solid particles. There are less studies applying the methodology in 3D due to the tremendous computational effort to calculate the velocity field in 3D (WANG 2014).

In this study, we compare two conceptually different methodologies for obtaining tortuosity in 3D granular beds. We determine hydraulic tortuosity following the idea of KOPONEN et al. (1996, 1997) and we calculate the geometric tortuosity making use of the Path Tracking Method. To compare the two methods, we apply them using the same virtually created granular structure.

Materials and Methods

Granular Material

Starting point for the method comparison is a virtual realization of a granular structure. We create one bed consisting of 50 spherical particles placed in a cuboid domain. Particle sizes are based on marble glass beads used in previous experimental investigations (SOBIESKI et al. 2016b) SiLibeads Glass Type S (LINDNER 2015). These grains have an average diameter equal to 6.072 mm and a standard deviation of 0.051.

Discrete Element Method

We created the virtual granular bed using the Discrete Element Method (DEM) proposed by CUNDALL and STRACK (1979). DEM evaluates the dynamics of a set of solid bodies using Newtonian laws of linear and angular motion:

$$m_i \frac{\mathrm{d}\vec{v}_i}{\mathrm{d}t} = \sum_{j=1}^{n_c} \left(\vec{F}_{ij}^{\,n} + \vec{F}_{ij}^{\,t}\right) + \vec{F}_i^{\,\mathrm{ext}} \tag{3}$$

and

$$I_i \frac{\mathrm{d}\vec{\omega}_i}{\mathrm{d}t} = \sum_{j=1}^{n_c} \left(r_i \times \vec{F}_{ij}^{\,t} + f_{ij} \times \vec{F}_{ij}^{\,n}\right) \tag{4}$$

where:

m_i – mass of the i-th body [kg],
I_i – moment of inertia of the i-th body [kg·m^2],
$\vec{v}_i$ – linear velocity of the i-th body [m/s],
$\vec{\omega}_i$ – angular velocity of the i-th body [rad/s],
$\vec{F}_{ij}^{n}$ – normal forces between neighbouring bodies i and j [N],
$\vec{F}_{ij}^{t}$ – tangential forces between neighbouring bodies i and j [N],
n_c – number of contacts between i-th body and neighbouring bodies [-],
$\vec{F}_i^{\text{ext}}$ – external forces acting on the i-th body (e.g. gravity force) [N],
r_i – distance between the contact point with the j-th body and the mass centre of the i-th body [m],
f_{ij} – distance between the direction of acting the normal force and the mass centre [m].

The algorithm consists of three main steps:

– detecting all contact pairs;

– calculating new values of forces acting on each body (velocities and displacements are constant in this stage);

– calculating new values of velocities and displacements (forces are constant in this stage).

The key aspect is the mathematical description of the normal and tangential forces between bodies in all contact points. Thus, their calculation in every time step is particularly important.

The physically based DEM approach is advantageous to simple random generators for constructing 3D porous structures since it takes particle interactions into account. That allows to create virtual beds with smaller porosity.

We created the specific virtual granular bed using the Radius Expansion Method (WIDULIŃSKI et al. 2009), implemented in the open source code YADE (ŠMILAUER et al. 2017). The final geometry is fully characterized by the centre coordinates of particles (x_m, y_m, z_m) (m = 1, …, 50) and their radii r_m (or diameter d_m). From that, geometrical characteristics such as porosity can calculated.

Lattice Boltzmann Method

The Lattice Boltzmann Method (LBM) is used to calculate the flow on the porous grain structure. The flow of a fluid is characterized by the discrete Boltzmann equation (BHATNAGAR et al. 1954):

$$\frac{\partial f}{\partial t} + \vec{v}\nabla_{\vec{x}} f + \frac{\vec{F}}{m}\nabla_{\vec{v}} f = \left(\frac{\partial f}{\partial t}\right)_{\text{col}} \tag{5}$$

where:

$f(x, v, t)$ – single-particle distribution function (where x is the coordinate and v is the microscopic velocity),

$\frac{\vec{F}}{m}$ – is the unitary external forces,

$\left(\frac{\partial f}{\partial t}\right)_{\text{col}}$ – represents the collisional term.

Fluid flow is determined by numerically solving Equation 5 on a binary grid. The grid is usually defined as a three-dimensional matrix of logical numbers, e.g., a value of 1 characterizes a grid point of the solid body and 0 values mean that the point is a part of the pore space.

The algorithm to solve Equation 5 covers two main steps (BHATNAGAR et al. 1954):

a) streaming processes; and

b) collision process, which is the mathematically critical step.

Characteristic for the LBM is that streaming occurs only in discrete directions. Two numbers, define the variant of the LBM model: the dimensionality (e.g. D3) and the number of directions (e.g. Q27). Thus, D3Q27 describes a model in three-dimensions where the lattice gas can move in 27 directions. The most popular LBM variants are D2Q9, D3Q15, D3Q19 and D3Q27.

Knowing the distribution function (f) in each i^{th} direction allows to calculate the macroscopic density and the macroscopic velocity of the lattice gas using:

$$\rho = \sum_{i=0}^{n_i} f_i e_i \tag{6}$$

and

$$v = \frac{1}{\rho} \sum_{i=0}^{n_i} f_i e_i \tag{7}$$

where:

r – lattice gas density,

v – lattice gas velocity,

e_i – direction vectors,

n_i – the number of the space directions in the model.

The calculated flow velocities by the LBM are used to compute the hydraulic tortuosity according to the Equation 2.

We calculated creeping flow in the Lattice Boltzmann Method making use of the Palabos numerical code (Palabos Home 2017). We applied a D3Q27 model with periodic boundary condition in the main direction flow. In the other directions (X and Y), we applied the bounce-back boundary condition to mimic

the no flow boundaries. The unitary external force (Eq. 5) responsible for the movement of the lattice gas were set to 0.0, 0.0 and 0.0001 lattice units [lu] in X, Y and Z direction at all nodes in the pore space. The relaxation time was constant and simulation results were recorded after 1000, 2000, 4000, 8000, 16 000 and 32 000 iterations.

Geometry Conversion

Using DEM generated geometries for LBM calculation requires a conversion step since both methods rely on different geometry conceptualizations. The vector geometry description of the grain objects in the DEM needs to be transformed into an LBM structured binary grid as summarized in Figure 1.

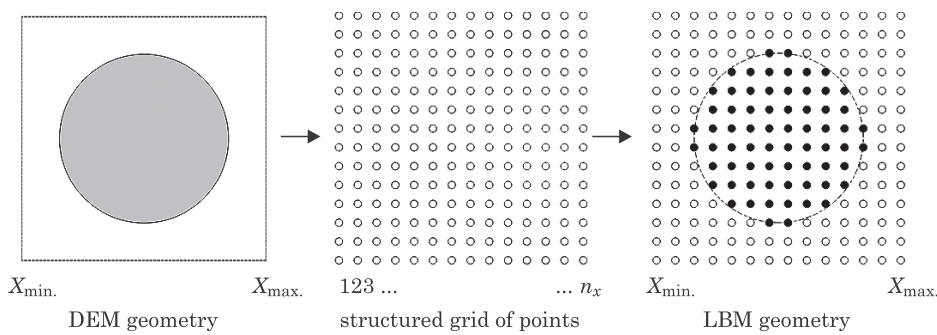

Fig. 1. Schema of geometry conversion between DEM and LBM

We implemented a Fortran code to convert the DEM geometry to an LBM binary structure matrix of 0's and 1's.

Two types of structural grids may be distinguished: node-centred and cell-centred grids. Both kinds of grids may be conveniently visualised by ParaView (ParaView Home 2020), MayaVi (MayaVi Home 2020) or other similar software. We follow the second approach given that grain centres can directly be interpreted as points in the LBM grid. As a consequence, the number of cells equals the number of points simplifying the implementation of the LBM.

Given the geometric parameters, the LBM grid value is specified as 1 (solid) if a sphere is overlapping the grid coordinate, and otherwise 0 (void space), as visualized in Figure 2. The total number of solid points representing a grain is a function of the LBM grid resolution. It is characterized by the number of points per direction (n_x, n_y and n_z). A sufficient resolution of grains is relevant for computational accuracy as outlined by (WANG 2014), and further discussed in section *Geometry conversion for a LBM model*.

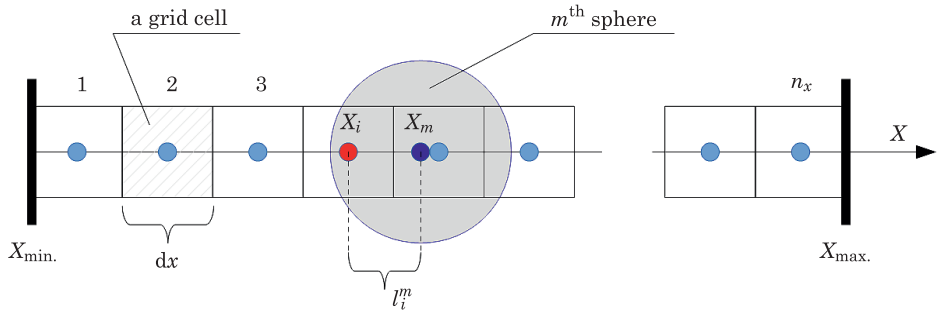

Fig. 2. Converting the geometry from DEM coordinates to a LBM grid for a selected space direction

Path Tracking Method

We calculate geometrical tortuosity using the Path Tracking Method (PTM), developed by Sobieski (SOBIESKI 2009, SOBIESKI et al. 2016a). The numerical method calculates the lengths of paths in granular beds based on the geometrical parameters of the grains. The length of a path across the domain is the sum of the unitary lengths calculated inside local tetrahedral structures (Fig. 3). We performed calculation with the PathFinder code (a freely available implementation of the PTM method). Details on the PTM can be found in the PathFinder Users' Guide (SOBIESKI, LIPIŃSKI 2016).

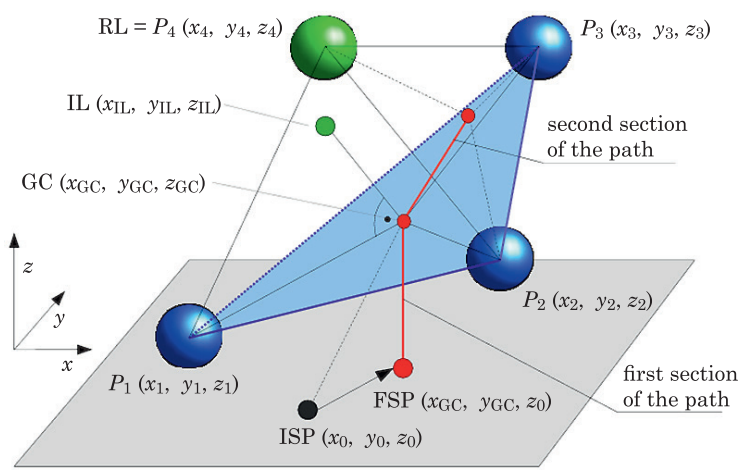

Fig. 3. Schema of the tetrahedral structure used in the Path Tracking Method; meaning of abbreviations: ISP – Initial Starting Point (starting point of calculation), FSP – Final Starting Point (starting point of the path), GC – gravity center of the triangle formed by particles P_1, P_2 and P_3, IL – Ideal Location (predicted centre of particle P_4 forming the tetrahedral structure), RL – Real Location (actual centre of particle P_4)

Knowing the path length within the granular domain allows to calculate the geometric tortuosity of that path based on Equation 1. The procedure is repeated for multiple starting points to calculate the average tortuosity value as the domain tortuosity. The algorithm allows to calculate the tortuosity independent of the resolution (SOBIESKI 2016).

We applied the method to 25×25 Initial Starting Points on a regular grid. Doing so, we arrived at a domain tortuosity as average over 625 paths. Some of these paths coincide when initial starting points end up in the same trajectory. SOBIESKI et al. (2012) found that this effect is not insignificant. Furthermore, he pointed out that 25 individual paths of fully distinct trajectories are sufficient to obtain a representative value of the tortuosity. Representative value here means that the average does not change with increasing number, in line with the concept of represenative elementary volumes (REV) (BEAR 1972).

We calculate the porosity of the specific virtual bed using the PathFinder code. The analytically determined value of 0.5832 equals the value reported by the YADE code with a relative error of 0.03%.

Results and Discussion

Virtual bed

The 3D realization of a porous medium structure with 50 grains is visualized in Figure 3. The virtual bed was created using YADE open source numerical code (ŠMILAUER et al. 2017), which uses the Discrete Element and the Radius Expansion Method as described in section *Discrete Element Method*. Details on the procedure can be found in (SOBIESKI et al. 2016a, 2016b).

Grains have a size distribution with an average diameter of $d = 5.9$ mm and standard deviation of $\sigma = 0.051$ mm (Fig. 4). The porosity of the bed is $\phi = 0.583$, based on geometrical calculations. The size of the domain and number of particles

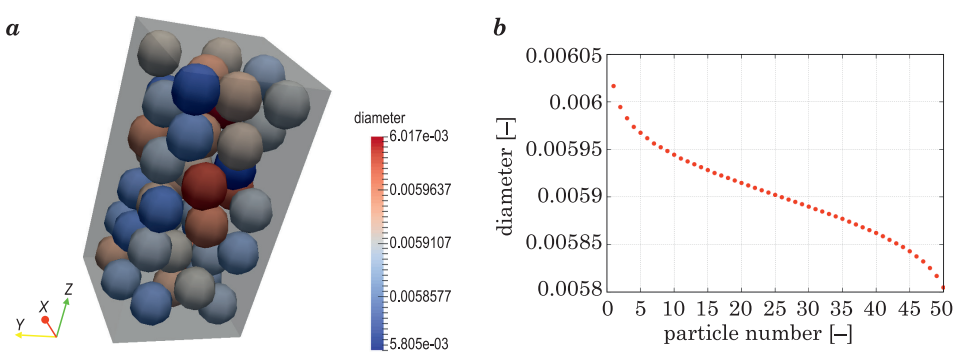

Fig. 4. 3D view (*a*) and particle size distribution (*b*) of the generated virtual bed

was chosen in balance between numerical accuracy and the computational limitations. The slight deviation of the average diameter from the starting value is a results of the growing process within the Radius Expansion Method. This aspect, however, does not impact the results of this study.

Geometry conversion for a LBM model

We prepared 8 LBM grid resolution of the virtual bed of $n_x \times n_y \times n_y$ (with n being the total number of grid points): $32 \times 32 \times 64$ ($n = 65\,536$), $64 \times 64 \times 128$ ($n = 524\,288$), $96 \times 96 \times 192$ ($n = 1\,769\,472$), $128 \times 128 \times 256$ ($n = 4\,194\,304$), $160 \times 160 \times 320$ ($n = 8\,192\,000$), $192 \times 192 \times 384$ ($n = 14\,155\,776$), $224 \times 224 \times 448$ ($n = 22\,478\,848$) and $256 \times 256 \times 512$ ($n = 33\,554\,432$). Figure 5*a* shows the virtual bed and its equivalent in a form of the lattice grid in coarse resolution. Figure 5*b* a cross section shows how the particle surface is approximated by grid cells.

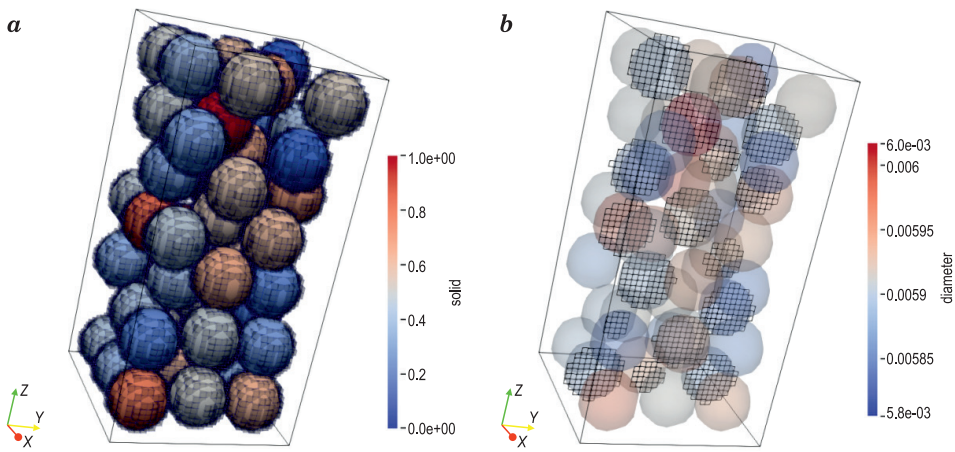

Fig. 5. Example of the LBM grid generated for the virtual bed with a resolution of $32 \times 32 \times 64$: *a* – full view, *b* – cross-section in *YZ* plane

The higher the resolution of a single particle in the LBM grid, the higher are the computational cost for the grid conversion. Figure 6 provides an example for a sphere in LBM grid resolutions of $32 \times 32 \times 32$; $96 \times 96 \times 96$ and $160 \times 160 \times 160$ points.

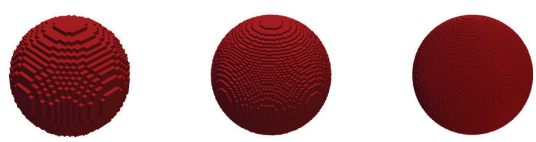

Fig. 6. A simple sphere converted to LBM grid with different resolutions

According to WANG (2014), the radius of each sphere should be at least resolved by ten lattice nodes. All except the smallest of our LBM grids fulfil this condition with lattice nodes per radius of 5 (Fig. 5*b*), 10, 15, 20, 25, 30, 35 and 40, respectively.

Figure 7 summarizes the conversion time (t_c) as function of the grid point number. Time increases linearly $t_c = ax + b$ with a slope of $a = 0.000154$ and $b = 0$. At high resolutions conversion times are up to hours. This aspect becomes critical when applying the method in hybrid methods with feedback loops for cases with changes in the solid phase.

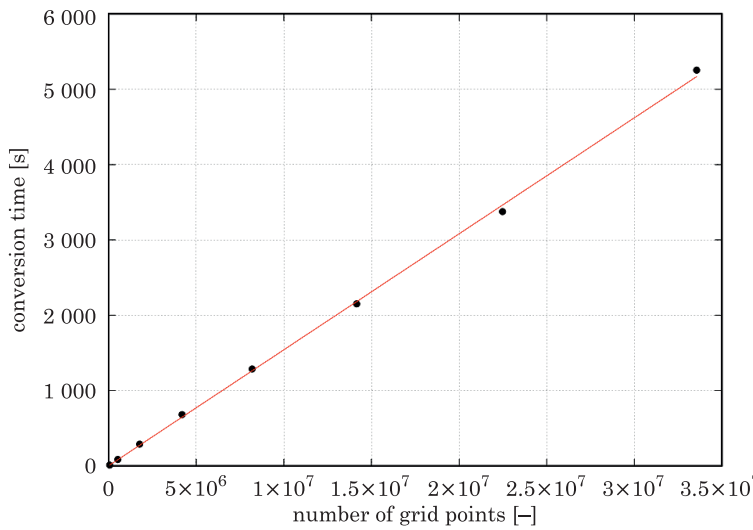

Fig. 7. Conversion time in function on grid resolution

We check the influence of the grid resolution on the LBM geometry by calculating a LBM porosity as

$$\phi_{\mathrm{LBM}} = \frac{n_0}{n_x n_y n_z} \tag{8}$$

where:

n_0 – the number of grid points belonging to the porous space of the granular bed (denoted by 0 in the geometry matrix) [-],

$n_x n_y n_z$ – the total number of points in the grid [-].

Figure 8 shows the LBM porosity as function of resolution. The LBM porosity decreases approaching an asymptotic value. The trend can be fitted to the functional relationship:

$$\phi_{\mathrm{LBM}} = \frac{ax + b}{cx + d} \tag{9}$$

with coefficients a, b, c and d equal to 1.17325, 0.141114, 2.01073 and 0.131859, respectively.

The LBM porosity is greater than the geometrical porosity of the DEM model, clearly overestimating the porosity of the porous body. However, the relative errors decrease with increasing grid resolution and do not exceed a few percent as shown in the subplot of Figure 8. The relative errors between the LBM porosity and the reference porosity are a good indicator for the minimum required grid resolution, with an acceptable level of about 1% (Fig. 8).

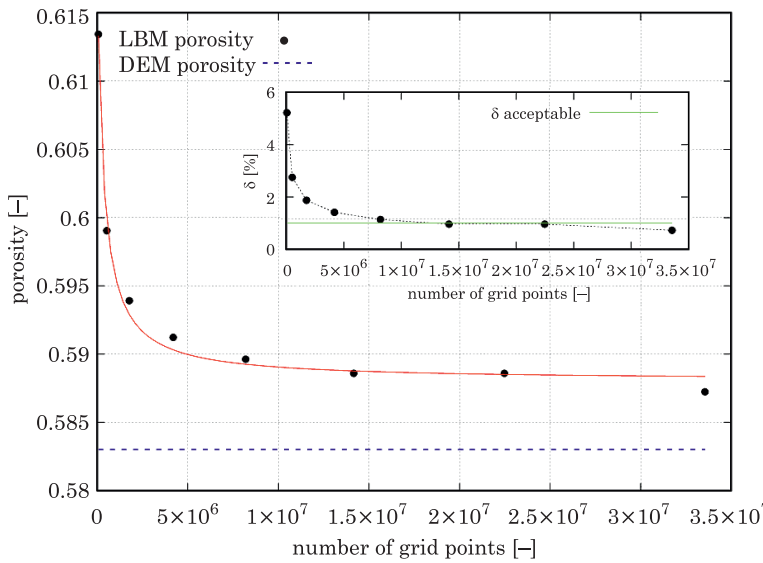

Fig. 8. LBM porosity as function of the grid resolution for cases 1–8.

LBM simulation

We calculated the velocity distribution in the LBM grids using the Palabos numerical code (Palabos Home 2017) with computational specifications outlined in section *Lattice Boltzmann Method*. Figure 9 shows the virtual bed, the converted LBM grid (with reduced resolution of points), the distribution of the lattice gas density (being close to one in the pore space and zero inside the spheres) and the distribution of the velocity field.

Figures 10 and 11 displays the dependency of the average and maximum lattice gas density to the number of grid nodes and the number of iterations. Both show

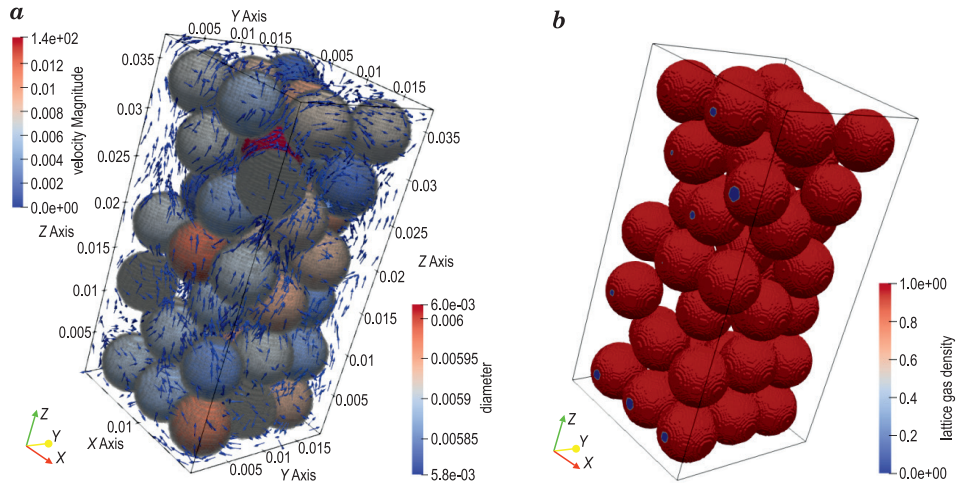

Fig. 9. Results of LBM flow field calculations for the grid of 128×128×256 (after 16 000 iterations): *a* – velocity field, *b* – binary form of the bed geometry

non-linear relationships. We focus on the lattice gas density as central quantity from which all other parameters, such as velocity or pressure can be inferred.

Figure 10 shows that a minimum number of iterations is needed to obtain a steady state for small grid resolutions. For the grids containing 65 536 and 524 288 (65 536×8) nodes approximately 2000 and 16 000 (2000×8) are need. Thus, the minimum number of iterations depends linearly on the grid resolution. Obtaining steady state for large grids is, in practice, strongly limited by the massive calculation times. Following the trend, the required simulation time (on the same computer) is about 135 days for the largest grid. This value was estimated on the basis of data obtained for the grid 32×32×64 (65 536 nodes) and 16 000 iterations, where the calculation time was equal to 34 026 s. In turn, the number of nodes for the grid resolution 224×224×448 (22 478 848 nodes) is 343 times greater. Assuming a linear trend, the calculation time needed for performing the same number of iterations should be 343 times longer, thus about 135 days.

In Figure 11 shows a comparison for the maximum values of the lattice gas. Again, values increase with the grid resolution. The maximum values of the lattice gas velocity may be even 15 times greater than the average ones.

Figure 12 displays the average velocity as function of grid resolution and the number of iterations. The deviation of results for less than 4000 iterations suggests that the required minimum number of iterations is about 8000, independent of the grid resolution. Increasing the iterations beyond 8000 does not change the velocity for the same grid resolution. However, velocities differ between grid resolution, with higher values for denser grids.

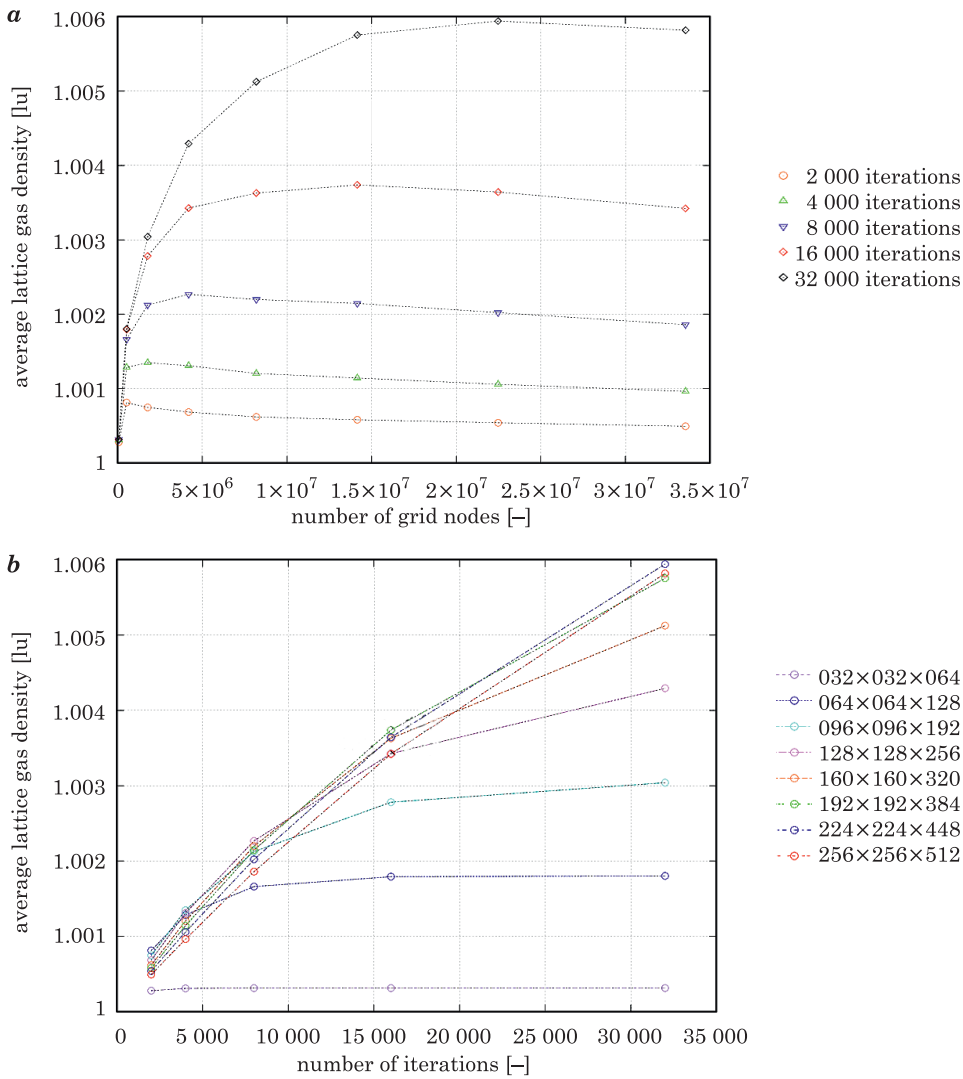

Fig. 10. Average density of the lattice gas as a function of the grid resolution (*a*) and the number of iterations (*b*)

Table 2 summarizes average velocities and relative errors compared to the highest resolution (256×256×512) with 32 000 iterations. The small average velocity for the lowest grid resolution clearly shows that it is too coarse, which is in line with the conclusion of WANG (2014) regarding the resolution of solid particle in the LBM grid.

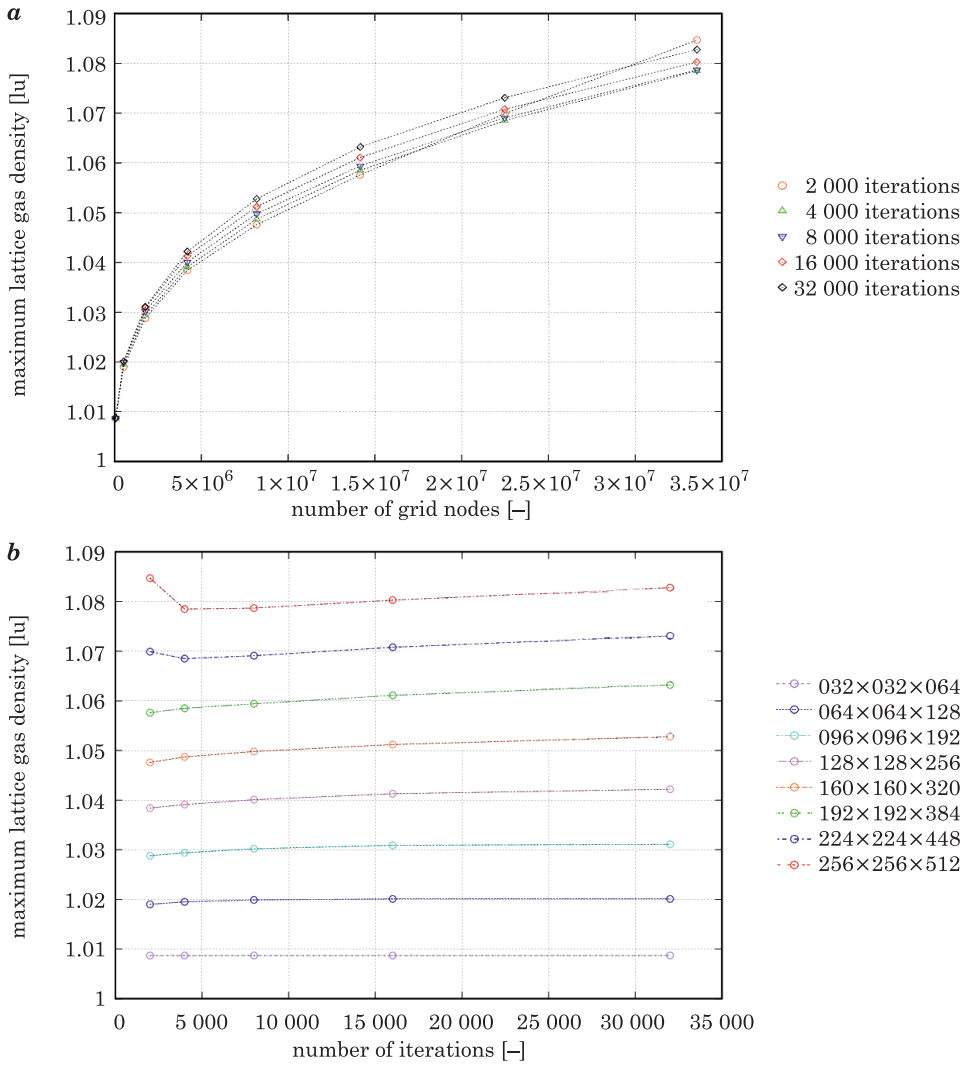

Fig. 11. Maximum value of the lattice gas density as a function of the grid resolution (*a*) and the number of iterations (*b*)

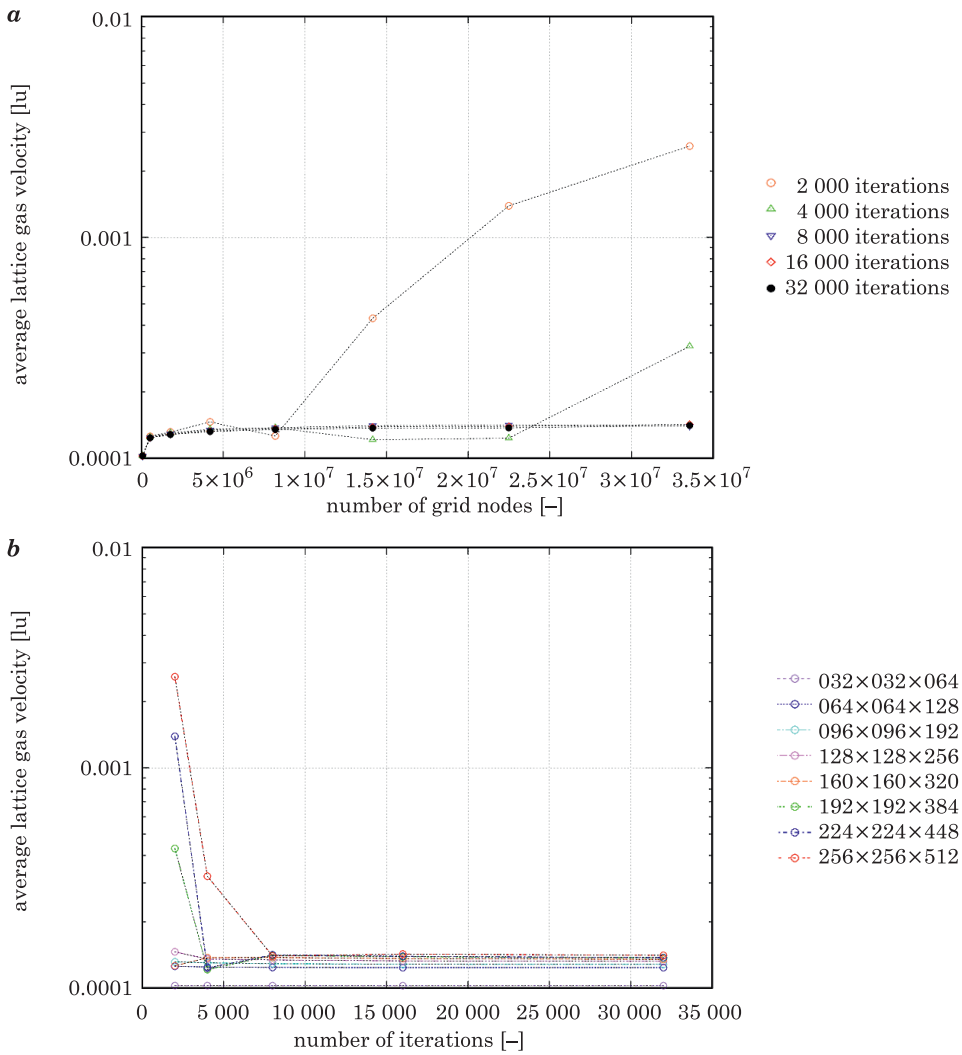

Fig. 12. Average velocity of the lattice gas density as a function of the grid resolution (*a*) and the number of iterations (*b*)

Table 2

Average lattice gas velocities v_{ave} and relative errors δ (relative to highest resolution) for 32 000 iterations

Case No.	n [-]	v_{ave} [lu]	δ [%]
1	65 537	1.0243E-04	27.16
2	524 289	1.2372E-04	12.02
3	1 769 473	1.2795E-04	9.02
4	4 194 305	1.3200E-04	6.14
5	8 192 001	1.3487E-04	4.09
6	14 155 777	1.3694E-04	2.62
7	22 478 849	1.3723E-04	2.41
8	33 554 432	1.4063E-04	0.00

Figure 13 shows the hydraulic tortuosity calculated from the LBM results using Equation 2. All cases give physically acceptable values, i.e., $\tau > 1$. We see that values stabilize for 8000 iterations and more, independent of the grid resolution. This supports the previous finding that 8000 is the required minimum number of iterations.

The hydraulic tortuosity at sufficient iterations differs among grid resolutions, although only slightly for higher resolutions. The asymptotic value ranges around 1.556. Assuming that the result obtained for the highest grid resolution and 32 000 iterations provides the most exact value, we can determine the relative errors for other cases (at 32 000 iterations) as: 0.74%, 0.84%, 1.08%, 2.14%, 4.09%, 7.87% and 14.16% for cases 7 to 1, respectively.

In addition to our hydraulic tortuosity results, we have shown the result obtained by WANG (2014) in Figure 13. We consider the domain size to be one reasons for deviation between our results and that of Wang as he used a larger porous structure, thus the boundaries affect the results less. In our model all spheres are located inside the domain, giving that the porosity is higher near the walls. Thus, preferential pathways with higher velocities are formed (Fig. 14), leading to an overestimation of tortuosity.

To explore the effect of the boundaries, we recalculated the tortuosity considering only velocities within the domain (Fig. 14*b*) within a distance of 10% of the domain size from the outer boundary. Figure 15 shows the hydraulic tortuosity as function of the LBM settings for the reduced amount of velocity values. Generally, the tortuosity decreases. For the highest resolution by about 4% from 1.556 to 1.49. Analogously, in the range of 4% for the other cases. However, the calculated value of hydraulic tortuosity stays high, indicating that the method of determining tortuosity independent of the pathways by relating fluid velocities might be error prone for high porosities.

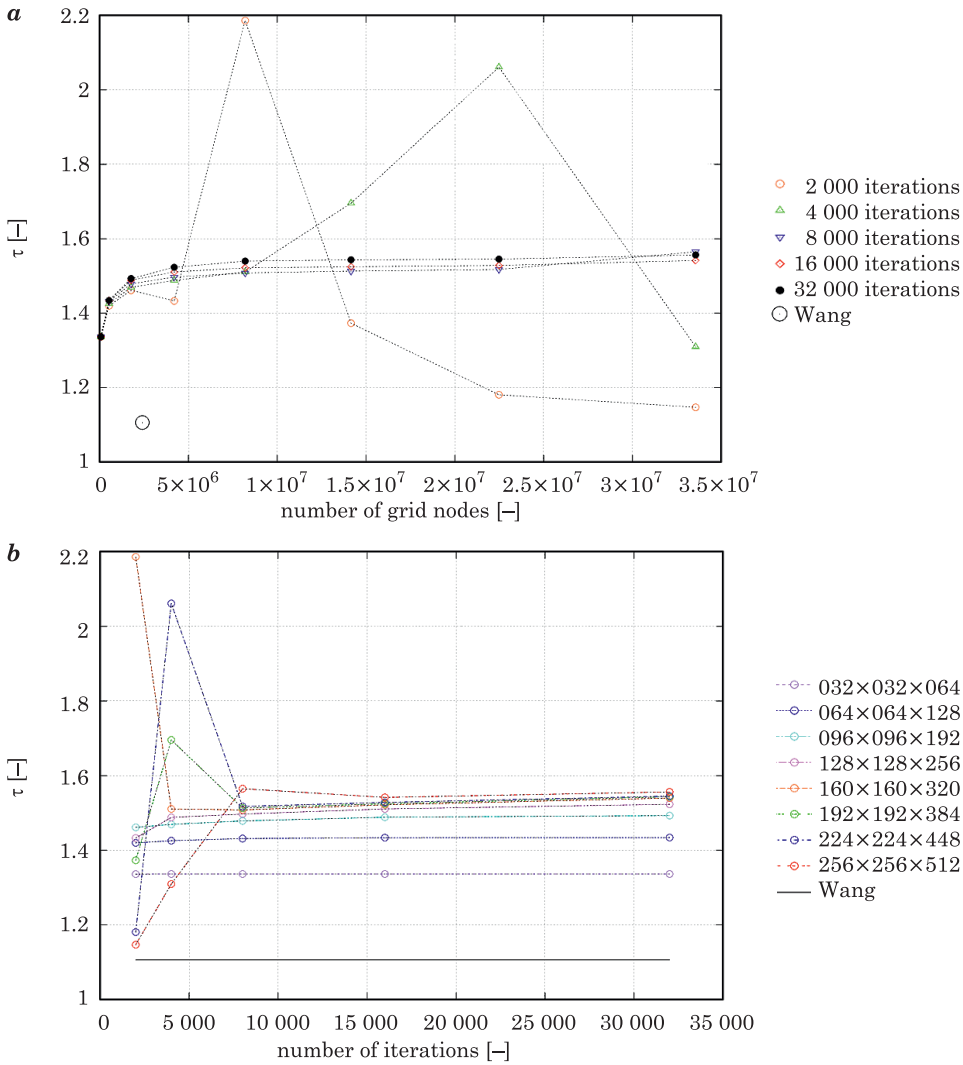

Fig. 13. Hydraulic tortuosity as function of the grid resolution (*a*) and the number of iterations (*b*)

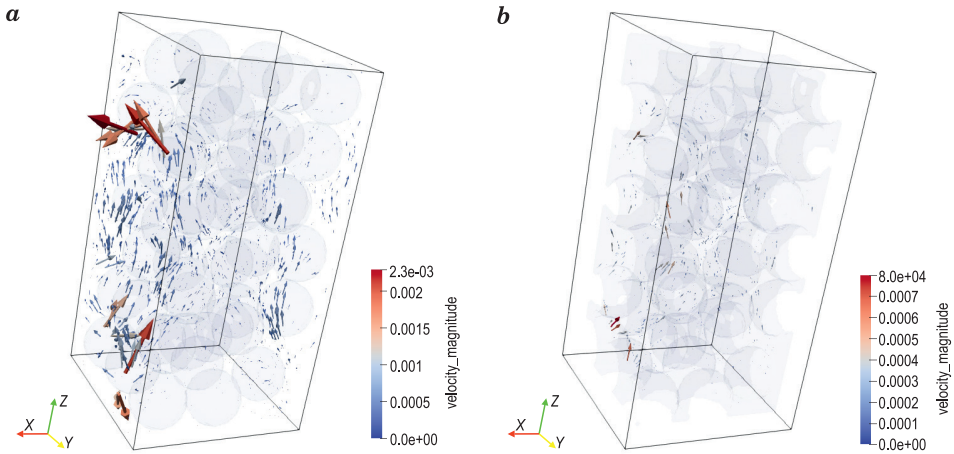

Fig. 14. Visualisations of the velocity field for the grid 64×64×128 and 32 000 iterations taking all value into account (*a*) and cutting off boundary effects (*b*)

Our results show that grid resolution in LBM has an impact on the calculated hydraulic tortuosity. Thus, we cannot agree with KOPONEN et al. (1996) who found that for a given obstacle configuration the tortuosities calculated with different lattice resolutions were close to each other. The same conclusion was given by NABOVATI and SOUSA (2007), stating that the effect of the domain resolution is negligible in the range examined. These conclusions were developed on the basis of 2D simulations and may not be applicable for 3D geometries. This is also supported by the results of Wang who stated that the radius of the sphere should not be less than ten lattices. We see that tortuosity differences become very small when the grid resolution and the number of iterations increase. However, both model parameters are subject to the specific case setting and needs to be determined individually, which takes additional time.

PTM calculations

In the second stage, we used the Path Tracking Method to determine the geometrical tortuosity of the granular bed (section *Path Tracking Method*). Figure 16 shows one calculated path. Figure 17 visualizes the tortuosity field for the 625 individual starting points. The average value (τ_{ave}) is 1.185 which is 7.14% higher than the tortuosity of Wang (1.106). Figure 18 summarizes the individual tortuosity values of all paths. Additionally, it contains values for two characteristic cases:

– the grid resolution 32×32×64 (Fig. 10*b*),
– the highest grid resolution 256×256×512.

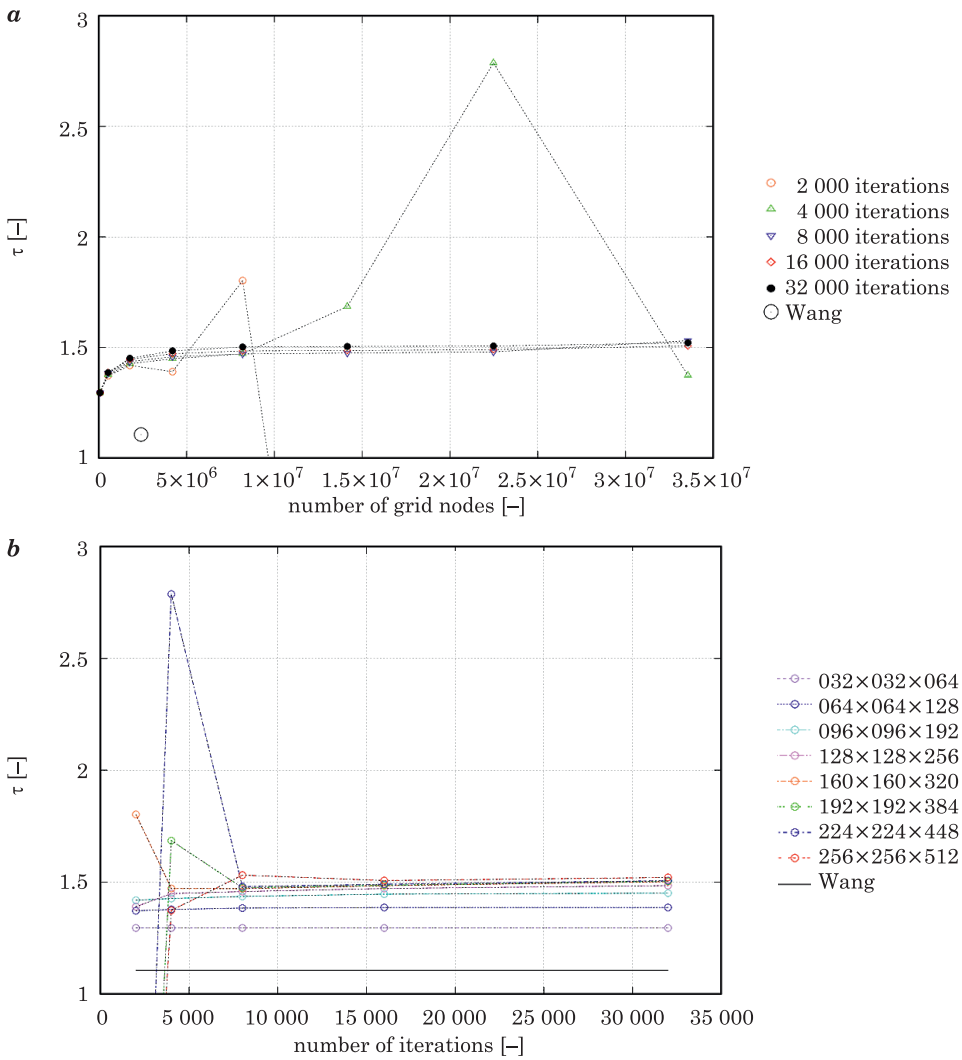

Fig. 15. Hydraulic tortuosity as function of the grid resolution (*a*) and the number of iterations (*b*) for simulated velocities in the inner domain

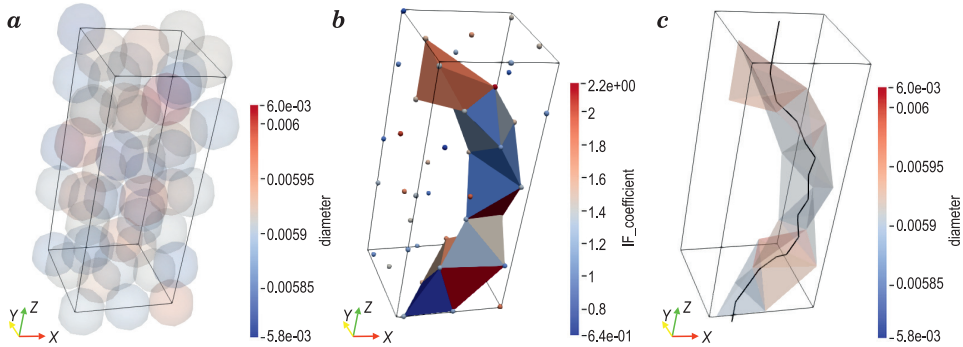

Fig. 16. Visualisation of the granular bed (*a*), tetrahedral structures used in the Path Tracking method (dots represent the spheres centres) (*b*) and the final path (*c*)

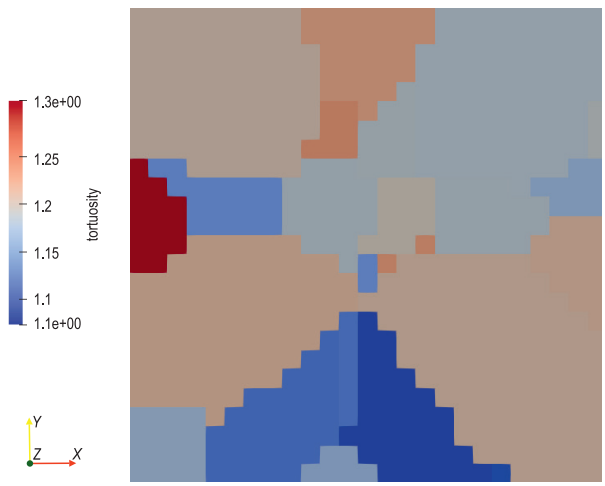

Fig. 17. Tortuosity as function of the starting point coordinates for the 625 individual locations

In both cases the number of iterations is equal to 32 000. The tortuosities obtained with LBM are clearly higher than for the others cases. Thus, it remains open which value represent tortuosity best in the LBM approach. Potential factors for improvement might be a bigger domain size, higher lattice resolution and/or more iterations.

Figures 17 and 18 show large areas of equal tortuosity values. These starting points end up in identical trajectories. They are represented by the same Final Starting Point (see Fig. 3). The sizes and shapes of these areas depends on the local arrangement of particles. For details on tortuosity fields, the reader is referred to SOBIESKI (2016).

The calculation time of the 625 individual path lengths was very short, in the order of a few minutes. Figure 19 shows the individual calculation times

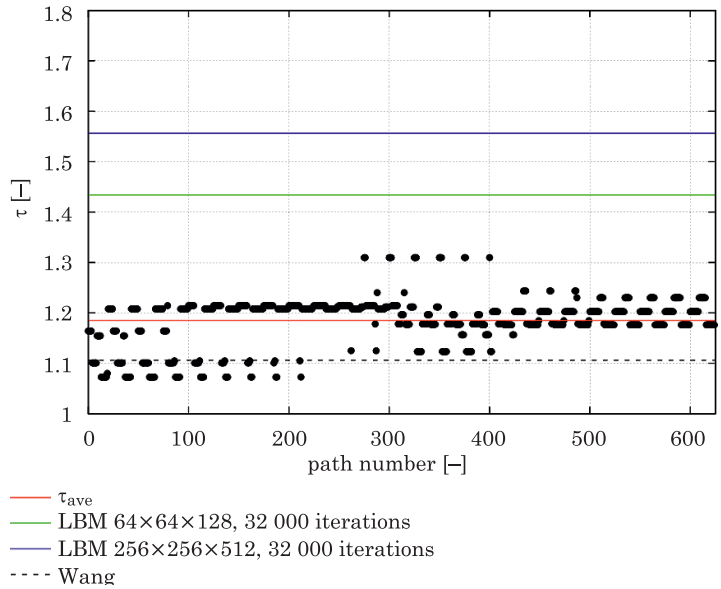

Fig. 18. Individual tortuosity values for the 625 initial starting points

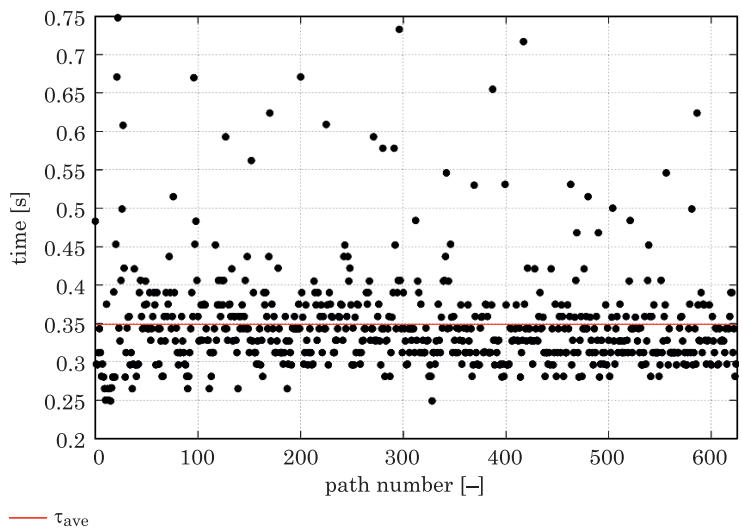

Fig. 19. Calculation times of the individual path length with the PTM

summing up to about 218 s. It can be seen that calculation times differ depending on the Initial Starting Point, which differences up to a factor of 3. Compared to the LBM simulations, this is 10 times faster for the smallest grid resolution and 2000 iterations. For the high grid resolution of 256×256×512 and 32 000 iterations, the ratio equals about 83 700. This illustrates a major advantage of the PTM approach.

Another benefit of the PTM is the spatial resolution of the individual tortuosity values. Obtaining a distribution of tortuosities for granular beds allows to perform detailed analysis of flow field specifications and statistical analysis.

Summary and Conclusions

We performed a comparison of two numerical methods to calculate tortuosity of granular beds using generated 3D media. We applied the Lattice Boltzmann Method (LBM) to compute hydraulic tortuosity based on the ratios of flow velocities and also used Path Tracking Method (PTM) which directly calculates geometric tortuosity. For both methods, we investigated computation times as well as the quality of tortuosity values given data resolution.

Table 3 summarizes the main features of both methodologies. In particular, this study has shown that:

– The resolution of the LBM grid plays a critical role. It affects the conversion time (linearly), the actual porosity, the calculation time (linearly), and the calculated velocity values. The density and the velocity of the lattice gas depend non-linearly on LBM grid.

– The number of iterations performed during the LBM simulations is important. Both, average and maximum lattice gas density change non-linearly. Thus, other quantities are affected as well. Our results suggest a minimum number of 8000 iterations.

– The Lattice Boltzmann Method requires large computing power, particularly given a accurate grid resolution and sufficient iteration steps. This hampers its use on standard personal computers. Parallel computing is a prerequisite for analysing more realistic porous beds where larger domain sizes and denser particle packings are encountered.

– The application of the LBM requires a quality check on resolutions and iteration steps. Average values of the lattice gas density and the velocity should be compared for different settings. However, for repeated investigations on similar geometries (e.g., only changing the number of objects in the DEM) one test is sufficient.

– The Path Tracking Method is beneficial as it is fast and easy to implement. It is free from conversion requirements. The only resolution dependency refers

to the number of initial starting points. However, a small number is sufficient to properly determine the domains tortuosity from individual pathways.

– PTM offers great advantage over any indirect way of calculating hydraulic tortuosity using flow velocities (independent of the specific method used) as it circumvents the requirement to calculate the velocity field in the pore space of the media.

Table 3

Summary and comparison of features of Lattice Boltzmann Method (LBM) and the Path Finder Method (PFM) for calculating tortuosity starting from grain bed geometry (defined by geometric parameters)

Feature	LBM	PTM
Geometry conversion	required pre-processing step; increases computation time; requires additional software for geometry conversion	not required
Porosity	depends on grid resolution; may also depend on conversion algorithm used	analytically calculated
Tortuosity	calculated indirectly; depend on multiple factors as grid resolution, iterations, choice of LBM model, numerical model settings	calculated from geometry; directly related to flow path, provides individual values within domain
Computational demand	very high (for calculations and visualisation)	very low
Computation time	very long	very short (depending on number of starting points)
Software	Pre-processing tool; Lattice Boltzmann solver; postprocessing tool	Path Finder (no further software required)

The publication was written during the first author's internship at Utrecht University, co-financed by the European Union under the European Social Fund (Operational Program Knowledge Education Development), carried out in the project Development Program at the University of Warmia and Mazury in Olsztyn (POWR.03.05. 00-00-Z310/17).

References

AFKHAMI M., HASSANPOUR A., FAIRWEATHER M., NJOBUENWU D.O. 2015. *Fully coupled LES-DEM of particle interaction and agglomeration in a turbulent channel flow*. Computers and Chemical Engineering, 78: 24-38.

AL-ARKAWAZI S., MARIE C., BENHABIB K., COOREVITS P. 2017. *Modeling the hydrodynamic forces between fluid-granular medium by coupling DEM-CFD*. Chemical Engineering Research and Design, 117: 439-447.

BEAR J. 1972. *Dynamics of Fluids in Porous Media*. Courier Dover Publications, New York.

BHATNAGAR P.L., GROSS E.P., KROOK M. 1954. *A model for collisional processes in gases I: small amplitude processes in charged and neutral onecomponent system*. Physical Review, 94(3): 511-524.

CARMAN P.C. 1937. *Fluid Flow through Granular Beds*. AIChE, 15: 150.

CATALANO E. 2012. *A pore- coupled hydromechanical model for biphasic granular media*. Ph.D. Thesis, Grenoble University, France.

CHEN F. 2009. *Coupled Flow Discrete Element Method Application in Granular Porous Media using Open Source Codes*. Ph.D. Thesis, University of Tennessee, Knoxville, USA.

CIESZKO M. 2009. *Description of anisotropic pore space structure of permeable materials based on Minkowski metric space*. Arch. Mech., 61(6): 425-444.

CIESZKO M., KRIESE W. 2006. *Description of tetragonal pore space structure of porous materials*. Arch. Mech., 58(4-5): 477-488.

CUNDALL P.A., STRACK O.D. 1979. *A discrete element model for granular assemblies*. Géotechnique, 29: 47-65.

DUDA A., KOZA Z., MATYKA M. 2011. *Hydraulic tortuosity in arbitrary porous media flow*. Physical Review, E, 84: 036319.

ERATH C. 2010. *Coupling of the Finite Volume Method and the Boundary Element Method*. Ph.D. Thesis, University Ulm, Germany.

FENG Y.T., HAN K., OWEN D.R.J. 2007. *Coupled lattice Boltzmann method and discrete element modelling of particle transport in turbulent fluid flows: Computational issues*. International Journal for Numerical Methods in Engineering, 72: 1111-1134.

Free Software Foundation. 2019. https://www.fsf.org/ (access: 10.02.2020).

GALINDO-TORRES S.A. 2013. *A coupled Discrete Element Lattice Boltzmann Method for the simulation of fluid-solid interaction with particles of general shapes*. Computer Methods in Applied Mechanics and Engineering, 265: 107-119.

GHAREDAGHLOO B., PRICE J.S., REZANEZHAD F., QUINTON W.L. 2018. *Evaluating the hydraulic and transport properties of peat soil using porenetwork modeling and X-ray micro computed tomography*. Journal of Hydrology, 561: 494-508.

KOMORÓCZI A., ABE S., URAI J.L. 2013. *Meshless numerical modeling of brittle – viscous deformation: first results on boudinage and hydrofracturing using a coupling of discrete element method (DEM) and smoothed particle hydrodynamics (SPH)*. Computational Geosciences, 17(2): 373-390.

KOPONEN A., KATAJA M., TIMONEN J. 1996. *Tortuous flow in porous media*. Phys. Rev. E, 54: 406.

KOPONEN A., KATAJA M., TIMONEN J. 1997. *Permeability and effective porosity of porous media*. Phys. Rev. E, 56: 3319.

LINDNER S. 2015. *SiLibeads Glass beads Type S, Microglass beads*. Product Data Sheet, Version V13. http://www.tecmos.com/wp-content/uploads/2018/05/SiLibeads-Type-S.pdf.

MAHABADI O.K. LISJAK A., HE L., TATONE B.S.A., KAIFOSH P., GRASSELLI G. 2016. *Development of a New Fully-Parallel Finite-Discrete Element Code: Irazu*. ARMA, 16: 516.

MAREK M. 2014. *CFD modelling of gas flow through a fixed bed of Raschig rings*. Journal of Physics, Conference Series, 530: 012016.

MARKAUSKAS D., KRUGGEL-EMDEN H., SIVANESAPILLAI R., STEEB H. 2017. *Comparative study on mesh-based and mesh-less coupled CFD-DEM methods to model particle-laden flow*. Powder Technology, 305: 78-88.

MARKL M. 2015. *Numerical Modeling and Simulation of Selective Electron Beam Melting Using a Coupled Lattice Boltzmann and Discrete Element Method*. Ph.D. Thesis, Friedrich-Alexander-University Erlangen-Nuremberg, Germany.

Mayavi: 3D scientific data visualization and plotting in Python. 2020. MayaVi. https://docs.enthought.com/mayavi/mayavi/ (access: 10.02.2020).

NABOVATI A., SOUSA A.C.M. 2007. *Fluid Flow Simulation in Random Porous Media at Pore Level Using Lattice Boltzmann Method*. In: *New Trends in Fluid Mechanics Research*. Eds. F.G. Zhuang, J.C. Li. Springer, Berlin, Heidelberg.

NORDBOTTEN J.M. 2014. *Finite volume hydromechanical simulation in porous media*. Water Resources Research, 50(5): 4379-4394.

Palabos. 2020. Universite de Geneve. http://www.palabos.org/ (access: 10.02.2020).

ParaView. 2020. http://www.paraview.org/ (access: 10.02.2020).

QIU L.-C. 2015. *A Coupling Model of DEM and LBM for Fluid Flow through Porous Media*. Procedia Engineering, 102: 1520-1525.

ROJEK J. 2007. *Multiscale analysis using a coupled discrete/finite element model*. Interaction and Multiscale Mechanics, 1(1): 1-31.

SAKAI M. 2016. *How Should the Discrete Element Method Be Applied in Industrial Systems?* KONA Powder and Particle Journal, 33: 169-178.

SAOMOTO H., KATAGIRI J. 2015. *Direct comparison of hydraulic tortuosity and electric tortuosity based on finite element analysis*. Theoretical and Applied Mechanics Letters, 5(5): 177-180.

SOBIESKI W. 2009. *Calculating tortuosity in a porous bed consisting of spherical particles with known sizes and distribution in space*. Research report 1/2009, Winnipeg, Canada.

SOBIESKI W. 2016. *The use of Path Tracking Method for determining the tortuosity field in a porous bed*. Granular Matter, 18: 72.

SOBIESKI W., DUDDA W., LIPIŃSKI S. 2016a. *A new approach for obtaining the geometric properties of a granular porous bed based on DEM simulations*. Technical Sciences, 19(2): 165-187.

SOBIESKI W., LIPIŃSKI S. 2016. *PathFinder User's Guide*. University of Warmia and Mazury, Olsztyn.

SOBIESKI W., LIPIŃSKI S., DUDDA W., TRYKOZKO A., MAREK M., WIĄCEK J., MATYKA M., GOŁEMBIEWSKI J. 2016b. *Granular porous media*. University of Warmia and Mazury, Olsztyn.

SOBIESKI W., ZHANG Q., LIU C. 2012. *Predicting Tortuosity for Airflow Through Porous Beds Consisting of Randomly Packed Spherical Particles*. Transport Porous Med., 93(3): 431-451.

SRIVASTAVA S., YAZDCHI K., LUDING S. 2012. *Mesoscale dynamic coupling of finite- and discrete-element methods for fluid-particle interactions*. Philosophical Transactions of the Royal Society A, 372(2021): 1-18.

STRÁNSKÝ J., JIRÁSEK M. 2012. *Open source FEM-DEM coupling*. 18th International Conference Engineering Mechanics, Svratka, Czech Republic, May 14-17, Paper no 18, p. 1237-1251.

SUN W.C., KUHN M.R., RUDNICKI J.W. 2013. *A multiscale DEM-LBM analysis on permeability evolutions inside a dilatant shear band*. Acta Geotechnica, 8(5): 465-480.

ŠMILAUER V., CATALANO E., CHAREYRE B., DOROFEENKO S., DURIEZ J., DYCK N., ELIÁŠ J., ER B., EULITZ A., GLADKY A., GUO N., JAKOB CH., KNEIB F., KOZICKI J., MARZOUGUI D., MAURIN R., MODENESE CH., SCHOLTÈS L., SIBILLE L., STRÁNSKÝ J., SWEIJEN T., THOENI K., YUAN CH. 2020. *Yade Documentation*. 2nd Edition, after Release 2020-04-30.git-c3696f2. https://yade-dem.org/doc/Yade.pdf (access: 10.02.2020).

TRYKOZKO A., PESZYNSKA M., DOHNALIK M. 2016. *Modeling non-Darcy flows in realistic pore-scale proppant geometries*. Computers and Geotechnics, 71: 352-360.

VILLARD P., CHEVALIER B., LE HELLO B., COMBE G. 2009. *Coupling between finite and discrete element methods for the modelling of earth structures reinforced by geosynthetic*. Computers and Geotechnics, 36(5): 709-717.

WANG P. 2014. *Lattice Boltzmann Simulation of Permeability and Tortuosity for Flow through Dense Porous Media*. Math. Prob. Eng., 694350.

WIDULIŃSKI Ł., KOZICKI J., TEJCHMAN J. 2009. *Numerical Simulations of Triaxial Test with Sand Using DEM*. Archives of Hydro-Engineering and Environmental Mechanics, 56(3-4): 149-171.

WILLERT C.E., GHARIB M. 1991. *Digital particle image velocimetry*. Experiments in Fluids, 10(4): 181-193.

WU T.-R., HUANG C.-J., CHUANG M.-H., WANG C.-Y., C.-R. CHU C.-R. 2011. *Dynamic coupling of multi-phase fluids with a moving obstacle*. Journal of Marine Science and Technology, 19(6): 643-650.

XIANG J., LATHAM J.P., VIRE A., ANASTASAKI E, PAIN C.C. 2012. *Coupled fluidity/y3d technology and simulation tools for numerical breakwater modelling*. Coastal Engineering Proceedings, 33: 1-9.

ZENG Q., YAO J. 2015. *Numerical Simulation of Fluid-Solid Coupling in Fractured Porous Media with Discrete Fracture Model and Extended Finite Element Method*. Computation, 3: 541-557.

ZHAO J., SHAN T. 2013. *Coupled CFD–DEM simulation of fluid – particle interaction in geomechanics*, Powder Technology, 239: 248-258.

Technical Sciences, 2020, 23(1), 53–67

UNIWERSYTET WARMIŃSKO-MAZURSKI W OLSZTYNIE

Quarterly peer-reviewed scientific journal
ISSN 1505-4675
e-ISSN 2083-4527
TECHNICAL SCIENCES
Homepage: www.uwm.edu.pl/techsci/

doi: 10.31648/ts.5125

THE APPLICATION OF THE RESPONSE SURFACE METHOD (RSM) TO OPTIMIZE THE CONDITIONING OF PRIMITIVE RYE GRAIN KRZYCA (*SECALE CEREALE* VAR. *MULTICAULE*) BEFORE MILLING

***Stanisław Konopka*[1], *Beata Piłat*[2]**

[1]ORCID: 0000-0002-8826-9308
Faculty of Technical Sciences
University of Warmia and Mazury in Olsztyn
[2]ORCID: 0000-0002-6771-2753
Faculty of Food Sciences
University of Warmia and Mazury in Olsztyn

Received 17 February 2020; Accepted 15 April 2020; Available online 27 April 2020.

K e y w o r d s: rye, conditioning, flour yield, ash content, falling number value, time of milling.

A b s t r a c t

The aim of the current study was to optimize the conditioning process of primitive rye, known as Krzyca in Polish, which has recently been reintroduced to farming. The experiment was conducted according to the Box-Behnken model with three independent variables: the temperature of water used for grain conditioning (10, 15, 20°C), the duration of the conditioning process (4, 10, 16 h) and the final grain moisture content (13, 14, 15%). In the obtained flours, four dependent variables were determined (time of grain milling, yield of extraction flour, ash content of flour and falling number value). The obtained polynomial equations and the response surface method point to the significance of the ranges of independent values, with the highest impact noted for flour ash and falling number values.

Correspondence: Stanisław Konopka, Katedra Maszyn Roboczych i Metodologii Badań, Wydział Nauk Technicznych, Uniwersytet Warmińsko-Mazurski, ul. M. Oczapowskiego 11, 10-719 Olsztyn, e-mail: stanisław.konopka@uwm.edu.pl

Introduction

Common rye (*Secale cereale*) is an economically important crop in Poland and the European Union, mainly used for the production of bread (KONOPKA et al. 2017, WARECHOWSKA et al. 2019). Rye flour contains less gluten-type proteins, while more healthy pentosans and dietary fiber (BUKSA et al. 2012, BUSHUK 2001, GĄSIOROWSKI 1994, SZAFRAŃSKA 2011, VEJRAŽKA et al. 2012). According to Central Research Center for Crop Plants in Poland (*Lista odmian roślin…* 2019) there are 66 varieties of winter rye currently in the Polish National Register, appearing as population or hybrid plants.

In recent years, however, there has been an increase in consumer interest in traditional and regional foods. Thus, the original crop species have returned to cultivation. One of the priorities of the rural development program in Poland (Program Rozwoju Obszarów Wiejskich – PROW) for 2014-2020 is to restore, protect and strengthen ecosystems dependent on agriculture and forestry. Agri-environment-climate operations under the Package 6 PROW have been focused, among others, on the protection of endangered plant genetic resources in agriculture (PAJĄKOWSKI 2015). Among the species of local varieties of cultivated plants supported under this Package is rye krzyca (latin names *Secale cereale* var. *multicaule/Secale montanum* Guss.) (PAJĄKOWSKI 2015). Krzyca rye (other forms of dialect names are "ikrzyca" and "skrzyca") is a genetically older, untreated form of winter rye, cultivated widely until the nineteenth century throughout Central Europe (CHRZĄSZCZ 2020, KOWALSKA-LEWICKA 2016). Due to the low grain yields (1.5-3.0 t ha^{-1}), the dark color of the grain and its easy falling out from the ear, this species was, however, displaced in the 20^{th} century by modern rye (CHRZĄSZCZ 2020).

Currently, krzyca rye is returning to cultivation, but information on the grain composition, and its technological, milling and baking quality is very scarce. In recent years, KONOPKA et al. (2017) compared the technological quality and content of selected bioactive ingredients in the grain of krzyca and common rye from organic farming. These studies have shown that both species have comparable baking value, while the grain of krzyca contains more protein, total free phenolic compounds, total phenolic acids, flavonoids, sterols, tocols and carotenoids than common rye (KONOPKA et al. 2017). A recent study of this primitive rye also showed that this grain has shorter kernels, lower thousand-kernel weight and a higher contribution of redness in surface color, while grain mechanical features during compression and specific energy of milling are intermediate between open-pollinated and hybrid rye cultivars (WARECHOWSKA et al. 2019).

In the processing of cereal grains for baking purposes, an important element is the assessment of its milling properties, determined *inter alia* by flour extraction and its ash content (STĘPNIEWSKA, ABRAMCZYK 2011, STĘPNIEWSKA 2016). These distinguishing features depend on the participation of individual

morphological parts in the grain (seed coat, aleurone layer, endosperm) and the conditions used to prepare the grain for milling, i.e. conditioning (JANKOWSKI 1981). Conditions conducive to achieving the highest flour extract (with as low ash as possible) were developed for bread cereal grains in the 1950s and 1960s (JANKOWSKI 1981). At present, they form the practical knowledge of mill workers that have adapted them into the dominant common cultivars of *Triticum aestivum* and *Secale cereale*. In turn, ancient species, currently reintroduced for agriculture and processing, due to the different physicochemical properties of grain require research, including optimizing the conditions for their conditioning before milling.

The current study analyzed the optimum conditions for conditioning krzyca grain before milling under the influence of three input parameters (independent variables): water temperature for conditioning the grain, conditioning time and grain moisture after conditioning to determine how they affect: grain milling time, flour extraction yield, ash content and flour falling value of extraction krzyca flour (dependent variables).

Materials and methods

The research material was krzyca rye grain (supplier of BIOSFERA Trade Olsztyn). Krzyca grain had an initial moisture of 10.27%, ash content 1.78% dry matter and a mass of 1,000 kernels equal to 22.4 g. The experiment was conducted according to the Box-Behnken model with the above variables at three levels, which resulted in 15 measuring points for normalized (-1, 0, +1) values of input quantities (DERRINGER, SUICH 1980). The real values of experimental factors (independent variables) were selected as: the temperature of water used to conditioning (10, 15, 20°C), the final moisture of conditioned grain (13, 14, 15%) and the time of conditioning (4, 10, 16 h). The ranges of independent variables used were selected using the classic values for traditional rye grain (JANKOWSKI 1981, GĄSIOROWSKI 1994). Real values assigned to the code (-1, 0, +1) corresponded to the sequence from the lowest to the highest factor level. Dependent variables were: time of milling [s], flour yield [%], ash content of flour [%] and falling number value of flour [s]. Grain samples of 100 g after conditioning were ground in a laboratory mill AGROMATIC AQC 109 (Laupen Schweiz) with flour sifting module with a mesh diameter of 250 μm. Main technical parameters of the mill are: number of grooves in rollers from 5 to 20/cm; dimensions of rollers – diameter 7 cm, width 3 cm; revolutions of rollers 1 and 3 – 970 rpm; revolutions of rollers 2 and 4 – 420 rpm. Gaps between rollers is factory set and diminish from 0.8 mm to 0.02 mm. The grinding time was measured using a stopwatch from the moment of opening the grain feeding slide until the last grain was milled. Moisture content of grain was determined according to PN-EN ISO 712:2012

standard, using thermal testing chamber KBC 100 (Wamed, Poland) set at 131°C. Before this assay grain was carefully ground in an A10 IKA Labortechnik mill (Staufen, Baden-Wurttemberg, Germany). Ash content of grain and obtained flours was determined according to PN-EN ISO 2171:2010 standard, using a laboratory muffle furnace (AB Utenos Elektrotechnika, Lithuania) set at 900°C. Falling number value was determined using 1600 device (Perten Instruments, Sweden) according to PN-EN ISO 3093:2010 standard. 1000-kernel weight was determined with the use of an electronic kernel counter (Kernel Counter LN S 50A, Unitra CEMI, Poland) and an electronic scale (WPE 120, Radwag, Poland).

The results of the experiments were used to develop the models of four dependent variable changes according to the 2-nd polynomial equation (without interaction effects):

$$\hat{Y}_i = b_0 + b_1X_1 + b_2X_2 + b_3X_3 + b_4X_1^2 + b_5X_2^2 + b_6X_3^2 \quad (1)$$

where individual symbols mean:

$\hat{Y}_i$ – the estimated value of the next dependent variable (i = 1, 2, 3, 4),
b_0 – constant value in the equation,
X_1 – temperature of water used to conditioning [°C],
X_2 – final moisture of conditioned grain [%],
X_3 – time of conditioning [s],
$b_1 \div b_6$ – value of the relevant coefficient.

The response (function utility) profiles are presented in the form of contour areas of the plane illustrating the values of total usability of the response calculated for input values defined by various combinations. The response surface method (RSM) used allows for a relative distinction between the components of the "active" and "passive" of equations. At the same time, it allows users to specify stochastic models between dependent and independent variables. The suitability of individual models for predicting the variability of a given dependent variable, depending on statistically significant independent variables, was determined on the basis of a statistical scale of values R-squared (R^2) and adjusted R-square (adj.-R^2) (STANISZ 1998). Additionally, milling efficiency index (ratio of flour yield to flour ash content) was calculated. Analysis of variance (with Duncan's tests) was used to determine significant differences between tested variants.

All statistical calculations were carried out at a significance level of $\alpha = 0.05$ with STATISTICA v.13.1 software (StatSoft, Inc. Poland).

Results and discussion

The list of actual real values of independent variables used in the generated Box-Behnken model (3-factor variant) and the obtained experimental results are presented in Table 1.

Table 1

Real values of independent variables of conducted experiment in Box-Behnken model and results of determined final results of experiments

Variant of the experiment	Independent variables			Dependent variables			
	temperature of water used to conditioning [°C]	final moisture of conditioned grain [%]	time of conditioning [h]	time of milling [s]	flour yield [%]	ash content of flour [%]	falling number value of flour [s]
1	10	13	10	56	42.5	0.695	190
2	20	13	10	60	42.8	0.729	219
3	10	15	10	67	33.6	0.683	246
4	20	15	10	66	34.0	0.708	227
5	10	14	4	64	41.0	0.491	203
6	20	14	4	66	38.2	0.569	206
7	10	14	16	70	44.5	0.467	237
8	20	14	16	61	39.9	0.409	254
9	15	13	4	66	41.2	0.670	250
10	15	15	4	78	37.8	0.650	241
11	15	13	16	60	40.9	0.608	246
12	15	15	16	64	39.0	0.630	236
13	15	14	10	62	37.4	0.545	244
14	15	14	10	66	38.2	0.493	242
15	15	14	10	72	39.4	0.539	237

The first analyzed feature was the time of milling krzyca grain which, depending on the conditioning conditions (variant of the experiment), varied from 56 s to 78 s for the milling of 100 g of grain sample. Table 1 shows that in variant 10 (15°C, 15%, 10 h) it was more than 40% longer than in variant 1 (10°C, 13%, 10 h). Simultaneously, the data presented in Figure 1 and Table 2 indicate that the only significant independent variable affecting this parameter (except for the constant value) was the final moisture of conditioned grain, which value of the linear dependency coefficient (b_2) was statistically significant. Generally, an increase in milling time in the range of 13-15% was observed along with the increase in the final moisture of the krzyca grain. Finally, the equation

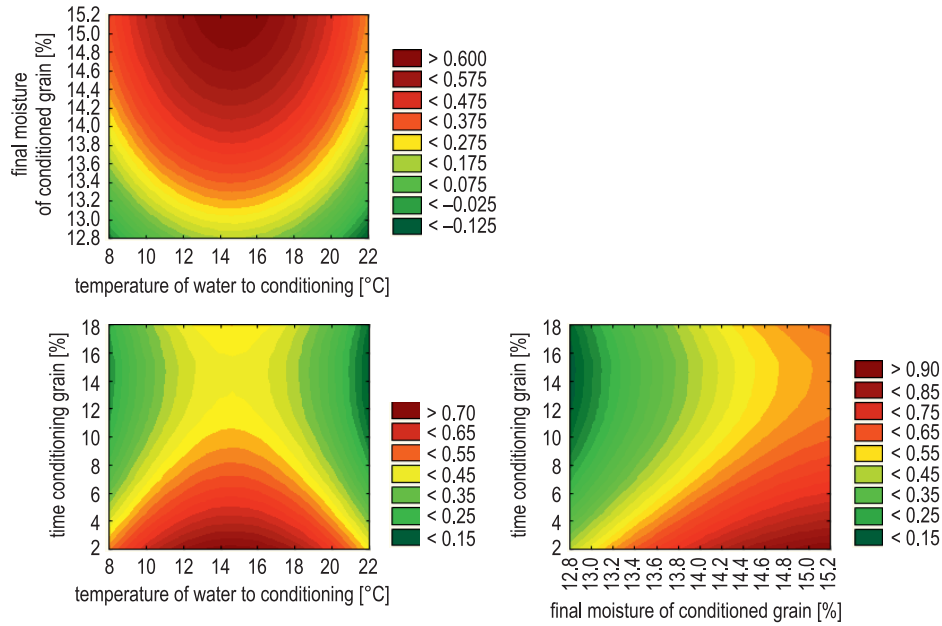

Fig. 1. Contour plot of plane areas illustrating levels of overall desired response variability of dependent variable -Y_1 (time of milling of 100 g of the sample) produced in different areas of the plane defined by values of pairs of independent variables

Table 2

The results of the assessment of the significance of the regression equation coefficients for milling time of 100 g of the sample

Constant value/ Independent variables	Value of the coefficient	Value of the *t*-test	Standard error for the coefficient	Probability value
Constant value	64.833	48.589	1.3343	0.0000
X_1 – temperature of water used to conditioning [°C] (*L*)	-0.500	-0.3059	1.6341	0.7674
X_1 – temperature of water used to conditioning [°C] (*Q*)	1.541	1.281	1.2027	0.2358
X_2 – final moisture of conditioned grain [%] (*L*)	4.125	2.524	1.6341	0.0355
X_2 – final moisture of conditioned grain [%] (*Q*)	0.666	0.554	1.2027	0.5945
X_3 – time of conditioning [s] (*L*)	-2.375	-1.453	1.6341	0.1842
X_3 – time of conditioning [s] (*Q*)	-0.833	-0.692	1.2027	0.5080

effect evaluation: variable – time of milling [s]; R^2 = 0.5815, adj.-R^2 = 0.2676, mean square MS = 21.36458.
L – linear effect, *Q* – quadratic effect.

presents the mathematical relationship between the milling time of the sample and statistically significant independent variables (2):

$$\hat{Y}_1 = 64.833 + 4.125\, X_2 \tag{2}$$

However, the values of the coefficient of determination ($R^2 = 0.5815$) and adjusted coefficient of determination (adj.-$R^2 = 0.2676$) for this equation indicate the relatively small impact of other independent variables and poor practical possibilities to use this model to predict the value of the dependent variable in question (STANISZ 1998). In the presented experiment, the shortest, and thus the most energy-efficient milling time was found in variant 1, which was characterized by the lowest temperature of water used for conditioning, the lowest final moisture of conditioned grain and average time of conditioning (10°C, 13%, 10 h).

Grain milling is one of the most energy-consuming processes in cereal grain processing. In the industrial processing, about 60-75% of the total energy is associated with this technological operation stage (DANCIU et al. 2009). Extending the milling time of a grain batch leads to an increase in the energy input for milling. Rationalization of energy consumption in the plant is a conscious action aimed at reducing it without reducing the quality and volume of production. It is estimated that in industrial plants, a 20% reduction in electricity consumption results in a 15% reduction in the fee paid (KIRYLUK et al. 2010). Energy expenditure in the milling process depends on the type of mill used, mill settings and the physicochemical properties of the grain and the degree of grinding (DZIKI, LASKOWSKI 2002, DZIKI 2008, WIERCIOCH, NIEMIEC 2006, WIERCIOCH et al. 2008). Most research in this field concerns the impact of grain moisture and hardness on energy consumption (WARECHOWSKA 2014). Numerous researchers have noted that as grain moisture increases, energy consumption in grinding increases (more details in WARECHOWSKA 2014). Moist grains become less brittle and more plastic, which results in less susceptibility of the endosperm to comminution into flour particles (JANKOWSKI 1981).

The next measured feature was the flour extraction yield, which varied from 33.6% to 44.5%, respectively in variants 3 (10°C, 15%, 10 h) and 7 (10°C, 14%, 16 h) of the experiment (Tab. 1). This indicates that in variant of the experiment 7 it was approx. 33% higher compared to variant 3. The data presented in Figure 2 and Table 3 also indicate that the only significant independent variable (except for the constant value) affecting this parameter was the final moisture of conditioned grain, whose value of the coefficient (b_2) was statistically significant. Along with an increase in the moisture content of krzyca grain in the range of 13-15%, a linear decrease in flour extraction yield was observed. The equation describing the yield of flour from the krzyca grain as a function of statistically significant parameters (3) has the following form:

$$\hat{Y}_2 = 64.833 + 4.125X_2 \tag{3}$$

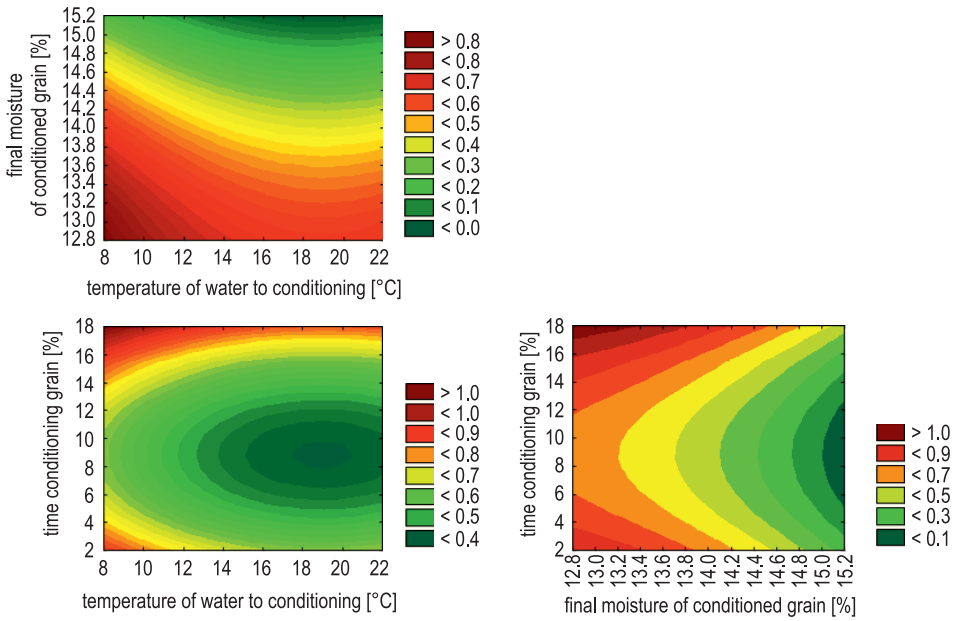

Fig. 2. Contour plot of plane areas illustrating levels of overall desired response variability of dependent variable -Y_2 (flour yield) produced in different areas of the plane defined by values of pairs of independent variables

Table 3

The results of the assessment of the significance of the regression equation coefficients for flour yield

Constant value / Independent variables	Value of the coefficient	Value of the t-test	Standard error for the coefficient	Probability value
Constant value	39.625	68.075	0.5820	0.0000
X_1 – temperature of water used to conditioning [°C] (L)	-0.855	-1.199	0.7129	0.2647
X_1 – temperature of water used to conditioning [°C] (Q)	-0.268	-0.512	0.5246	0.6220
X_2 – final moisture of conditioned grain [%] (L)	-2.873	-4.031	0.7129	0.0037
X_2 – final moisture of conditioned grain [%] (Q)	0.319	0.609	0,5246	0.5591
X_3 – time of conditioning [s] (L)	0.761	1.067	0.7129	0.3167
X_3 – time of conditioning [s] (Q)	-1.010	-1.925	0.5246	0.0903

effect evaluation: variable – flour yield [%], $R^2 = 0.7443$, adj.-$R^2 = 0.5527$, mean square MS = 4.065927.
L – linear effect, Q – quadratic effect.

The determination coefficient (R^2 = 0.7443) value and adjusted coefficient of determination (adj.-R^2 = 0.5527) for this equation are determined on a statistical scale as high, which indicates significant possibilities of using this model to predict the value of the dependent variable in question.

The extraction flour yield from cereal grains is determined by the share of the main morphological parts of the grain. Rye flour extract is lower than wheat flour and usually does not exceed 64-65% for modern rye (ROSENTRATER, EVERS 2018). The main reason is the fact, that it is difficult to separate rye endosperm from the seed coat in grain with a high content of non-starch polysaccharides (WARECHOWSKA et al. 2019). The highest flour extract can be obtained from grain with a high proportion of starch endosperm (GĄSIOROWSKI 1994) and the share of starch endosperm is positively correlated with a mass of 1,000 kernels (SCHULER et al. 1995). However, the grain of krzyca is relatively small and has a significantly lower mass of 1000 kernels (by about 25%) than traditional rye (own research and WARECHOWSKA et al. 2019). This indicates that the flour extract obtained in variant 7 of the experiment (44.5%) is probably close to the maximum, although a higher yield of extraction flour of this primitive rye flour (49.8%) was obtained by WARECHOWSKA et al. (2019). In the cited work, the extraction rate of flour of krzyca grain was similar to that of hybrid rye (48.9%) and was significantly lower than the extraction rate of flour from open-pollinated rye (53.5%).

The ash content of rye grain can range widely from 1.43% to 2.42% of dry matter (STĘPNIEWSKA et al. 2018, 2019). For the krzyca grain in this study, it was 1.78% of dry matter. The ash content of the obtained extraction flours varied from 0.409% to 0.729% of dry matter (Tab. 1). These values corresponded to the relatively low extraction rates of obtained flours. The data analysis presented in Figure 3 and Table 4 shows that the variability of ash content in krzyca extraction flours is significantly affected by: a constant value, the final moisture of conditioned grain (quadratic effect) and the time of conditioning (linear and quadratic effects). Finally, the functional relationship between ash content and statistically significant independent variables can be written as:

$$\hat{Y}_3 = 0.609 - 0.083X_2^2 - 0.033X_3 + 0.026X_3^2 \quad (4)$$

and very high values of the coefficient of determination (R^2 = 0.9390) and adjusted coefficient of determination (adj.-R^2 = 0.8933) for this equation indicate its suitability for predicting the discussed variable value.

The obtained results showed that the lowest level of ash content in krzyca extraction flour can be obtained by milling the grain at ca 14% of the final moisture and a relatively long time of conditioning is preferable (above 16 h). These conditions lead to making the coat of krzyca grain more plastic, which has become less susceptible to crushing during milling (JANKOWSKI 1981, GĄSIOROWSKI 1994). Currently preferable in the diet are wholemeal flours, but there is still

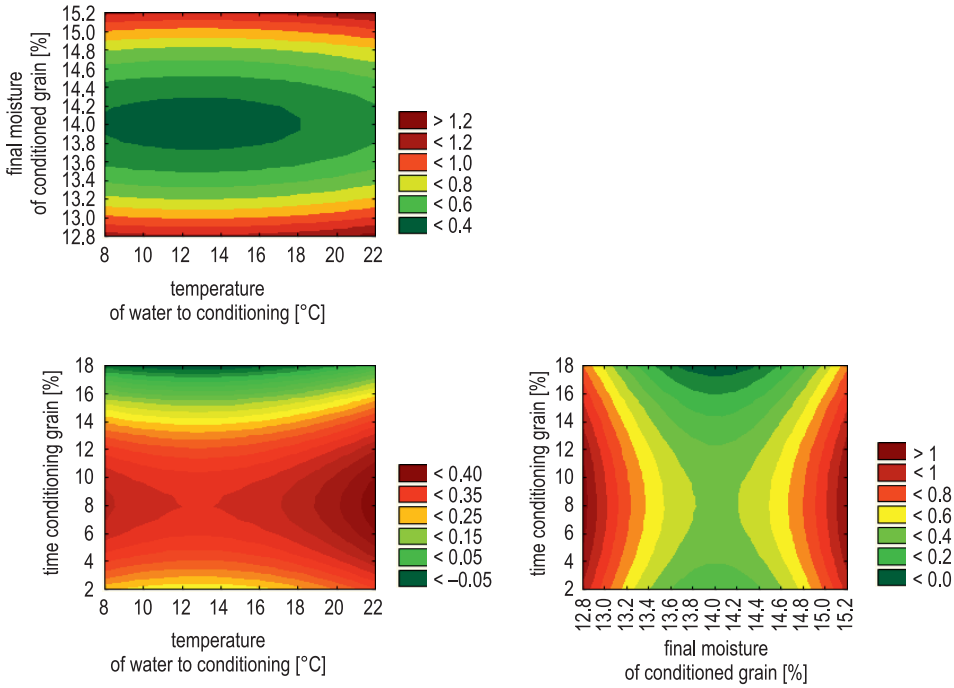

Fig. 3. Contour plot of plane areas illustrating levels of overall desired response variability of dependent variable Y_3 (ash content of flour) produced in different areas of the plane defined by values of pairs of independent variables

Table 4

The results of the assessment of the significance of the regression equation coefficients for ash content of flour

Constant value / Independent variables	Value of the coefficient	Value of the t-test	Standard error for the coefficient	Probability value
Constant value	0.609	65.317	0.0093	0.0000
X_1 – temperature of water used to conditioning [°C] (L)	0.010	0.864	0.0114	0.4124
X_1 – temperature of water used to conditioning [°C] (Q)	-0.006	-0.671	0.0084	0.5207
X_2 – final moisture of conditioned grain [%] (L)	-0.004	-0.339	0.0114	0.7431
X_2 – final moisture of conditioned grain [%] (Q)	-0.083	-9.921	0.0084	0.0000
X_3 – time of conditioning [s] (L)	-0.033	-2.911	0.0114	0.0195
X_3 – time of conditioning [s] (Q)	0.026	3.150	0.0084	0.0135

effect evaluation: variable – ash content of flour [%], $R^2 = 0.9390$, adj.-$R^2 = 0.8933$, mean square MS = 0.00104.
L – linear effect, Q – quadratic effect.

a need to produce relatively pure, refined baking flours for special baking and culinary needs. In this context, extraction flour of krzyca rye exhibits better pro-healthy properties than traditional rye grain (KONOPKA et al. 2017).

Based on flour yield and its ash content milling efficiency index (MEI) was calculated and presented on Figure 4 (to compare the values was used variance analysis ANOVA). In general, the higher MEI value the better the milling value (DZIKI et al. 2012). The highest MEI values (95.3 and 97.6) were determined for variants 7 and 8, respectively, characterized by medium final moisture of conditioned grain (14%) and the longest time of conditioning (16 h). In contrast, the lowest MEI values (49.2 and 48.0) were found for variants 3 and 4, respectively, characterized by the highest final moisture of conditioned grain (15%) and the medium time of conditioning (10 h). Temperature of water used to conditioning had no significant effect on MEI values.

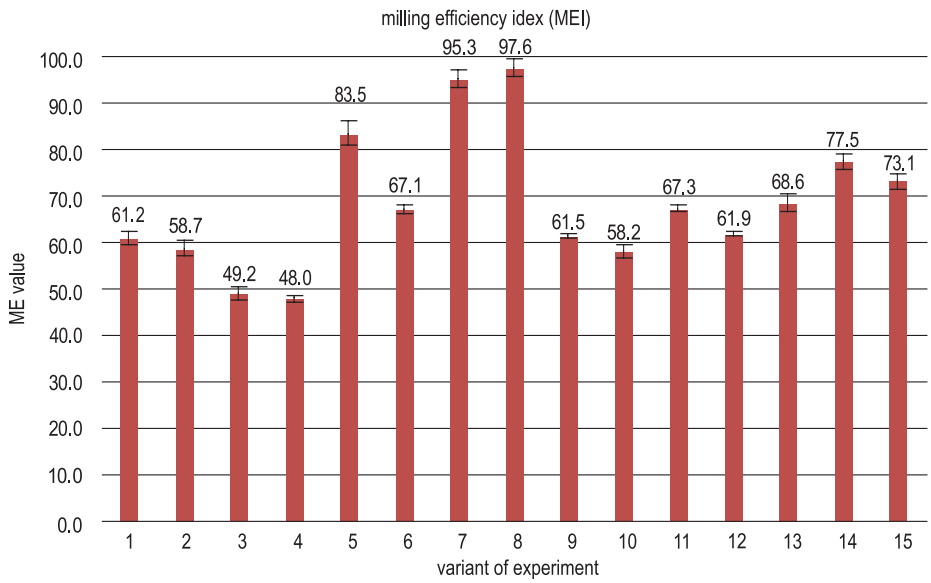

Fig. 4. Milling efficiency index (MEI) of obtained flours from tested variants of experiment – the values marked in superscript with different letters are significantly different ($\alpha = 0.05$)

The last analyzed feature of krzyca extraction flours was the falling number value. This feature indirectly measures the viscosity of gelatinized flour sample and is related to α-amylase activity in grain (GĄSIOROWSKI 1994, STĘPNIEWSKA et al. 2018, WARECHOWSKA et al. 2019). This factor was analyzed to detect any possible undesirable impact of conditioning parameters on flour quality. Rye flour of good baking quality has falling number values in the range of 125-200 s (GĄSIOROWSKI 1994). Flours with falling number values above 250 s need additional sources of enhanced starch degrading activity.

The results of falling number values in krzyca flours are presented in Table 1. They varied from 190s in variant 1 (10°C, 13%, 10 h) to 254 s in variant 8 (20°C, 14%, 16 h). These results show the relatively good baking values of all produced extraction flours. The values of coefficients of an equation describing the relationship of the falling number value in relation to used independent variables are presented in Table 5. The values of this dependent variable (Y_4) are highly determined by: constant value, the temperature of water used for conditioning (quadratic effect), the final moisture of conditioned (linear effect) and the time of conditioning (linear effect). The general (stochastic) model of this relationship is represented by the equation (5):

$$\hat{Y} = 229.583 + 9.688X_1^2 + 9.083X_2 + 12.917X_3 \quad (5)$$

The very high values of R-squared (R^2 = 0.9949) and adjusted R-square (adj.-R^2 = 0.9641) for this equation they show that the predictors determined largely explain the variability values of the dependent variable in question.

The medium temperature of the water for conditioning, prolonged conditioning duration and the higher final moisture of conditioned grain resulted in an enhanced level of falling number values (Fig. 5). It is a rather unexpected phenomenon (the reverse trend was expected), but krzyca grain differs in chemical composition from traditional rye grain (KONOPKA et al. 2017, WARECHOWSKA et al. 2019) and this variation can affect the obtained results.

Table 5

The results of the assessment of the significance of the regression equation coefficients for falling number value of flour

Constant value / Independent variables	Value of the coefficient	Value of the t-test	Standard error for the coefficient	Probability value
Constant value	229.583	220.577	1.0408	0.0000
X_1 – temperature of water used to conditioning [°C] (L)	3.333	2.481	1.3437	0.1313
X_1 – temperature of water used to conditioning [°C] (Q)	9.688	10.326	0.9382	0.0092
X_2 – final moisture of conditioned grain [%] (L)	9.083	6.760	1.3437	0.0212
X_2 – final moisture of conditioned grain [%] (Q)	0.563	0.599	0.9382	0.6097
X_3 – time of conditioning [s] (L)	12.917	9.613	1.3437	0.0106
X_3 – time of conditioning [s] (Q)	-1.688	-1.799	0.9382	0.2139

effect evaluation: variable – falling number value of flour [s], R^2 = 0.9949, adj.-R^2 = 0.9641, mean square MS = 13.05733.
L – linear effect, Q – quadratic effect.

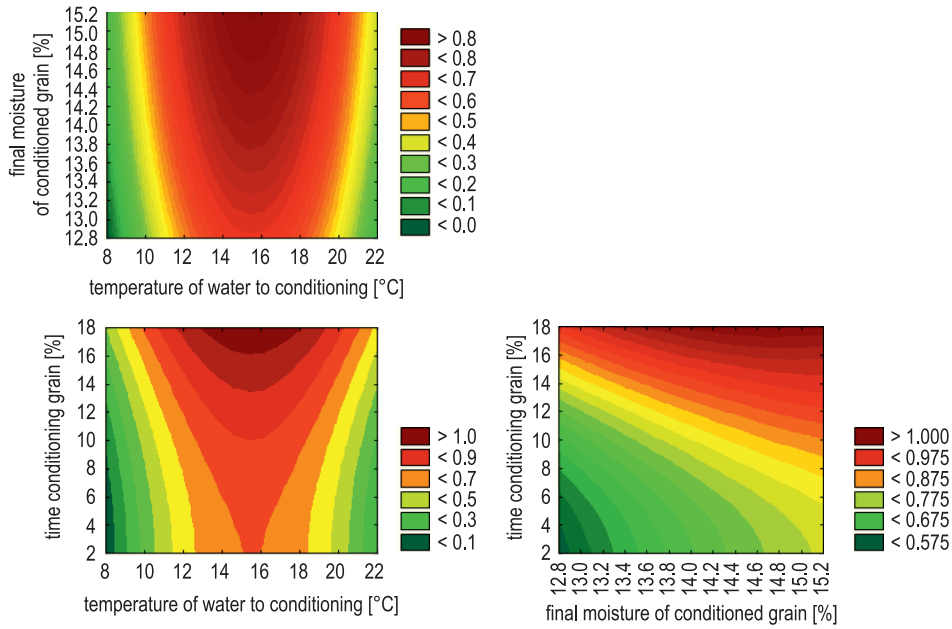

Fig. 5. Contour plot of plane areas illustrating levels of overall desired response variability of dependent variable Y_4 (falling number value of flour) produced in different areas of the plane defined by values of pairs of independent variables

Conclusions

The results of the presented study show that the milling properties of krzyca grain and the quality of obtained extraction flours can be affected by the conditions of grain conditioning. The time of grain milling increases primarily with an increase in the final moisture of conditioned grain (from range 13-15%). The rate of extraction flour is the lowest with a medium time of conditioning duration (10 h) and at an enhanced final moisture of conditioned grain (above 15%) and temperature of water used for conditioning (20°C). Flour ash content of flour seems to be minimized at the highest values of water temperature (20°C), time of conditioning (16 h) and a medium moisture of conditioned grain (14%). The highest milling efficiency indices were determined for variants characterized by medium final moisture of conditioned grain (14%) and the longest time of conditioning (16 h). A falling number value of flour is the lowest after the use of the coldest water (10°C); the lowest moisture of conditioned grain (13%) and medium time of conditioning (10 h). The highest impact of the used independent variables of condition was found for flour ash and flour falling number value.

References

Buksa K., Nowotna A., Gambuś H., Krawantka J., Sabat R., Noga M. 2012. *Analiza porównawcza i skład chemiczny ziarna wybranych polskich odmian żyta, pochodzących z trzech kolejnych lat uprawy*. Acta Agrophysica, 19(2): 265-276.

Chrząszcz A. b.d. *Krzyca – opis, właściwości i zastosowanie. Zboże krzyca ciekawostki.* Ekologia.pl. Zielono, pozytywnie, nowocześnie. Styl życia. Zdrowa żywność. https://www.ekologia.pl/styl-zycia/zdrowa-zywnosc/krzyca-opis-wlasciwosci-i-zastosowanie-zboze-krzyca-ciekawostki,22132.html (access: 12.02.2020).

Danciu I., Danciu C., Banu I., Vaduva M., Mester M. 2009. *Researches regarding the grinding resistance of the wheat grain*. Journal of Agroalimentary Processes and Technologies, 15(3): 393-395.

Derringer G., Suich R. 1980. *Simultaneous optimization of several response variables*. Journal of Quality Technology, 12: 214-219.

Dziki D. 2008. *The crushing of wheat kernels and its consequence on the grinding process*. Powder Technology, 185(2): 181-186.

Dziki D., Cacak-Pietrzak G., Biernacka B., Jończyk K., Różyło R., Gładyszewska B. 2012. *The grinding Energy as an indicator of wheat milling value*. TEKA. Commission of Motorization and Energetics in agriculture, 12(1): 29-33.

Dziki D., Laskowski J. 2002. *Wpływ wielkości ziarna na wybrane właściwości pszenicy*. Inżynieria Rolnicza, 5(38): 337-344.

Jankowski S. 1981. *Zarys technologii młynarstwa i kaszarstwa*. WNT, Warszawa.

Kiryluk J., Pawlak T., Borlikowska A. 2010. *Wykorzystanie analizy zużycia energii w młynach pszennych do obniżenia energochłonności produkcji*. Przegląd Zbożowo-Młynarski, 12: 34-36.

Konopka I., Tańska M., Skrajda M. 2017. *Evaluation of baking value and content of selected pro-healthy compounds in grain of primitive rye "krzyca"*. Przegląd Zbożowo-Młynarski, 4: 18–21.

Kowalska-Lewicka A. 2016. Krzyca – rys historii. Żyto krzyca (*Secale cereale* var. *multicereale*). G.R. Damazynka. http://www.krzyca.webity.pl/krzyca-historia/ (access: 12.02.2020).

Lista odmian roślin rolniczych wpisanych do krajowego rejestru w Polsce. Polish National List of Agricultural Plant Varieties. 2019. Centralny Ośrodek Badania Odmian Roślin Uprawnych. Słupia Wielka. http://www.coboru.pl/Publikacje_COBORU/Listy_odmian/lo_rolnicze_2019.pdf .

Pająkowski J. 2015. *Informator nt. starych odmian roślin rolniczych i ogrodniczych występujących na terenie Rzeczpospolitej Polskiej i możliwościach ich introdukcji do uprawy jako odmiany regionalne i amatorskie*. Ministerstwo Rolnictwa i Rozwoju Wsi, Warszawa. https://bankgenow.edu.pl/wp-content/uploads/2017/06/Informator-Stare-Odmiany-2015-min.compressed.pdf.

PN-EN ISO 2171:2010. *Ziarno zbóż i nasiona roślin strączkowych i ich przetwory. Oznaczanie zawartości popiołu metodą spalania*.

PN-EN ISO 3093:2010. *Pszenica, żyto i mąki z nich uzyskane, pszenica durum i semolina – Oznaczanie liczby opadania metodą Hagberga-Pertena*.

PN-EN ISO 712:2012. *Ziarno zbóż i przetwory zbożowe – Oznaczanie wilgotności – Metoda odwoławcza*.

Rosentrater K.A., Evers A.D. 2018. *Kent's Technology of Cereals*: *An Introduction for Students of Food Science and Agriculture*. Woodhead Publishing. https://doi.org/10.1016/C2014-0-02847-X.

Rye: Production, chemistry, and technology. 2001. Ed. W. Bushuk. American Association of Cereal Chemists, Inc. St. Paul, Minnesota, USA.

Schuler S.F., Bacon R.K., Finney P.L., Gbur E.E. 1995. *Relationship of test weight and kernel properties to milling and baking quality in soft red winter wheat*. Crop Science, 35(4): 949-953.

Stanisz A. 1998. *Przystępny kurs statystyki w oparciu o program STATISTICA PL na przykładach z medycyny*. StatSoft Polska Kraków, p. 1-362.

Stępniewska S. 2016. *Wartość przemiałowa ziarna wybranych odmian pszenicy ze zbiorów z lat 2012-2014*. Acta Agrophysica, 23(1): 105-117.

STĘPNIEWSKA S., ABRAMCZYK D. 2011. *Wartość przemiałowa i wypiekowa odmian pszenicy uprawianych w Polsce na podstawie oceny ziarna ze zbiorów lat 2006-2010*. Postępy Nauki i Technologii Przemysłu Rolno-Spożywczego, 66(3): 90-98.

STĘPNIEWSKA S., HASSON W.H., SZAFRAŃSKA A., CACAK-PIETRZAK G., DZIKI D. 2019. *Procedures for breadmaking quality assessment of rye wholemeal flour*. Foods, 8: 331. doi:10.3390/foods8080331.

STĘPNIEWSKA S., SŁOWIK E., CACAK-PIETRZAK G., ROMANKIEWICZ D., SZAFRAŃSKA A., DZIKI D. 2018. *Prediction of rye flour baking quality based on parameters of swelling curve*. European Food Research and Technology, 244: 989-997.

SZAFRAŃSKA A. 2011. *Ocena wartości wypiekowej mąki żytniej*. Postępy Nauki i Technologii Przemysłu Rolno-Spożywczego, 66(4): 5-18.

VEJRAŽKA K., FAMĚRA O., KOCOURKOVÁ Z., HASENAY S. 2012. *Selected grain physical properties of different rye varieties* (*Secale cereale*) *and milling quality*. Proceedings of the 6th International Congress Flour-Bread'11. 8th Croatian Congress of Cereal Technologists, Opatija, Croatia, 12-14 October, 2011, p. 461-466. Faculty of Food Technology Osijek, University of Josip Juraj Strossmayer.

WARECHOWSKA M. 2014. *Wybrane właściwości fizyczne ziarna zbóż a energochłonność rozdrabniania*. Inżynieria Rolnicza, 1(149): 239-249.

WARECHOWSKA M., WARECHOWSKI J., TYBURSKI J. SIEMIANOWSKA E., NAWROCKA A., MIŚ A., SKRAJDA-BRDAK M. 2019. *Evaluation of physicochemical properties, antioxidant potential and baking quality of grain and flour of primitive rye (Secale cereale var. Multicaule*). Journal of Food Science and Technology, 56: 3422.

WIERCIOCH M., NIEMIEC A. 2006. *Energochłonność procesu rozdrabnia pszenicy ozimej o różnej szklistości przy stosowaniu gniotownika i śrutownika walcowego*. Inżynieria Rolnicza, 11(86): 511-518.

WIERCIOCH M., NIEMIEC A., ROMAŃSKI L. 2008. *Wpływ wielkości ziarniaków pszenicy na energochłonność ich rozdrabniania*. Inżynieria Rolnicza, 5(103): 367-372.

Żyto, chemia i technologia. 1994. Ed. H. Gąsiorowski. PWRiL, Poznań.

Technical Sciences, 2020, 23(1), 69–80

UNIWERSYTET WARMIŃSKO-MAZURSKI W OLSZTYNIE

Quarterly peer-reviewed scientific journal
ISSN 1505-4675
e-ISSN 2083-4527
TECHNICAL SCIENCES
Homepage: www.uwm.edu.pl/techsci/

doi: 10.31648/ts.5177

THERMOVISION MEASUREMENTS OF TEMPERATURE ON THE TOOL-CHIP UPPER SIDE IN TURNING OF AISI 321 STEEL

Marian Bartoszuk

ORCID: 0000-0002-6964-6921
Faculty of Mechanical Engineering
Opole University of Technology

Received 24 February 2020, accepted 24 April 2020, available online 29 May 2020.

K e y w o r d s: cutting zone, temperature on the chip upper side, contact temperature, thermovision, infrared imaging.

A b s t r a c t

The article presents the results of thermovision tests of temperature distribution in the cutting zone. The tests were carried during orthogonal turning of AISI 321 austenitic steel without coolant. TNMA160408 inserts made of H10F carbide were selected as the cutting edges. In the study, special attention was paid to the method of determining the surface emissivity coefficient of the chip upper side. The maximum temperature values of the chip upper side determined from thermographic images were related to the average contact temperature measured by the natural thermocouple method. The results of the study indicate that the maximum temperature value of the chip upper side is proportional to the average contact temperature, and represents approximately 42-44% of its value. The results were illustrated graphically.

Correspondence: Marian Bartoszuk, Katedra Technologii Maszyn i Automatyzacji Produkcji, Wydział Mechaniczny, Politechnika Opolska, ul. Mikołajczyka 5, 45-271 Opole, phone: +48 77 449 84 61, e-mail: m.bartoszuk@po.edu.pl

Nomenclature

a_p – depth of cut [mm]
f – feed rate [mm/rev]
v_c – cutting speed [m/min]
t_k – average contact temperature [ºC]
$t_{W\max}$ – maximum temperature of the chip upper side [ºC]

Introduction

It is generally known that heat during the cutting process is generated in the primary plastic deformation zone and in the friction zone of the chip against the rake face of the cutting edge. The total amount of heat generated during the cutting process is extracted from the cutting zone by lifting together with the chip, moves to the tool cutting edge and in a negligible part flows into the workpiece (GRZESIK 2016, STEPHENSON, AGAPIOU 2016). The division of thermal streams depends both on the processing parameters and on the mutual ratio of thermo-physical properties of both tool and workpiece materials. By observing the temperature distribution in the cutting zone you get a lot of information about the cutting process itself, e.g. tool wear. Temperature distribution information can also be a valuable source of data to verify cutting simulation models. It is well known that it is difficult to measure the temperature in the cutting zone, and especially in the immediate vicinity of the contact zone. This is often done by placing a thermocouple inside the cutting edge (ANEIRO et al. 2008, YVONNET et al. 2006) but with carbide cutting edges it is not easy. Another interesting measurement technique was proposed by BASTI, OBIKAWA and SHINOZUKA (2007). To measure the average contact temperature, they used a thin thermocouple made by photolithography before applying a protective coating to the cutting edge rake face. Most often, however, the cutting temperature is measured by measuring the thermoelectric force generated at the contact between the cutting edge and the workpiece material (ABHANG, HAMEEDULLAH 2010, AKHIL et al. 2016, CEAU et al. 2010). However, this is the temperature averaged over the entire contact area, both at the rake face and clearance face. Recently, methods using IR radiation are gaining in importance. Initially, pyrometric measurements were predominant in cutting temperature measurements, but with time and the progress of electronics, thermographic and thermovision methods are becoming increasingly important (HEIGEL et al. 2017, ZHAO et al. 2018). They make it quite easy to determine the temperature distribution on the surfaces of the cutting zone, but they require a careful determination of the emissivity coefficient of the surface being tested. This necessity is due to the fact that the value of the surface emissivity coefficient has a significant impact on the measurement result (ARRAZOLA 2008, RECH 2006).

On the basis of literature data and own research results, it can be concluded that temperature measurements in the cutting zone still pose many research problems. The accuracy of the obtained measurement results depends primarily on the accuracy of the calibration of the measurement chain. In the case of thermovision measurements, the accuracy of the measurements depends on the accuracy of the determination of the emissivity coefficient of the observed surface.

This article presents problems related to thermovision measurements of temperature distribution on the surfaces of the cutting zone. Special attention has been paid to the temperature of the chip upper side as an important source of information about the cutting process itself. The sources of possible interferences and causes of measurement inaccuracies are also discussed. In the research, great emphasis was placed on developing the author's own method of determining the emissivity coefficient of the observed chip surface. Verification of the obtained results was based on the average contact temperature determined by the natural thermocouple method.

Research methodology

Workpiece and cutting tool materials

A case of dry orthogonal cutting of AISI321 austenitic steel with carbide cutting edges without protective coatings was selected for testing. The quality of the steel selected for testing was guaranteed by approval no. MEST944800/2010/. Regardless of this, the chemical composition of the steel was confirmed by laboratory tests. The results obtained are shown in Table 1. However, this steel has a high tendency to be reinforced by compression. After compression, the value of $R_{0.2}$ limit reaches 1080 to 1370 N/mm^2.

Table 1

Chemical composition of AISI 321 stainless steel

Element	Mn	Si	P	S	Cr	Ni	Mo	Cu	V	Al
% at.	1.63	0.66	0.007	0.014	17.31	9.29	0.36	0.43	0.062	0.025
Element	Ti	W	Co	Pb	Sn	As	B	N	Ca	Fe
% at.	0.309	0.029	0.116	<0.001	0.01	0.003	0.0013	<0.001	0.0017	69.70

The tests were carried out using the PTNGR 2020-16 tool holder ensuring orthogonal positioning of the TNMA 160408 cutting edge with a flat rake face (Tab. 2).

Table 2

Specification of the angles of the tool cutting edge

Cutting tool angle	Symbol	Value [°]
Normal rake	γ_n	-5
Normal clearance	α_n	5
Major tool cutting edge	κ_r	90
Inclination	λ_s	-6

As the material of the cutting edge, fine-grained H10F carbide recommended by the manufacturer, i.a., for processing steel, cast iron, stainless steel and heat-resistant alloys based on nickel, chromium and titanium with low cutting speeds and high feed rates, was adopted (*Narzędzia tokarskie* 2017).

Test stand

The tests were carried out on a stand based on a TUM-35D1 center lathe with a modernized drive system. During the tests, the values of the components of total cutting force, contact temperature and thermographic images of the cutting zone were measured and recorded. The average contact temperature was measured using the natural thermocouple method with a single cutting edge (ABHANG, HAMEEDULLAH 2010, CEAU et al. 2010). Thermographic images were collected using a JENOPTIK VarioCAM thermal imaging camera equipped with IRBIS 3 software dedicated to archiving and processing thermographic images.

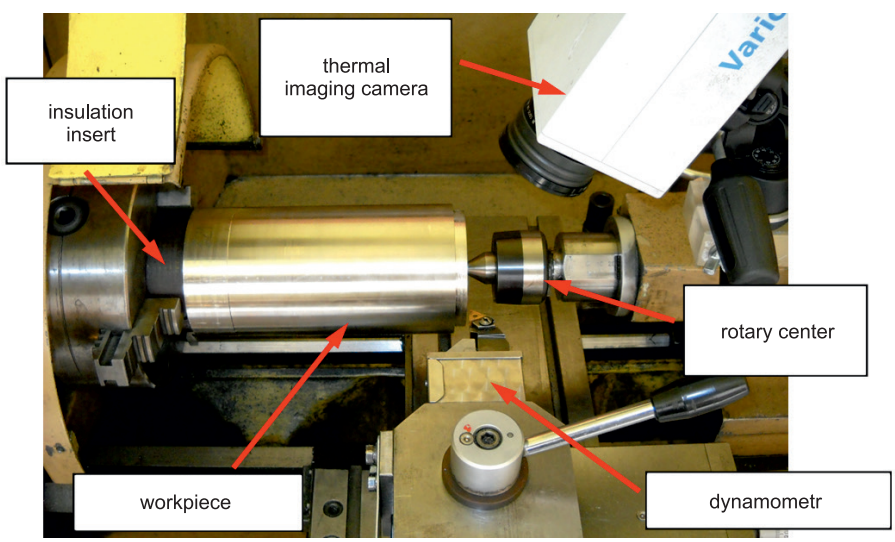

Fig. 1. View of the specimen in the processing space of the test stand

Experimental tests of the cutting process were carried out on specimens in the form of a cylinder with undercut forming a short pipe with a wall thickness of 2 mm. The location of the specimen in the test stand space is shown in Figure 1.

For the sake of recording of the tested signals a National Instruments NI 9237 measurement card and LabVIEW software were used. The selected software allowed for easy construction and adaptation of existing measurement chains to the needs of the conducted research.

Process conditions

The turning tests were carried out for orthogonal cutting, without coolant, with H10F carbide cutting edges, without protective coatings. The following processing conditions are assumed:

– cutting speed v_c = 66.67, 86.33, 100.00, 116.67, 133.33, 150.00 m/min,
– feed rate f = 0.20 mm/rev,
– cutting width a_p = 2 mm.

The samples for testing the emissivity of the chip upper side were prepared with the following cutting parameters:

– cutting speed v_c = 50.00 m/min,
– feed rate f = 0.04, 0.10, 0.16 mm/rev,
– cutting width a_p = 2 mm.

Results and discussion

Calibration of the measurement chain

During thermovision measurements of temperature distribution in the cutting zone, special attention was paid to the observation of the chip upper surface. Due to the nature of the chip forming process, its upper surface has a complex, fault-crossed texture (Fig. 2). According to the literature data (ARRAZOLA et al. 2008, M'SAOUBI et al. 2004, RECH 2006, WANG et al. 1996), the emissivity of such a surface is significantly different from that given for machined surfaces. Therefore, in order to obtain reliable temperature measurements of the chip upper side it was necessary to calibrate the measuring chain.

Typically, the calibration of thermovision measurement chains is based on a perfectly black body (M'SAOUBI et al. 2004) or specially prepared surfaces with known emissivity (WANG et al. 1996). Jaspers used a different solution in his research (JASPERS et al. 1998). The thermographic measuring chain was calibrated using a chip enclosed in a special vacuum chamber and heated by a current flow. However, these are idealized conditions, far removed from the prevailing conditions during the cutting process. Another equally impor-

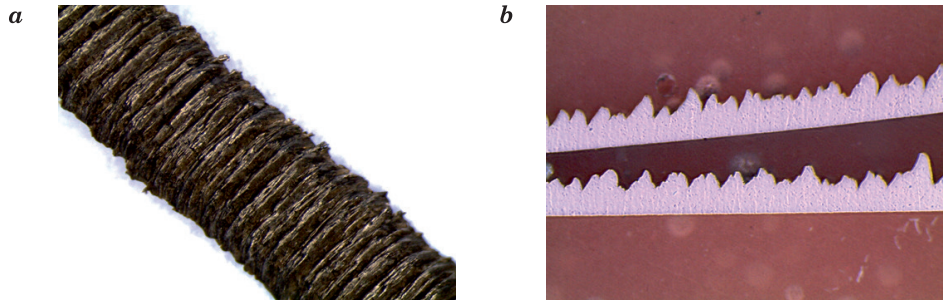

Fig. 2. The chip after orthogonal turning at a cutting speed v_c = 66.67 m/min and feed rate f = 0.1 mm/rev: *a* – view of the chip upper side at magnification ×10.5, *b* – chip longitudinal section at magnification ×24

tant aspect that can affect the accuracy of thermal imaging measurements is the oxidation of the observed surface. However, JASPERS (JASPERS et al. 1998), just like ARRAZOLA et al. (2008) have shown in their works little influence of oxidation on the change of surface emissivity coefficient.

In order to reproduce the conditions as close as possible to real conditions during calibration, the measuring chain was calibrated using chips placed on a plate made of tested steel. To reduce heat conduction losses between the substrate plate and the chip, DRAGON ceramic heat-resistant adhesive was used. As with the experimental tests during calibration, the upper side of the chips was in direct contact with the surrounding atmosphere. An overview of the calibration stand for the thermovision chain is shown in Figure 3.

The course of emission changes of the chip upper surface is shown in Table 3. The average values of chip surface emissivity produced during the experimental tests at a cutting speed v_c = 50 m/min and the values determined for the surface of a steel plate after turning were collected there. The average roughness value of the steel substrate plate was about R_a = 1.215 µm.

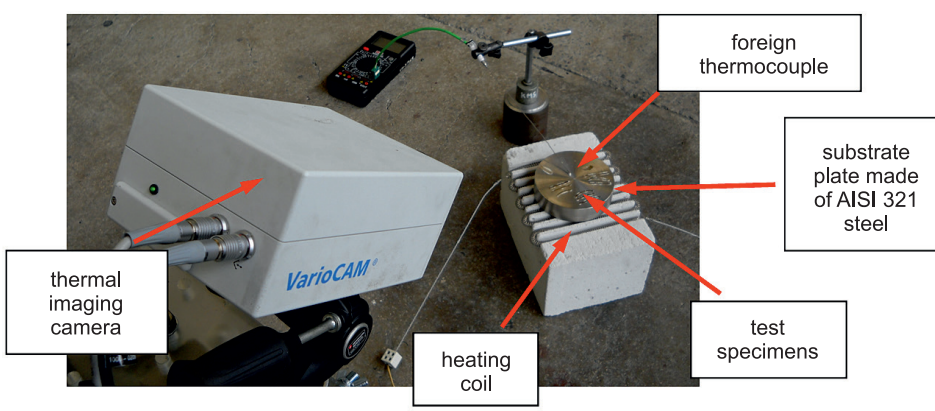

Fig. 3. A calibration stand for the thermal imaging camera

Table 3

A summary of average emissivity values of the chip surface and of AISI 321 steel after turning

Temperature [°C]	Post-turning steel	Chip surface		
		$f = 0.04$	$f = 0.10$	$f = 0.16$
50	0.24	0.50	0.53	0.58
100	0.26	0.55	0.56	0.63
150	0.25	0.54	0.54	0.59
200	0.29	0.60	0.61	0.62
250	0.28	0.59	0.57	0.61
300	0.29	0.60	0.58	0.61
350	0.29	0.63	0.58	0.61
400	0.30	0.60	0.62	0.62
450	0.30	0.58	0.57	0.58
500	0.31	0.53	0.53	0.53
550	0.37	0.49	0.50	0.49
600	0.43	0.45	0.45	0.46

The analysis of the waveform of changes in the value of the emissivity coefficient determined for the upper side of the chips indicates that regardless of the processing parameters, the observed chip surfaces have very similar emissivity values (Fig. 4). The nature of the changes, especially in the higher temperature range is almost identical for all analyzed cases. At the same time, the tests carried out indicate significant differences in the emissivity values for chips and the machined surface of the substrate plate. These differences

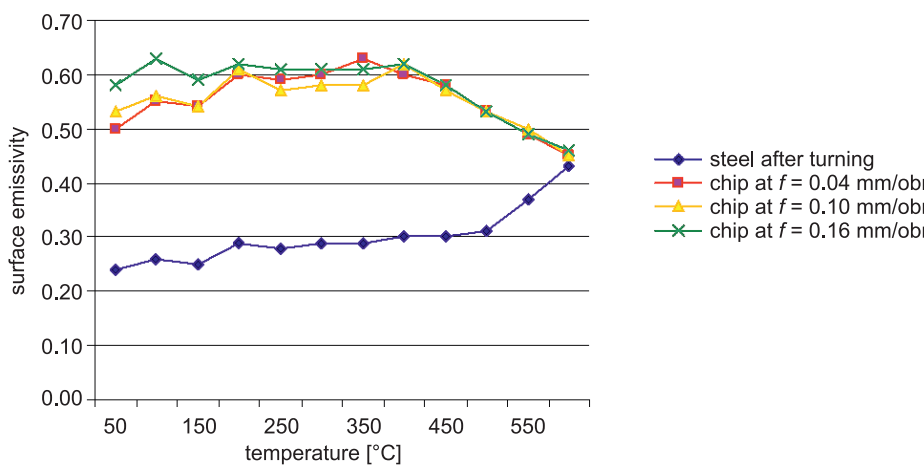

Fig. 4. The course of changes in the emissivity coefficient of the upper side of chips and AISI 321 steel after turning as a function of temperature

are particularly noticeable at temperatures below 400°C. The emissivity for the turned surface in the temperature range under consideration is about half as high as for the upper surface of the chips. Above this temperature, the difference indicated decreases noticeably.

Temperature distribution in the cutting zone

The maximum temperature generated during cutting can reach 900 or even about 1000°C. However, on the surfaces of the cutting zone we can observe much lower values. The greatest amount of heat generated in the cutting zone is carried away with the chip. Therefore, in the thermographic image of the cutting zone its surface has the brightest colors. A sample image obtained from a thermal imaging camera is shown in Figure 5. Its analysis shows that the temperature distribution along the center line of the chip is in line with the literature (JASPERS et al. 1998, RECH 2006). The waveform of the temperature changes of the upper side of the chip are shown in Figure 6. The IRBIS 3 software used in the tests allowed to automatically search for the area with the highest temperature and set the maximum temperature value. Using this function, the temperature values of the maximum chip upper side were determined for all the cases studied. An exemplary summary of the thermal imaging results and the corresponding average contact temperature values is shown in Table 4 and Figure 7.

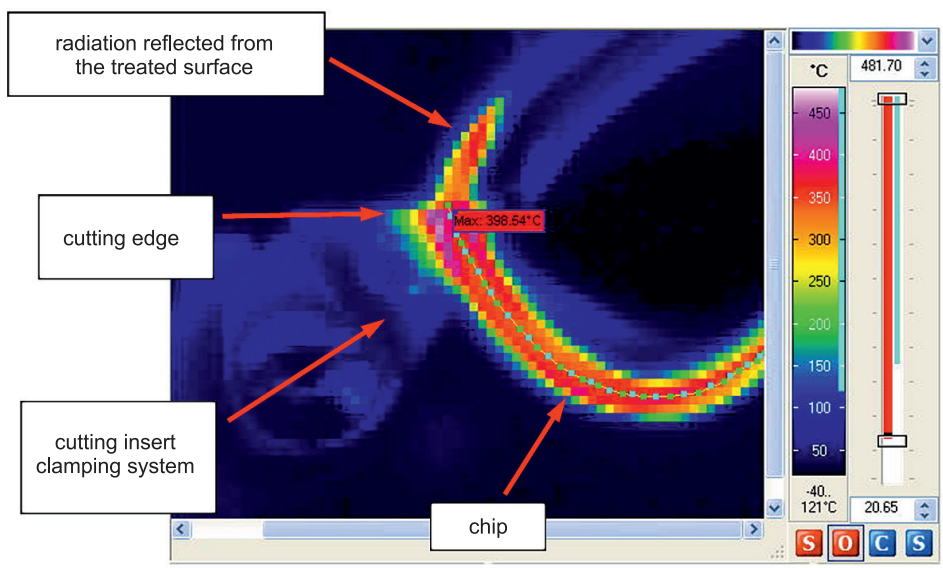

Fig. 5. A thermographic image of the cutting zone obtained for a cutting insert without coatings at a cutting speed v_c= 100 m/min and feed rate f = 0.20 mm/rev

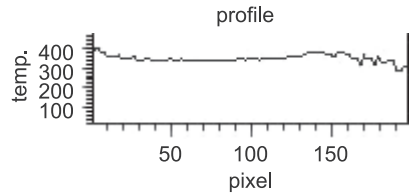

Fig. 6. The temperature distribution along the chip center line, cutting parameters: v_c = 100 m/min, f = 0.20 mm/rev

Table 4

Examples of average values of test results for a feed rate of 0.2 mm/rev and a variable cutting speed

v_c [m/min]	t_k [°C]	$t_{W\max}$ [°C]
66.67	880.0	367.3
86.33	912.4	376.5
100.00	931.0	381.8
116.67	949.4	387.3
133.33	963.1	392.1
150.00	972.0	396.3

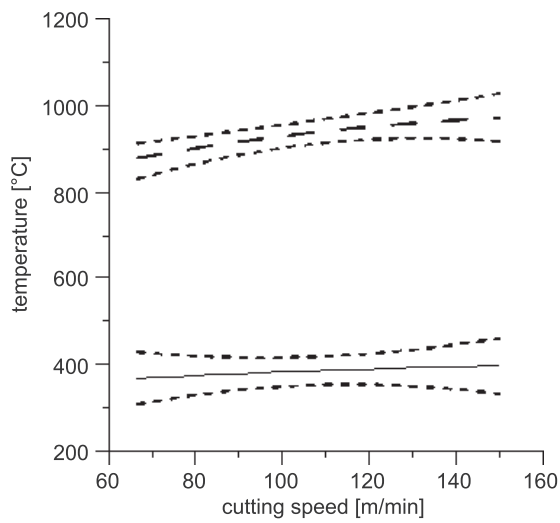

Fig. 7. Contact temperature and maximum temperature of the chip upper side; cutting parameters: v_c= 100 m/min, f = 0.20 mm/rev

When comparing the results obtained with each other, it can be seen that the temperature value of the maximum chip upper side is proportional to the average contact temperature. At cutting speed of 66.67 m/min it represents approximately 42-44% of the average contact temperature and approximately 40-42% w_k for v_c = 150 m/min. The results obtained indicate that the value of the maximum temperature of the chip upper side mainly depends on the cutting speed v_c. The feed rate does not affect the nature of changes in relation $t_{W\max}=f(t_k)$.

Interferences

Detailed analysis of the thermographic images of the cutting zone indicates that the measurement result may be affected by a number of external factors. In the previously discussed Figure 5, outside the clearly visible chip area, one can see the radiation reflected from the processed surface of the object. The cause of such an interference is considered to be the angle of the thermal imaging camera and the proximity of the heat source. The angle at which the IR camera was set during the measurements caused the collected images to show the IR radiation emitted from the chip just behind the slip zone, which was reflected on the surface of the processed test specimen. Sometimes the source of reflected radiation can be lighting or solar radiation. However, it should be noted that these interferences do not cause significant changes in the temperature distribution on the upper surface of the chip. In practice, only sporadically occurring point reflections of foreign IR radiation could be observed on the upper surface of the chip without affecting the measurement value. The negligible impact of these interferences is supposed to be due to the high roughness and irregular shape of the observed chip surface.

The literature quite often says that the reason for inaccuracies in thermal imaging measurements may be the oxidation of the observed surfaces. However, due to its relatively small importance it is usually overlooked (ARRAZOLA et al. 2008, JASPERS et al. 1998). The phenomenon of surface oxidation is closely related to the change of its emissivity coefficient. Therefore, when analyzing the nature of the changes in the surface emissivity coefficient, determined in the tests, as a function of temperature, it can be seen that the assumption made on the basis of literature data about the negligible effect of surface oxidation on the emissivity coefficient is appropriate, but only up to a temperature of about 400°C (Figure 4). When this value is exceeded, the emissivity of the chip upper surface decreases noticeably, reaching about 0.453 at 600°C. The opposite phenomenon is observed for the substrate plate. When it exceeds 450°C, its emissivity coefficient gradually increases to a value of about 0.430 at 600°C. Such changes in the emissivity coefficient values for both observed surfaces, which differ significantly in roughness, suggest that for a higher temperature range, however, the oxidation phenomenon is significant. It should be noted that the method used in the research to determine the emissivity coefficient

of the upper side of the chip contained the effect of the oxidation of the observed surface, therefore additional actions to correct its value were not necessary.

The second most significant and frequent disturbing factor is the chips curling above the cutting edge. A sample image of the cutting zone with a visible chip that interferes with the measurement is shown in Figure 8. As we know, the chips may temporarily obscure the measurement site completely, making it impossible to determine the temperature in the area under study. In addition, the heat lifted along with the chip has a strong influence on the surfaces directly adjacent to it by reflecting on them and changing the temperature indication values. Due to its nature, this type of interference is difficult to control.

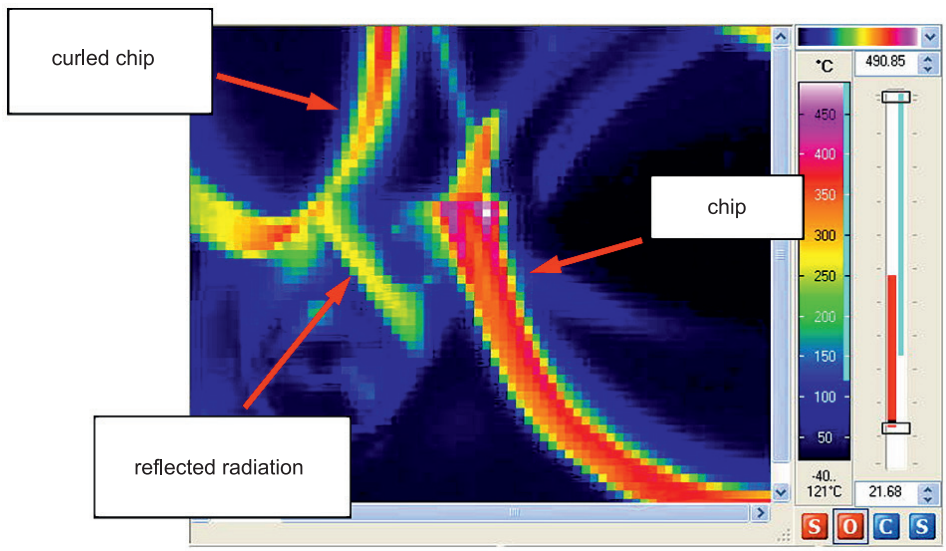

Fig. 8. The temperature distribution along the chip center line, cutting parameters: v_c = 100 m/min, f = 0.20 mm/rev

Conclusions

On the basis of the conducted research, it can be concluded that thermal imaging measurements of the temperature distribution in the cutting zone enable the determination of the maximum temperature of the chip upper side. However, the accuracy of such measurements depends on the precision of the calibration of the measuring chain. The value of the temperature determined in this way is proportional to the temperature generated with the contact area between the chips and the rake face. In the case of the examined austenitic steel, the ratio of the temperature of the chip upper side $t_{W\max}$ to the contact temperature t_k in the entire examined range of cutting speeds is almost constant and varies from

40 to 44%. It should be noted, however, that for other machined materials this ratio may take different values. The literature analysis and my own research indicate that the maximum temperature of the chip upper side can be successfully used to verify numerical calculations of the heat distribution in the cutting zone.

References

ABHANG L.B., HAMEEDULLAH M. 2010. *Chip-Tool Interface Temperature Prediction Model for Turning Process*. International Journal of Engineering Science and Technology, 2(4): 382-393.

AKHIL C.S., ANANTHAVISHNU M.H., AKHIL C.K., AFEEZ P.M., AKHILESH R., RAHUL R. 2016. *Measurement of Cutting Temperature during Machining*. IOSR Journal of Mechanical and Civil Engineering, 13(2-I): 108-122.

ANEIRO F.M., COEHO R.T., BRANDÃO L.C. 2008. *Turning Hardened Steel Using Coated Carbide at High Cutting Speeds*. Journal of the Brazilian Society of Mechanical Sciences and Engineering, XXX(2): 104-109.

ARRAZOLA P.J., ARRIOLA I., DAVIES M.A., COOKE A.L., DUTTERER B.S. 2008. *The effect of machinability on thermal fields in or-thogonal cutting of AISI 4140 steel*. CIRP Annals – Manufacturing Technology, 57: 65-68.

BASTI A., OBIKAWA T., SHINOZUKA J. 2007. *Tools with built-in thin film thermocouple sensors for monitoring cutting temperature*. International Journal of Machine Tools & Manufacture, 47: 793-798.

CEAU G., POPOVICI V., CROITORU S. 2010. *Researches About The Temperature of The Cutting Edge in Turning of Unalloyed Steel*. U.P.B. Sci. Bull., Series D, 72(3): 97-110. GRZESIK W. 2016. *Advanced Machining Processes of Metallic Materials. Theory, Modeling and Applications*. Elsevier Science.

HEIGEL J.C., WHITENTON E., LANE B., DONMEZ M.A., MADHAVAN V., MOSCOSO-KINGSLEY W. 2017. *Infrared measurement of the temperature at the tool–chip interface while machining Ti–6Al–4V*. Journal of Materials Processing Technology, 243: 123-130.

JASPERS S.P.F.C., DAUTZENBERG J.H., TAMINIAU D.A. 1998. *Temperature Measurement in Orthogonal Metal Cutting*. The International Journal of Advanced Manufacturing Technology, 14: 7-12.

M'SAOUBI R., CHANDRASEKARAN H. 2004. *Investigation of the effects of tool micro-geometry and coating on tool temperature during orthogonal turning of quenched and tempered steel*. International Journal of Machine Tools & Manufacture, 44: 213-224.

Narzędzia tokarskie. 2017. Katalog firmy Sandvik Coromant.

RECH J. 2006. *Influence of cutting tool coatings on the tribological phe-nomena at the tool-chip interface in orthogonal dry turning*. Surface & Coatings Technology, 200: 5132-5139.

STEPHENSON D.A., AGAPIOU J.S. 2016. *Metal Cutting Theory and Practice*. Third Edition, CRC Press.

WANG L., SAITO K., JAWAHIR S.I. 1996. *Infrared temperature meausrement of curled chip formation in metal machining*. Transaction of NAMRI/SME, XXIV: 87-92.

YVONNET J., UMBRELLO D., CHINESTA F., MICARI F. 2006. *A simple inverse procedure to determine heat flux on the tool in orthogonal cutting*. International Journal of Machine Tools & Manufacture, 46: 820-827.

ZHAO J., LIU Z., WANG B., HUA Y., WANG Q. 2018. *Cutting temperature measurement using an improved two-color infrared thermometer in turning Inconel 718 with whisker-reinforced ceramic tools*. Ceramics International, 44(15): 19002-19007.

Technical Sciences, 2020, 23(1), 81–89

UNIWERSYTET WARMIŃSKO-MAZURSKI W OLSZTYNIE

Quarterly peer-reviewed scientific journal
ISSN 1505-4675
e-ISSN 2083-4527
TECHNICAL SCIENCES
Homepage: www.uwm.edu.pl/techsci/

doi: 10.31648/ts.5422

THE INFLUENCE OF ELECTRONIC EXPOSURE AND HEAT TREATMENT ON THE ELECTRICAL CONDUCTIVITY OF EPOXY POLYMER MATERIALS

***Yuliia Udovytska*[1], *Sergiy Luniov*[2], *Vitalii Kashytskyi*[3], *Volodymyr Maslyuk*[4], *Ivan Megela*[5]**

[1]ORCID: 0000-0003-4707-6363
Science and Research Department
Lutsk National Technical University
[2]ORCID: 0000-0003-0737-8703
Department of Basic Sciences
Lutsk National Technical University
[3]ORCID: 0000-0003-2346-912X
Materials Science Department
Lutsk National Technical University
[4]ORCID: 0000-0002-5933-8394
Department of Photonuclear Processes
Institute of Electronic Physics, NAS
[5]ORCID: 0000-0003-3388-3535
Department of Photonuclear Processes
Institute of Electronic Physics, NAS

Received 22 April 2020, accepted 30 May 2020, available online 2 June 2020.

K e y w o r d s: irradiation, epoxy resin, specific electrical conductivity, heat treatment.

A b s t r a c t

The effects of high energy (12 MeV) electron irradiation and heat treatment on the electrical properties of epoxy polymers with PEPA content of 11, 12, and 13 wt. h. per 100 wt., including epoxy resin, were investigated. It was found that the electrical conductivity of epoxy polymers increases with electron irradiation, especially for doses higher than 10 kGy. It was also demonstrated that extra

Correspondence: Yuliia Udovytska, Lutsk National Technical University, Lvivska Str., 75, Lutsk, 43018, Ukraine, e-mail: yulgb123@gmail.com.

heat treatment of irradiated samples with a hardener content of 12 wt. h. leads to a further increase in their electrical conductivity. The nature of the obtained dependencies of electrical conductivity is determined by the processes of cross-linking and irradiation/thermal destruction, as well as the mass fraction content of the hardener. The radiation-stimulated increase in the conductivity of epoxy polymers can be used in the manufacture of conductive protective coatings and electronic components of sensors.

Introduction

The tasks of getting new and expanding the scope of composite materials by modifying structure and stability have always been pressing problems of science and technology (Clough 2011, Akhmedov et al. 2013, Pinchuk et al. 2009, Verma et al. 2020, 2019a, 2019b). In this sense, it is promising to use polymer composite materials based on epoxy resins, which have high adhesion to many materials and unique physical and mechanical properties that explain their wide range of applications in aerospace, engineering, and other fields of technology (Abakarov et al. 2007). In particular, conductive composites are widely used to produce conductive coatings, thermal and radiation screens, grounding conductors, and the development of many electronics and microsensors (Ishkov, Sagalkov 2006, Petrov, Gagulin 2001, Gaskov, Rumiantceva 2000, Galiamov et al. 2000, Zou et al. 2010, Bai, Shi 2007). The most common way to create electrically conductive composite materials based on polymer dielectrics is to introduce a variety of electrically conductive fillers (Blait, Blur 2008).

Also, as the review of modern works (Verma et al. 2017, 2018a, 2018b, 2019c) shows, promising structural materials are materials whose structure is a combination of bio and epoxy composites. The study of the conductive properties of such systems is just beginning. On the other hand, the results of the development of electrically conductive composite materials must meet some of the special requirements, such as manufacturability, economy, the efficiency of operational properties.

Most of the materials developed in such a way do not meet these requirements at the same time. For example, soot-filled polymer composites become conductive in soot content, which is much larger than with the introduction of carbon nanotubes, which, in turn, is difficult to distribute uniformly in the polymer matrix (Kuryptya et al. 2016).

For solving this problem, one requires finding new methods and technologies. In this respect, the processing of polymer composite materials by external physical fields (radiation, temperature, magnetic, electrical) will allow purposefully changing the electrical properties of these materials. In (Akhmedov et al. 2013, Pinchuk et al. 2009, Fouracre et al. 1991, Demkiv et al. 2015, Nychyporenko

et al. 2016, SHESHIN, DENISOVA 2016), ionizing radiation's influence on the physicochemical properties of polymer composite materials were investigated. It has been shown that the treatment of polymer composites by X-ray, gamma, or beta-radiation beams improves mechanical, electrical, and photoelectric properties. In (SAVCHUK et al. 2008, STUKHLIAK, KARTASHOV 2011), optimal temperature-time modes of heat treatment and low-frequency alternating magnetic field treatment were established, which provided an increase in the mechanical characteristics of epoxy composites. But, the combined effect of different physical fields on the physical, including electrical and chemical properties of epoxy polymers, has not yet been studied.

Thus, an urgent applied task is to study the effect of high-energy electron irradiation and heat treatment on the electrical properties of epoxy-based polymeric materials.

Experimental technique

This study's objective was to investigate the effect of different doses of high energy (12 MeV) electron irradiation on the specific conductivity of ED-20 brand epoxy resin with polyethylene polyamine hardener (11, 12 and 13 parts by weight per). According to theoretical estimates of (KNYAZEV 1977), the optimal content of PEPA hardener in the resin ED-20 is from 5 to 15 parts by weight per. As shown in (SAVCHUK et al. 2008, 2014), a decrease or increase of the proportion of hardener weakens the mechanical, tribotechnical and operational properties in varying degrees. For example, epoxy resin hardens unevenly and the physical and mechanical properties of the absolutely identical samples obtained on its basis will differ, when the content of a hardener PEPA more than 15 wt. h. Such material is not suitable for serial use. The most homogeneous structure and the best physical and mechanical properties are achieved when the content of the PEPA hardener in the neighborhood of 12 wt. h. This argued our choice of such mass fractions of PEPA hardener. The composition was poured into special shapes, resulting in rectangular parallelepiped specimens, 6×10×14 mm in size (see Fig. 1).

The initial curing process went on 24 hours under normal conditions (the air temperature in the laboratory was 20°C, atmospheric pressure – 750 mm Hg, and relative humidity – from 40 to 50 percent). The samples of the first group were irradiated with different electron dozes. The samples of the second group after irradiation were further heat treated. The heat treatment was a stepwise drying process in a furnace at temperatures of 70… 130°C for 6 hours (heat treatment at 70°C took place during the first hour, at 80°C, 90°C, 100°C, 110°C, 130°C – during the second, third, fourth, fifth and sixth hours, respectively). Radiation experiments were performed on the microtron M30 of IEP NASU

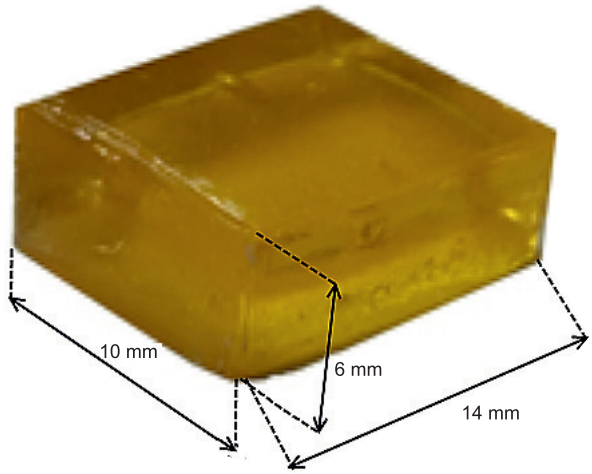

Fig. 1. The photograph of a epoxy resin sample for studies of the specific conductivity

with the electron's energy of 12 MeV, and they are monoenergetic of 0.01%. The inhomogeneity of the irradiation field did not exceed 10%. To ensure the stability of the room temperature of irradiation, which was recorded by a copper-constant differential thermocouple, the test samples were blown with nitrogen vapor. The epoxy polymer samples were irradiated to doses from 5 kGy (total fluence 1.56×10^{13} el./cm^2) to 100 kGy (total fluence 3.12×10^{14} el./cm^2) at electron flux rate 8.7×10^{10} el./(cm^2·s). The electron energy was chosen for the reason in order to the average linear electron path in the epoxy polymer was larger than the linear dimensions of the investigated samples. As is known (PAVLENKO et al. 2015, YASTREBINSKI et al. 2016), this parameter for the electron energy of 10 MeV is 1-4 cm for polymers, depending on their structure. In this case, the defects creation will be relatively uniform in the volume of a composite and there will be no significant resistance gradients that affect on the electrical conductivity of the epoxy resin. The processes of radiation destruction and creating of microcracks (PAVLENKO et al. 2010) will become significant at doses greater than 100 kGy. This will be affect the reducing of various physical and mechanical properties of the investigated epoxy polymer, including electrical properties. Measurements of the electrical resistance of epoxypolymers were performed on a universal voltmeter-electrometer B7-30, which allows measurements of the resistance of materials in the range from 10^5 Om to 10^{18} Om. If the cross-sectional area of the sample is epoxy polymer S, and the length is L, then its specific conductivity:

$$\sigma = \frac{L}{RS} \tag{1}$$

R – is the resistance of the epoxypolymer [Om].

Experimental results and discussion

In Figures 2–4 presents the dependences of the electrical conductivity of the epoxypolymer with different content of PEPA hardener on the irradiation doses of 12 MeV electrons. As one can see, the specific conductivity of epoxypolymers (both in the absence and in the presence of extra heat treatment after irradiation) decreases with increasing radiation dose to 10 kGy and then rapidly increases. Irradiation of samples of epoxypolymers with a hardener content of 12 wt. h. with a dose of 100 kGy, their special heat treatment increases the electrical conductivity by 1.7 times (Fig. 2, curve *1*). For samples of epoxy-dianic resin with a hardener content of 11 and 13 wt. h. the most significant effect of increasing the electrical conductivity of 1.2 times (for samples of epoxy-dianic resin with a hardener content of 11 parts by weight) and 3.9 times (for samples of epoxy-dianic resin with the content of hardener 13 parts by weight) is achieved after irradiation of these samples with a dose of 100 kGy, without extra heat treatment (Fig. 2 and Fig. 3, curve *1*). According to Figure 2 and Figure 3, the extra heat treatment of these samples after irradiation leads to a decrease in their electrical conductivity.

The two different processes occur in the irradiated polymers composites. The first one consists (AKHMEDOV et al. 2013, BLAIT, BLUR 2008) in the cross-linking of their chain structures under irradiation. In this case, it takes place the enlarging of the polymer macromolecules due to the formation of transverse chemical bonds between linear macromolecules. Another process is the destruction of macromolecules, the creation of the smaller macromolecules with some volatile products. The intensities and characters of the cross-linking and destruction processes of epoxypolymers depend on conditions of radiation treatments, especially on their doses and values of energy of the electrons.

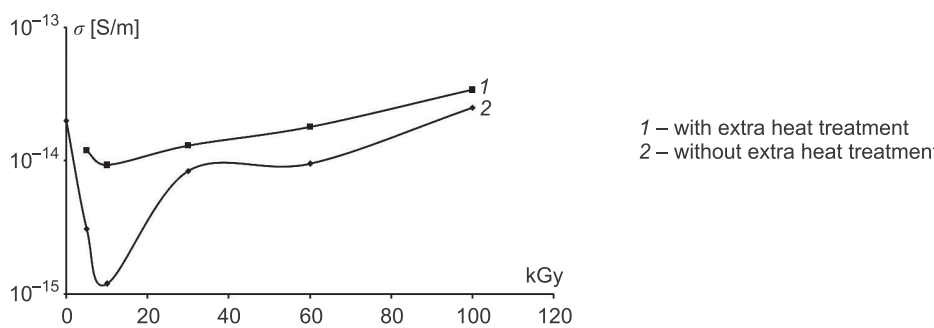

Fig. 2. The dependencies of the specific electrical conductivity on the absorbed electron irradiation doses for epoxypolymers with the content of PEPA hardener 12 parts by weight:
1 – irradiated samples of epoxypolymer which had been extra heat-treated,
2 – the same irradiated samples without extra heat treatment

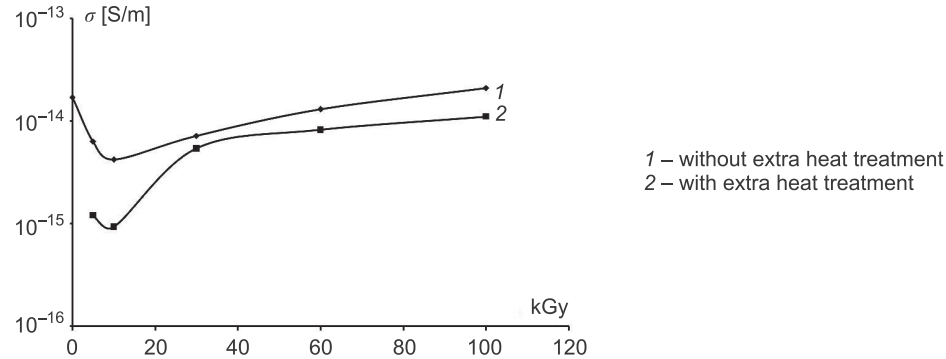

Fig. 3. The dependencies of the specific conductivity on the absorbed electron irradiation doses for epoxypolymers with the content of PEPA hardener 11 parts by weight:
1 – irradiated samples of epoxypolymer without extra heat treatment,
2 – same irradiated samples which had been extra heat-treated

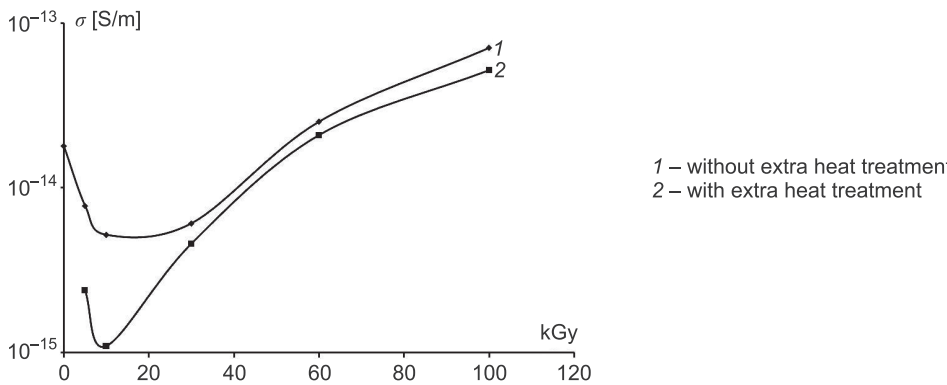

Fig. 4. The dependence of the specific conductivity on the absorbed electron irradiation doses for epoxypolymers with the content of PEPA hardener 13 parts by weight:
1 – irradiated samples of epoxypolymer without extra heat treatment,
2 – same irradiated samples which had been extra heat-treated

The effectiveness of such mechanisms of radiation-chemical transformations in composite materials will depend on the additional heat treatment and the mass fraction of the hardener, which explains the dependencies obtained in Figures 1-3. According to (ABAKAROV et al. 2007, BLAIT, BLUR 2008), three mechanisms of electrical conductivity are possible in polymer dielectrics: ionic, polarizing, and electronic. Besides, the dissociation and ionization of polymer molecules and processes of recombination of current carriers must also be taken into account. Today there is no only theory that able to explain the electrical conductivity of polymeric materials. For most polymer dielectrics, ionic conductivity is inherent (BLAIT, BLUR 2008). The specific conductivity

of the polymer is determined by the presence of free ions that are not chemically bonded to the macromolecules. In this case, the polymer chain is not involved in the transfer of electric charges, and the magnitude of the conductivity of the polymer depends on the presence of low molecular weight impurities, which can be a source of ions (AKHMEDOV et al. 2013). The expression for ionic conductivity can be written as (BLAIT, BLUR 2008):

$$\sigma = q\left(\sum_{i=1}^{n} m_i n_i \mu_i + \sum_{j=1}^{k} m_j n_j \mu_j\right) \tag{2}$$

where:

q – is the electron charge modulus,
m_i – is the charge of the i-th positive ion in electron charge units,
n_i – is their concentration,
μ_i – is the mobility,
m_j, n_j, μ_j – are the corresponding values for the j-th negative ion.

Cross-linking polymer macromolecules lead to the formation of a spatial grid and, consequently, a decrease in ion mobility. The decreasing of the ion mobility, according to equation 2, cause the reduction of the specific electrical conductivity of the polymer. Thus, for samples of epoxy-dianic resin with different PEPA harden content with electron irradiation doses up to 10 kGy, the probability of cross-linking is higher than that destruction of macromolecules, which explains the decrease of the electrical conductivity (see Figs. 2-4). For irradiation doses greater than 10 kGy, the destruction becomes more efficient.

Conclusions

The results of studies of the electrical properties of the electron-irradiated epoxy-dianic resin demonstrate their complicated nature. The specific electrical conductivity of these materials is determined by the domination of the macromolecules' cross-linking or destruction mechanisms, as well as the mass fraction of the curing agent into an epoxy-dianic resin.

The aggregation of macromolecules of the epoxypolymer due to their cross-linking leads to decreasing electrical conductivity. Extra heat treatment is effective only for irradiated epoxy resin samples with a hardener content of 12 wt. h. and leads to an increase in their electrical conductivity. Heat treatment of irradiated epoxy resin samples with a hardener content of 11 and 13 wt. h. leads to a decrease in their electrical conductivity. A purposeful change in the mass fraction of the hardener and the electron irradiation dose will control the electrical properties of the epoxy composite materials, which can be used to create conductive protective coatings and sensor electronics based on them.

References

Abakarov S.A., Magomedov G.M., Magomedov M.Z.R. 2007. *Electrical conductivity of epoxy polymers filled with SiO_2 nanoparticles*. Dagestan State Pedagogical University Journal Natural and Exact Sciences, 1: 11-15.

Akhmedov F.I., Kuliev A.D., Akhverdiev R.B., Samedova A.S., Guseinova M.B. 2013. *The effect of gamma radiation on the electrical conductivity of polymeric polypropylene composites with aluminum and iron oxides*. Electronic Materials Processing, 6: 94-97.

Bai H., Shi G. 2007. *Gas sensors based on conducting polymers*. Sensor, 7(3): 267-307.

Blait E.R., Blur D. 2008. *Electrical properties of polymers*. Fizmatlit, Moscow, p. 373.

Clough R.L. 2001. *High-energy radiation and polymers: A review of commercial processes and emerging applications*. Nuclear Instruments and Methods in Physics Research Section B: Beam Interactions with Materials and Atoms, 185(1-4): 8-33.

Demkiv T.M., Haliatkin O.O., Khapko Z.A. 2015. *Influence of ionizing radiation on the electrical properties of composite polymeric materials with BaF_2 and SrF_2 nanoparticles*. Visnyk of Lviv National University, The Series is Physical, 50: 64-71.

Fouracre R.A., Banford H.M., Tedford D.J., Gedeon S., Cao X., Wu S., Fu L. 1991. *The effect of gamma-irradiation on the electrical properties of two typical epoxy resin systems*. International Journal of Radiation Applications and Instrumentation. Part C. Radiation Physics and Chemistry, 37(4): 581-588.

Galiamov B.Sh., Zavialov S.A., Kupriianov L.Iu. 2000. *Features of the microstructure and sensory properties of nanosized composite films*. Journal of Physical Chemistry, 74(3): 459-465.

Gaskov A.M., Rumiantceva M.N. 2000. *Selection of materials for solid state gas sensors*. Inorganic Materials, 36(3): 369-378.

Ishkov A.V., Sagalakov A.M. 2006. *Electric conductivity of composites containing nonstoichiometric titanium compounds*. Technical Physics Letters, 32(5): 377-378.

Knyazev V.K. 1977. *Epoxy construction materials in mechanical engineering*. Mechanical Engineering, Moscow, p. 183.

Kuryptya Y., Sova N., Savchenko B., Slieptsov A., Plavan V. 2016. *Design of electrically conducting polymer hybrid composites based on polyvinyl chloride and polyethylene*. Eastern-European Journal of Enterprise Technologies, 3, 6(81): 26–32.

Nychyporenko O.S., Dmytrenko O.P., Kylish M.P., Pyinchuk-Rugal T.M., Grabovskij Yu.Je., Zabolotnij M.A., Mamunya Je.P., Levchenko V.V., Shlapats'ka V.V., Strel'chuk V.V., Tkach V.M. 2016. *Radiation-stimulated alteration of electrical conductivity of polyethylene nanocomposites with carbon nanotubes*. Problems of Atomic Science and Technology, 2(102): 99-106.

Pavlenko V.I., Bondarenko G.G., Cherkashina N.I. 2015. *Calculation of ionization and radiation losses of fast electrons in polystyrene composite*. Perspektivnye Materialy, 8: 5-11.

Pavlenko V.I., Yastrebinskij R.N., Edamenko O.D., Tarasov D.G. 2010. *Affecting of high-power bunches of rapid electrons polymeric radiation-protective composites*. Problems of Atomic Science and Technology, 1(65): 129-134.

Petrov V.M., Gagulin V.V. 2001. *Radar Absorbing Materials*. Inorganic Materials, 37(2): 135-141.

Pinchuk T.N., Didenko T.P., Dmitrenko O.P., Kulish N.P., Prilutsky Yu.P., Grabovsky Yu.Ye., Sementsov Yu.I., Shlapatskaya V.V. 2009. *Radiation modification of the physicomechanical properties of isotactic polypropylene with multi-walled carbon nanotubes*. Problems of Atomic Science and Technology, 4: 275-278.

Savchuk P.P., Kostornov A.G., Kashitskii V.P., Sadova O.L. 2014. *Friction wear of modified epoxy composites*. Powder Metallurgy and Metal Ceramics, 53(3-4): 205-209.

Savchuk P.P., Kostornov A.H., Kashytskyi V.P. 2008. *Influence of technological parameters on properties of epoxy composite materials*. Bulletin of Vasyl Stefanyk Precarpathian National University, Chemistry Series, VI: 56-64.

SHESHIN E.P., DENISOVA L.V. 2016. *Radiation modification of composite materials under gamma irradiation*. Bulletin of BSTU named after V.G. Shukhov, 12: 170-173.

STUKHLIAK P.D., KARTASHOV V.V. 2011. *Physico-mechanical properties of epoxy composites treated with low-frequency alternating magnetic fields*. Oil and Gas Exploration and Development, 2: 49-53.

VERMA A., SINGH V.K. 2019. *Mechanical, microstructural and thermal characterization of epoxy-based human hair-reinforced composites*. Journal of Testing and Evaluation, 47(2): 1193-1215.

VERMA A., BAURAI K., SANJAY M.R., SIENGCHIN S. 2020. *Mechanical, microstructural, and thermal characterization insights of pyrolyzed carbon black from waste tires reinforced epoxy nanocomposites for coating application*. Polymer Composites, 41(1): 338-349.

VERMA A., BUDIYAL L., SANJAY M.R., SIENGCHIN S. 2019. *Processing and characterization analysis of pyrolyzed oil rubber (from waste tires) – epoxy polymer blend composite for lightweight structures and coatings applications*. Polymer Engineering & Science, 59(10): 2041-2051.

VERMA A., GAUR A., SINGH V.K. 2017. *Mechanical properties and microstructure of starch and sisal fiber biocomposite modified with epoxy resin*. Materials Performance and Characterization, 6(1): 500-520.

VERMA A., JOSHI K., GAUR A., SINGH V.K. 2018. *Starch-jute fiber hybrid biocomposite modified with an epoxy resin coating: fabrication and experimental characterization*. Journal of the Mechanical Behavior of Materials, 27(5-6).

VERMA A., NEGI P., SINGH V.K. 2018. *Physical and Thermal Characterization of Chicken Feather Fiber Reformed Epoxy Resin Hybrid Composite*. Advances in Civil Engineering Materials, 7(1): 538-557.

VERMA A., NEGI P., SINGH V.K. 2019. *Experimental analysis on carbon residuum transformed epoxy resin: Chicken feather fiber hybrid composite*. Polymer Composites, 40(7): 2690-2699.

YASTREBINSKI R.N., CHERKASHINA N.I., YASTREBINSKAYA A.V., NOSKOV A.V. 2016. *Energy losses of fast electrons when passing through the radiation-protective iron-oxide composite*. Problems of Atomic Science and Technology, 4(104): 9-14.

ZOU J., Yip H.-L., HAU S.K., JEN A.K.-Y. 2010. *Metal grid/conducting polymer hybrid transparent electrode for inverted polymer solar cells*. Applied Physics Letters, 96(20): 203-301.

Technical Sciences, 2020, 23(1), 91–104

UNIWERSYTET WARMIŃSKO-MAZURSKI W OLSZTYNIE

Quarterly peer-reviewed scientific journal
ISSN 1505-4675
e-ISSN 2083-4527
TECHNICAL SCIENCES
Homepage: www.uwm.edu.pl/techsci/

doi: 10.31648/ts.5376

FORMATION AND RUPTURE OF GAS FILM OF ANTIBUBBLE

***Lichun Bai*[1], *Jinguang Sun*[2], *Zhijie Zeng*[3], *Yuhang Ma*[4], *Lixin Bai*[5]**

[1] ORCID: 0000-0003-4100-8546
School of Electronic and Information Engineering
Liaoning Technical University, Huludao, China
[2] ORCID: 0000-0001-7690-8486
School of Electronic and Information Engineering
Liaoning Technical University, Huludao, China
[3] ORCID: 0000-0003-0902-5741
University of Chinese Academy of Sciences
State Key Laboratory of Acoustics, Institute of Acoustics
Chinese Academy of Sciences, Beijing, China
[4] ORCID: 0000-0002-4700-0636
University of Chinese Academy of Sciences
State Key Laboratory of Acoustics, Institute of Acoustics
Chinese Academy of Sciences, Beijing, China
[5] ORCID: 0000-0003-0950-315X
State Key Laboratory of Acoustics, Institute of Acoustics
Chinese Academy of Sciences, Beijing, China

Received 1 April 2020, accepted 29 May 2020, available online 4 June 2020.

K e y w o r d s: Antibubble, gas film, liquid film, High-speed photographystructure.

A b s t r a c t

The formation and rupture of gas film in the process of formation, rupture and coalescence of antibubbles were investigated by high-speed photography. It was found that a gas film will appear and wrap a droplet when the droplet hit a layer of liquid film or foam before impacting the gas-liquid interface. The gas film may survive the impact on the gas-liquid interface and act as the gas film of an antibubble. A multilayer droplet will be formed when the droplet hits through several

Correspondence: L. Bai, State Key Laboratory of Acoustics, Institute of Acoustics, Chinese Academy of Sciences, No.21, Bei-Si-huan-Xi Road, Beijing, China (100190), Phone: +86-10-82547758, e-mail: blx@mail.ioa.ac.cn

layer of liquid films, and a multilayer antibubble will be formed when the multilayer droplet impact a gas-liquid interface or a single layer of foam on the liquid surface. The way to generate antibubbles by liquid films will undergo the formation and rupture of gas films. The coalescence of two antibubbles, which shows a similar merging process of soap bubbles, also undergo the rupture and formation of gas films. The rupture of gas film of antibubble caused by aging and impact is also discussed.

Introduction

Antibubbles are unusual fluid objects in the liquid. An antibubble is a thin spherical gas film containing and being surrounded by a liquid, which is completely opposite to the soap bubble structure. Antibubbles, with the special structure, have many potential applications. Antibubble can be used for air filtration or cleaning because of its large gas-liquid surface area without significant volume increase. Anti-bubble can hold specific liquids for substance transport or drug preparation, etc. Although antibubble has been reported as early as 1932 (HUGHES et al. 1932) and has been formally named as antibubble in 1974 (STONG 1974), antibubble is still an area that we know little about. Few researches were conducted until this century some valuable researches on formation (GANAN-CALVO et al. 2001, TUFAILE et al. 2002, POSTEMA et al. 2005, KIM et al. 2008, POSTEMA et al. 2007), aging (DORBOLO et al. 2005, 2010, SCHEID et al. 2012, 2014), collapse (SOB'YANIN 2015, ZOU et al. 2013), stabilization (DORBOLO et al. 2003, KIM et al. 2006, POORTINGA 2011), optical properties (SUHR 2012) and control (SILPE et al. 2013, POORTINGA 2013) of antibubbles aroused great academic interest.

The formation of antibubble is the premise and an important aspect of antibubble research. Antibubbles are usually generated by impinging a droplet or liquid jet on a stationary liquid surface (SOB'YANIN 2015), forming a gas film between the droplet or liquid jet and the liquid surface. Under the action of gravity and impact force, the gas film wraps the liquid and sinks below the liquid surface. The jet breaks because of Rayleigh-Plateau instability, the gas film closes, and becomes spherical under the action of surface tension, thus forming a gas film.

This method of producing antibubbles requires that the liquid surface is very clean, even so, the survival rate of antibubbles is still very low. Preparing antibubbles requires great patience (as shown in Fig. 1). For this reason, some researchers have made some improvements to this method, such as vibrating the nozzle and creating an oscillation in the incident jet (BREWER et al. 2010), adding an electrical connection to prevent electrical potential difference due to triboelectric effects (DORBOLO et al. 2003), and rationalizing several aspects of the optimal window in parameter space for creating antibubbles (KIM et al. 2008).

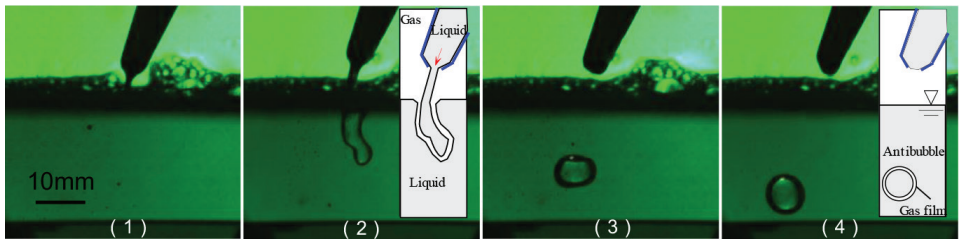

Fig. 1. Schematic diagram of experimental setup

Other researchers developed totally different methods to generate antibubbles, such as generating micron-sized antibubbles by capillary flow focusing (GANAN-CALVO et al. 2001), or generating millimeter-sized antibubbles by the coalescence between two bubbles (TUFAILE et al. 2002), or producing antibubbles by first making a particle-stabilized water-in-oil-in-water emulsion, then freeze-drying to remove both the water and the oil, and finally reconstitute the resulting powder in water (POORTINGA 2013), or oscillating contrast agent microbubbles may create a surface instability, and the re-entrant jet protrude into the gas bubble, leaving a droplet inside the bubble (POSTEMA et al. 2005, POSTEMA et al. 2007). In this paper, the membrane structure (liquid film and gas film) and its dynamic behavior in the process of antibubble formation and rupture is studied by means of high-speed photography.

Experiment

The experimental device consists of a glass tank, a dripping device, liquid films, a foam layer, a light source, lenses and a high-speed camera (as shown in Fig. 2). The dripping device can produce jets of different velocities and droplets

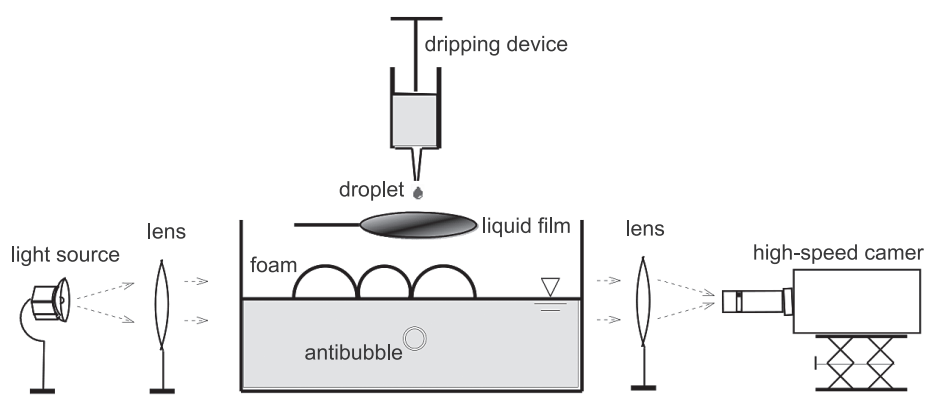

Fig. 2. Schematic diagram of experimental setup

of different sizes. A rectangular plexiglass container (220 mm×150 mm×170 mm) is used to hold a mixture of tap water and linear alkylbenzenesulfonate (LAS) (about 10 times the critical micellar concentration (2.2 mM)). The behavior of cavitation bubbles and antibubbles is recorded with a high-speed camera (Photron Fastcam SA-1, Photron Ltd., Japan) equipped with two long distance microscopes (Zoom 6000, Navitar, USA; LM50JCM, Kowa, Japan) respectively. The frames are illuminated with PI-LUMINOR high-light LED lamp (150 W), Cree XHP70 white high power LED, HALOGEN lamp (2600 W). In order to get a better image exposure, two lenses are used to produce parallel light for illumination in some experiments. In the experiment, the liquid in the dropper is the same as that in the rectangular glass tank. The gas in the antibubble film is the air in the environment (temperature: 20°C, pressure: 1 atm).

Results and discussion

Formation of antibubble

The preparation of antibubbles in laboratory requires harsh conditions. The dust and foam on the liquid surface affect the formation of antibubbles. It is usually necessary to use overflow devices to obtain a clean gas-liquid interface (as shown in Fig. 3). However, our experiments have found that the presence of foams on the interface sometimes helps to form antibubbles. When a single layer of foam (larger than the droplet size) is spread over the interface, the droplets or jet first penetrates the foam and then enters the water to become antibubbles (as shown in Fig. 3*b*).

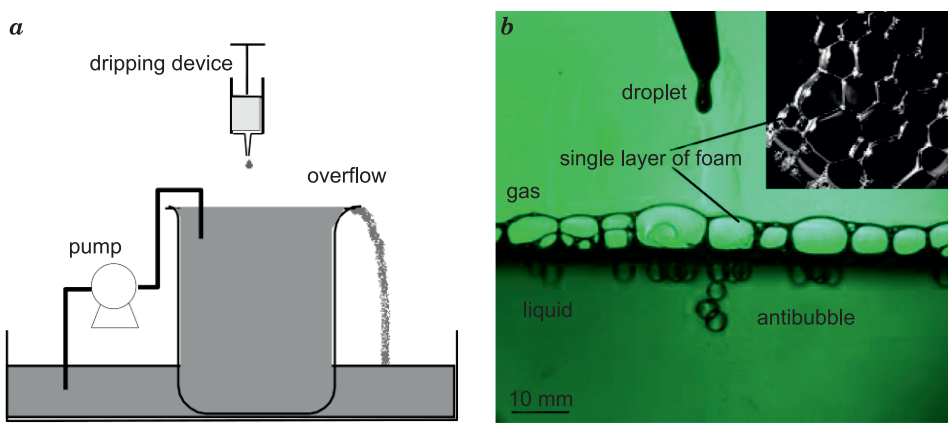

Fig. 3. Liquid surface conditions capable of producing antibubbles:
a – overflow, *b* – single layer of foam

The total reflection caused by the gas-liquid interface on both sides of the gas film makes the antibubble shine in the reflected light and show a thick black edge on the outer edge in the transmission light. This is the most obvious difference between ordinary bubbles and antibubbles underwater (as shown in Fig. 4*a*, *b*). When the droplet drops into a honeycomb monolayer foam on the liquid surface, if the impact point is near the intersection line of three soap bubbles (plateau boundary) or near the interface of two soap bubbles (common liquid membrane),

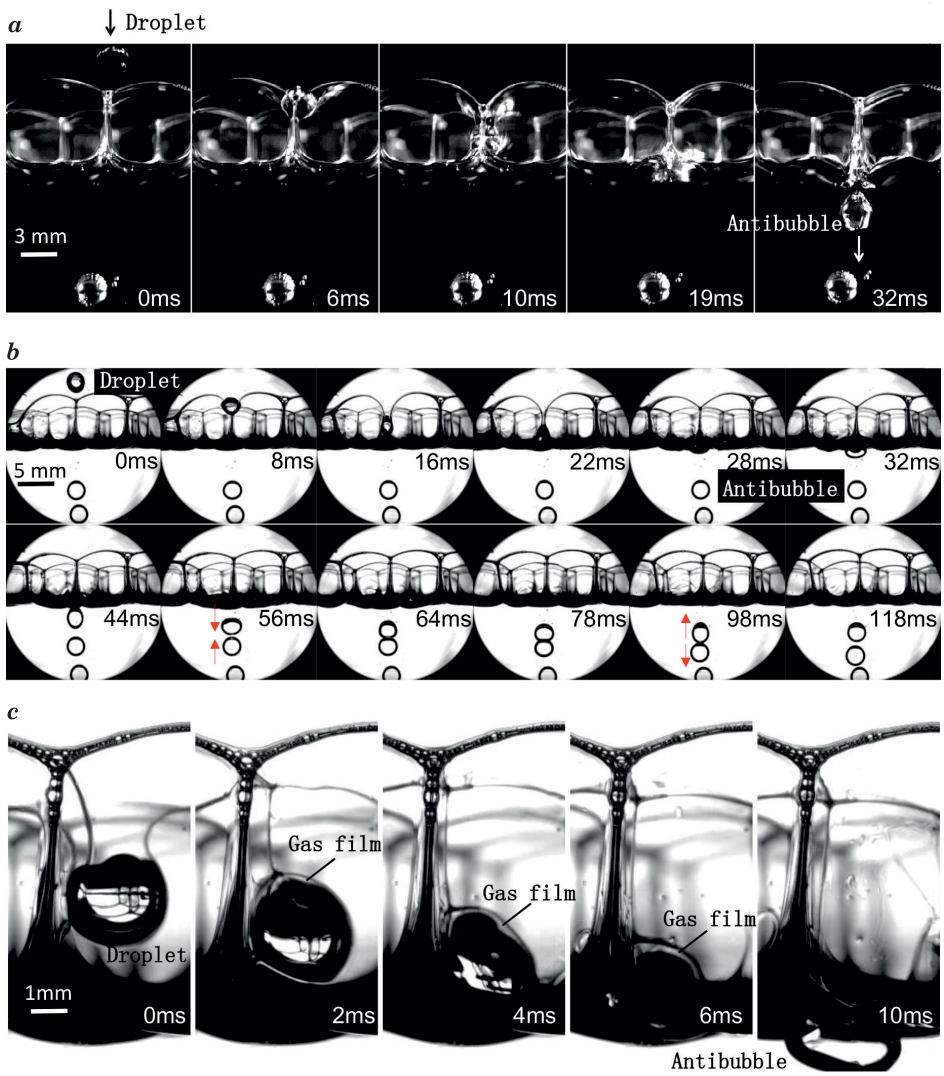

Fig. 4. Antibubble formation by hitting through a foam layer:
a – reflected light, *b* – transmitted light, *c* – detailed layout

because of the Gibbs-Marangoni effect, the surfactant molecules on the liquid film surface have the ability of self-repair to resist external disturbance, and the liquid film will deform without breaking. Because the hydrophobic end of surfactant in the liquid film of soap bubbles and interface of falling droplets is point towards the gas side, the plateau boundary or common liquid film of soap bubbles is separated by droplets, and there is a layer of gas film between the droplets and the liquid film (as shown in Fig. 4*c*). When the droplets with a layer of gas film and a layer of liquid film fall to the liquid surface, the liquid film and the liquid in the container are united, while the gas film still exists. Under the action of gravity and inertia, the droplets with gas film sink into the water and become antibubbles. The deformability of the foam layer causes the droplet to form a gas film before strongly impacting the liquid surface, which is the key to increase the production rate of the antibubbles. It is found in the experiment that when droplets impact near the dome ($\overset{\downarrow}{\frown}$) of the soap bubble, droplets will pass through the liquid film of the soap bubble, and then fall into the water. No antibubbles can be formed. However, if we reverse the bending direction of the liquid film ($\underset{\downarrow}{\smile}$), in most cases, an antibubble will be formed (as shown in Fig. 5).

In the experiment, a metal frame is used to support the liquid film. Because of gravity, the arc surface of the liquid film is concave. When the droplet passed through the liquid film, the droplet was wrapped by the liquid film, and there was a layer of gas film between the liquid film and the droplet (as shown in Fig. 5*a*). Reflected light was used to illuminate the surface of droplets. It can be clearly seen that the pressure wave caused by the lifting of the liquid film causes the fluctuation of the upper part of the droplet. A depression is formed at the top of the droplet and a micro bubble is wrapped into the droplet. This phenomenon is very common in the experiments of droplet penetrating the liquid film. If the droplet penetrates through two layers of liquid film, the droplet will be wrapped by two layers of liquid film and two layers of gas film (as shown in Fig. 5*b*). If the droplet penetrates through three layers of liquid film, three layers of liquid film and three layers of gas film will be wrapped outside the droplet (as shown in Fig. 5*c*).

It can be seen from Figure 6 that when the droplet impacts the liquid film, the liquid film is gradually stretched as the droplet falls. The surface tension of the liquid film tends to minimize the surface energy, which causes the liquid film to shrink toward the center and form a saddle shape. With the acceleration of contraction, the liquid film in the neck finally contacts each other and produces a liquid jet in the upper and lower directions of the neck. The liquid film in the metal frame and the liquid film encapsulating the droplets are closed separately. The liquid column between the two liquid films splits into micro droplets under the action of surface tension.

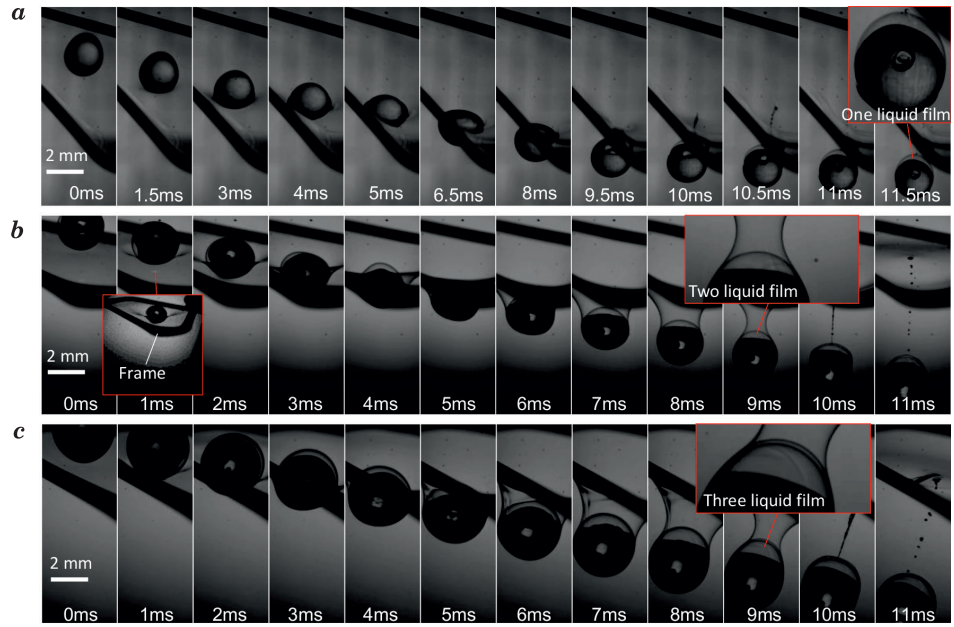

Fig. 5. Antibubble formation by hitting through a liquid film:
a – single layer liquid film, reflected light, *b* – double layer liquid film, transmitted light,
c – three layer liquid film, transmitted light

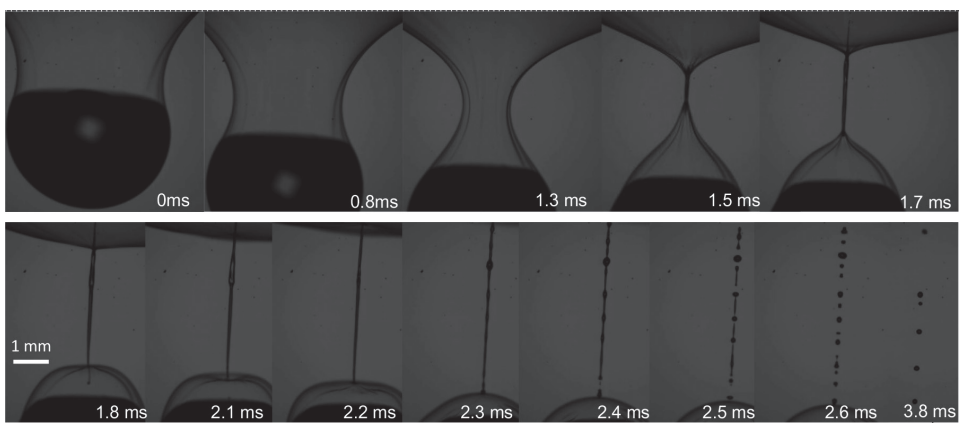

Fig. 6. The process of droplet packing by liquid film

Under the action of surfactants, ordinary droplets or droplets coated with one or more layers of liquid film and gas film usually form a layer of gas film between the outermost layer of the droplet and the liquid surface (as shown in Fig. 7*b* and *c*). The above-mentioned gas film holds the droplet floating on the liquid surface, forming a floating droplet or multilayer floating droplet. However,

under the pressure of gravity and lifting force, the gas in the film will drain rapidly, and the film will become thinner until it breaks due to van der Waals force. After the film breaks down, the liquid film on the outermost layer of the droplet merges with the liquid in the container. Mechanically unstable droplets will undergo a series of deformation until the next stable state. For multi-layer floating droplets (as shown in Fig. 7*a*, liquid film and gas film can be clearly seen), when the gas film breaks down, the droplets gradually narrow in the horizontal direction, making the droplets nearly conical. Subsequently, as the droplet width increases gradually, the top of the droplet begins to drop rapidly, and a surface wave extending outward is formed on the surrounding liquid surface. As the droplet sinks, it can be clearly seen that the circular intersection line between the top of the droplet and the liquid surface gradually reduces to a point and disappears , while releasing surface waves to propagate outward (as shown in Fig. 7*a*, *b*). For ordinary floating droplets (as shown in Fig. 7*c*), when the film breaks down, the droplet diameter decreases horizontally and forms a vertical boundary while the height remains unchanged. The boundary gradually shrinks towards the droplet axis, and at the same time, obvious surface waves are formed on the droplet surface. Subsequently, the droplets evolved from a cylindrical shape to a conical shape, and then, while the upper diameter of the cone remained unchanged, the bottom contracted rapidly to form a small diameter cylinder, which then sank into the water. During the whole deformation process of the droplet, surface waves continue to release and expand to the surrounding liquid surface (as shown in Fig. 7*c*).

The multi-layer floating droplets will sink into the water to form antibubbles after the breakdown of the gas film, while the ordinary floating droplets

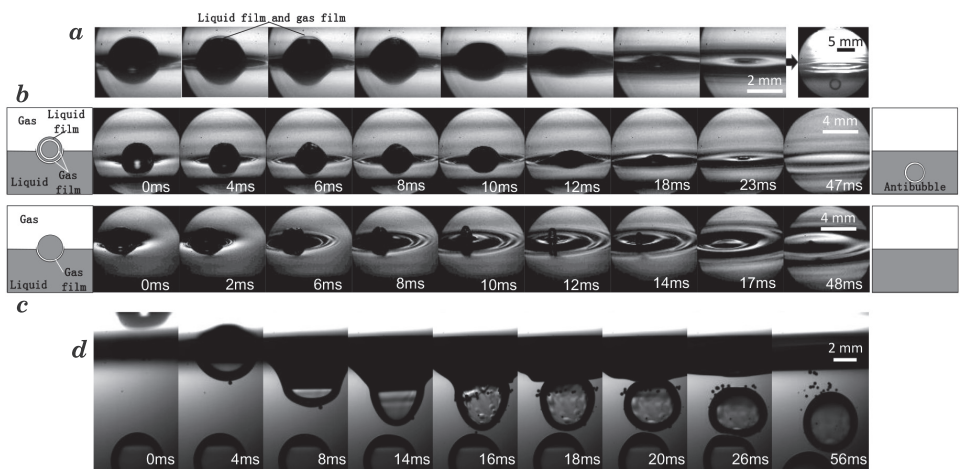

Fig. 7. The collapse of gas film and the formation of antibubble (*a*) and (*b*) multilayer floating droplet (on the surface) (*c*) ordinary floating droplet (*d*) multilayer floating droplet (under the surface)

will merge with the surrounding liquid after the breakdown of the gas film. The process of gas film breakdown and anti-bubble formation under liquid surface was photographed by high-speed photography under transmission light (as shown in Fig. 7*d*). When multi-film droplets fall on the liquid surface, there are thick black edges in the outer ring of the droplet and the area intersecting with the liquid surface due to the existence of gas film and the total reflection of light caused by it (as shown in Fig. 7*d*, τ = 8 ms). When the gas film breaks down (as shown in Fig. 7*d*, τ = 16 ms), the light transmitted from the droplet center appears very mottled due to the disturbance of the fluid and the change of the inner film thickness caused by the disturbance. At this moment, the black edge around the droplet still exists, indicating that the droplet is still encapsulated by the gas film. As the droplet sinks under the action of gravity and inertia force, an antibubble can be clearly observed below the liquid surface (as shown in Fig. 7*d*, τ = 56 ms).

The phenomenon of droplets bouncing on the liquid surface sometimes occurs when the gas film of ordinary floating droplets breaks down (as shown in Fig. 8). Every time the droplet bounces, it will become smaller. This is because when the gas film breaks down and the floating droplet deforms to the stage of thin cylinder, the lower part continues to shrink until it breaks, making the upper liquid form an independent smaller droplet. The smaller droplet falls to the surface again under the action of gravity, forming a new floating droplet. This newly formed floating droplet can undergo the same process to form another smaller droplet that falls onto the surface of the liquid. In this way, droplets can bounce up to four or five times on the surface of the liquid. The energy of these deformations comes from the surface energy released by film breakdown and droplet reduction.

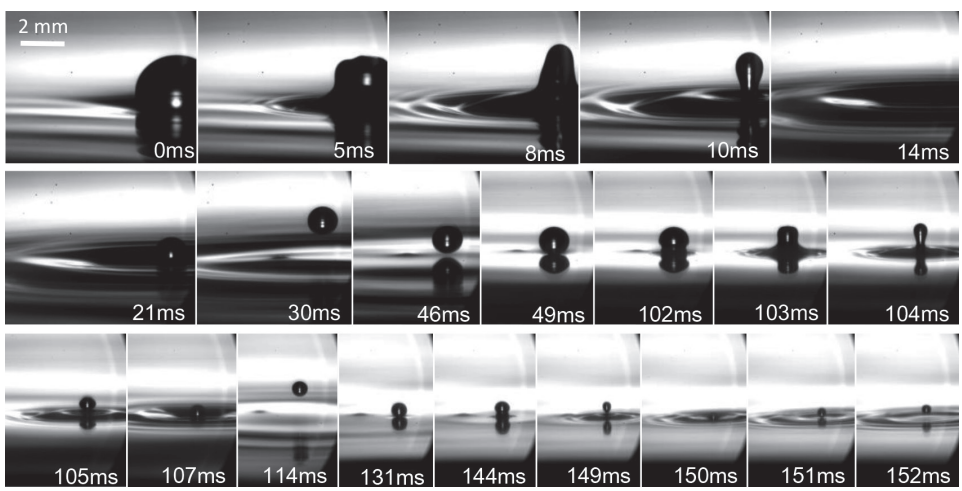

Fig. 8. Bouncing droplets on the liquid surface

Rupture of antibubble

Figure 4*a*, *b*, *c* and Figure 7*a*, *b*, *d* show the formation process of antibubbles. When droplets pass through several layers of liquid film and then fall on the liquid surface or fall on a single layer of foam, multi-layer antibubbles enveloped by several layers of gas film and several layers of liquid film may form under water. Because the gas density is smaller than that of water, the gas in the lower part of the anti-bubble film will gather up to the upper part, so the lower part of the film is very thin and the upper part is very thick. When the droplets are wrapped by several gas films, the black edges in the outer ring of the anti-bubble is much thicker at the top than at the bottom (as shown in Fig. 9). When one gas film breaks down in a multi-layer antibubble (whether inner or outer), the number of gas film layers decreases, but it does not lead to the disappearance of the whole antibubble (as shown in Fig. 10). The inner gas film of a multi-layer antibubble bursts at $\tau = 4$ ms. Many bubbles formed by gas film breakdown float up in the spherical droplets and coalesce at the top of the liquid inside the antibubble.

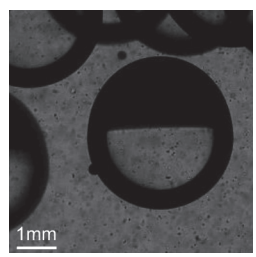

Fig. 9. Multilayer antibubbles

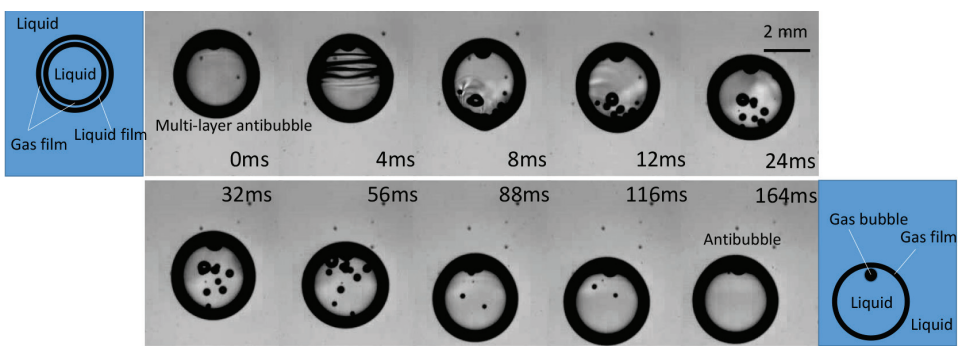

Fig. 10. The collapse of gas film of a multilayer antibubble

In order to explore the details of antibubble rupture, a single-gas-film antibubble breakdown process was photographed by a high-speed camera in a framing rate of 4000 fps and an exposure time of 1/178 000 s (as shown in Fig. 11). Because of the buoyancy of a small amount of gas in the antibubble gas film, the antibubble attached to the liquid surface (there is a layer of gas film between the antibubble and the liquid surface) slightly lifts the liquid surface to form a bump (τ = 0 ms). When the antibubble film breaks down at the lower right, the rest of the film remains intact, so the black edge caused by total reflection still exists. Due to total reflection, we cannot see the starting point of film breakage, but the surface wave generated by the breakdown has been formed and propagates to the upper left (τ = 0.50 ms). When the film disappears by one third, the black edge caused by total reflection in the lower right part disappears, and the outer edge of the damaged film and the small bubbles formed by fragmentation can be clearly seen (τ = 1.25 ms). After the antibubble collapses, a gas bubble is formed at the intersection with the liquid surface and attached below the liquid surface (τ = 4.75 ms).

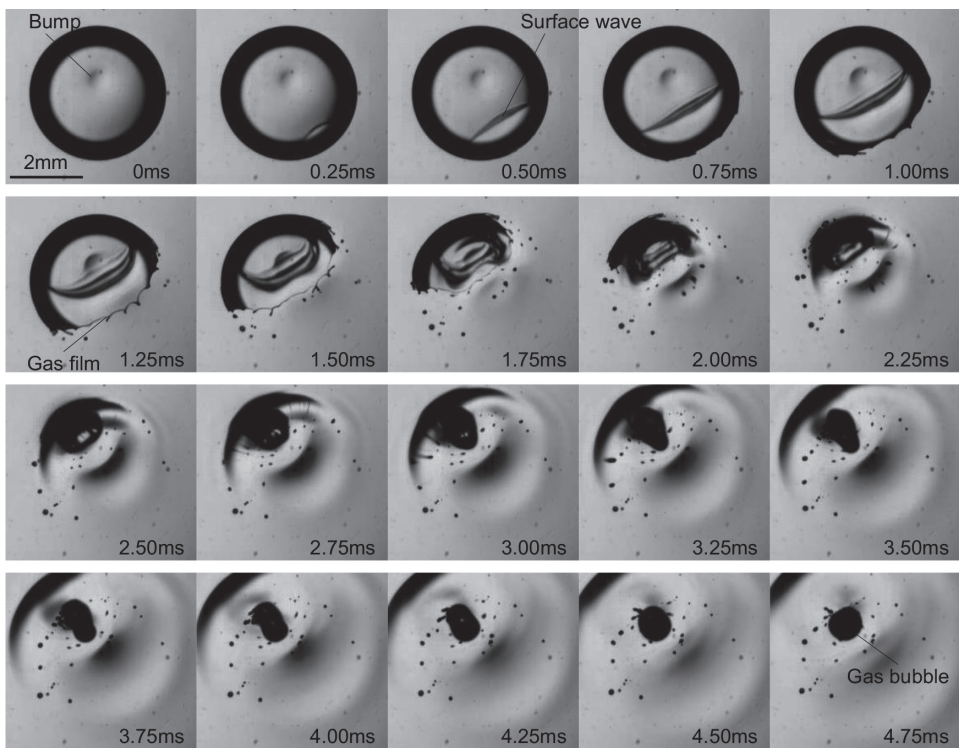

Fig. 11. The collapse of an antibubble

Coalescence of antibubbles

Due to the action of surfactants, two antibubbles usually bounce off when they collide with each other (Fig. 4*b*, τ = 56 ms – 118 ms; Fig. 7*d*, τ = 18 ms – 56 ms). However, if the film breaks when two antibubbles collide, the two antibubbles may merge with each other (as shown in Fig. 12). It is well known that there are two gas-liquid surfaces in the gas film of an antibubble. When two antibubbles collide, if the outer gas-liquid surface of the two gas films ruptures and merges, the two antibubbles will share an outer gas-liquid surface while retaining the original inner gas-liquid surface, forming an "8" shape structure. In this state, a shared gas film is formed between two droplets. If the shared gas film breaks down, in other words, the inner gas-liquid surface merges, then two droplets wrapped in the gas film merge, and two antibubbles merge into an antibubble. The coalescence of two antibubbles shows a similar merging process of soap bubbles. The present work is, to the best of the authors' knowledge, the first analysis about the coalescence of antibubbles.

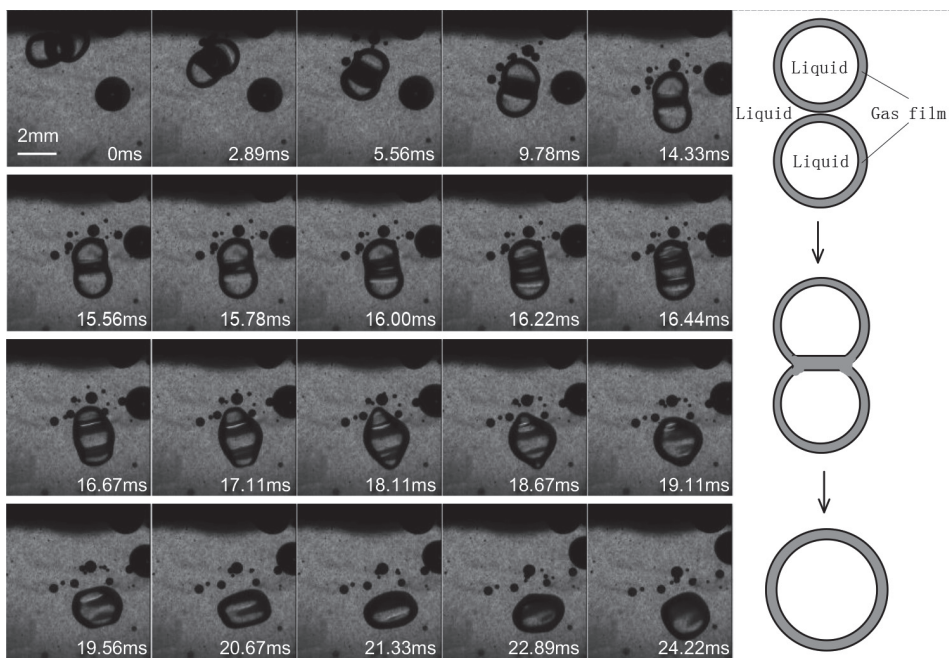

Fig. 12. The coalescence of antibubbles

Conclusion

The formation, rupture and coalescence of antibubbles are experimentally investigated by high-speed photography. The research focuses on the interaction between antibubble and film (gas film and liquid film) in these physical processes. It is found that if droplets or jets interacts with a liquid film or liquid membrane structure (foam) before impinging on the liquid surface, a gas film structure coated with liquid film will be formed. Then the impact on the liquid surface will greatly increase the survival rate of the antibubbles. This fluid structure encapsulated by gas film and liquid film impinges on the liquid surface, which will greatly improve the survival rate of antibubble. When droplets pass through several layers of liquid film and then fall on the liquid surface or fall on a single layer of foam, multi-layer antibubbles enveloped by several layers of gas film and several layers of liquid film may form under water. Because of the potential energy of the membrane structure, the rupture of films will produce new fluid structures. When two antibubbles interact, the rupture and coalescence of gas films can be decomposed into the process of the rupture and coalescence of two gas-liquid surfaces and different fluid structures can be formed.

Acknowledgments

This work was supported by the National Key Research and Development Project (No. 2018YFB1403303), the National Natural Science Foundation of China (No. 11874062, No. 11674350).

References

Brewer N., Nevins T., Lockhart T. 2010. *The formation of antibubbles*. The 4th place poster at the 2010 UW-Eau Claire Research Day.

Dorbolo S., Caps H., Vandewalle N. 2003. *Fluid instabilities in the birth and death of antibubbles.* New Journal of Physics, 5: 161.1–161.9.

Dorbolo S., Reyssat E., Vandewalle N., Qu´Er´E D. 2005. *Aging of an antibubble.* Europhysics Letters, 69: 966–970.

Dorbolo S., Terwagne D., Delhalle R., Dujardin J., Huet N., Vandewalle N., Denkov N. 2010. *Antibubble lifetime: influence of the bulk viscosity and of the surface modulus of the mixture.* Colloids and Surfaces A, 365: 43–45.

Ganan-Calvo M., Gordillo J.M. 2001. *Perfectly monodisperse microbubbling by capillary flow focusing.* Physical Review Letters, 87: 274501.

Hughes W., Hughes A.R. 1932. *Liquid drops on the same liquid surface.* Nature, 129: 59–59.

Kim P G., Stone A.H. 2008. *Dynamics of the formation of antibubbles.* Europhysics Letters, 83: 54001.

Kim P G., Vogel J. 2006. *Antibubbles: Factors that affect their stability.* Colloids and Surfaces A, 289: 237–244.

POORTINGA A.T. 2011. *Long-lived antibubbles: stable antibubbles through Pickering stabilization*. Langmuir, 27: 2138–2141.

POORTINGA A.T. 2013. *Micron-sized antibubbles with tunable stability.* Colloids and Surfaces A, 419: 15–20.

POSTEMA M., DE JONG N., SCHMITZ G., VAN.WAMEL A. 2005. *Creating antibubbles with ultrasound*. Proceedings IEEE Ultrasonics Symposium, p. 977–980.

POSTEMA M., TEN CATE F. J., SCHMITZ G., DE JONG N., VAN WAMEL A. 2007. *Generation of a droplet inside a microbubble with the aid of an ultrasound contrast agent: first result*. Letters in Drug Design & Discovery, 4: 74–77.

SCHEID B., DORBOLO S., ARRIAGA L. R., RIO E. 2012. *The drainage of an air film with viscous interfaces.* Physical Review Letters, 109: 264502.

SCHEID B., ZAWALA J., DORBOLO S. 2014. *Gas dissolution in antibubble dynamics*. Soft Matter, 10: 7096–7102.

SILPE J. E., MCGRAIL D.W. 2013. *Magnetic antibubbles: Formation and control of magnetic macroemulsions for fluid transport applications.* Journal of Applied Physics, 113: 17B304.

SOB'YANIN D.N. 2015. *Theory of the antibubble collapse.* Physical Review Letters, 114: 104501.

STONG C.L. 1974. *Curious bubbles in which a gas encloses a liquid instead of the other way around.* Scientific American Magazine, 230: 116–120.

SUHR W. 2012. *Gaining insight into antibubbles via frustrated total internal reflection*. European Journal of Physics, 33: 443–454.

TUFAILE A., SARTORELLI J. C. 2002. *Bubble and spherical air shell formation dynamics*. Physical Review E, 66: 056204.

ZOU J., JI C., YUAN B. G., RUAN X. D., FU X. 2013. *Collapse of an antibubble.* Physical Review E, 87: 061002(R).

Guide for Autors

Introduction

Technical Sciences is a peer-reviewed research Journal published in English by thePublishing House of the University of Warmia and Mazury in Olsztyn (Poland). Journal is published continually since 1998. Until 2010 Journal was published as a yearbook, in 2011 and 2012 it was published semiyearly. From 2013, the Journal is published quarterly in the spring, summer, fall, and winter.

The Journal covers basic and applied researches in the field of engineering and the physical sciences that represent advances in understanding or modeling of the performance of technical and/or biological systems. The Journal covers most branches of engineering science including biosystems engineering, civil engineering, environmental engineering, food engineering, geodesy and cartography, information technology, mechanical engineering, materials science, production engineering etc.

Papers may report the results of experiments, theoretical analyses, design of machines and mechanization systems, processes or processing methods, new materials, new measurements methods or new ideas in information technology.

The submitted manuscripts should have clear science content in methodology, results and discussion. Appropriate scientific and statistically sound experimental designs must be included in methodology and statistics must be employed in analyzing data to discuss the impact of test variables. Moreover there should be clear evidence provided on how the given results advance the area of engineering science. Mere confirmation of existing published data is not acceptable. Manuscripts should present results of completed works.

There are three types of papers: a) research papers (full length articles); b) short communications; c) review papers.

The Journal is published in the printed and electronic version. The electronic version is published on the website ahead of printed version of Technical Sciences.

Technical Sciences does not charge submission or page fees.

Types of paper

The following articles are accepted for publication:

Reviews

Reviews should present a focused aspect on a topic of current interest in the area of biosystems engineering, civil engineering, environmental engineering, food engineering, geodesy and cartography, information technology, mechanical engineering, materials science, production engineering etc. They should include all major findings and bring together reports from a number of sources. These critical reviews should draw out comparisons and conflicts between work, and provide an overview of the 'state of the art'. They should give objective assessments of the topic by citing relevant published work, and not merely present the opinions of individual authors or summarize only work carried out by the authors or by those with whom the authors agree. Undue speculations should also be avoided. Reviews generally should not exceed 6,000 words.

Research Papers

Research Papers are reports of complete, scientifically sound, original research which contributes new knowledge to its field. Papers should not exceed 5,000 words, including figures and tables.

Short Communications

Short Communications are research papers constituting a concise description of a limited investigation. They should be completely documented, both by reference list, and description of the experimental procedures. Short Communications should not occupy more than 2,000 words, including figures and tables.

Letters to the Editor

Letters to the Editor should concern with issues raised by articles recently published in scientific journals or by recent developments in the engineering area.

Contact details for submission

The paper should be sent to the Editorial Office, as a Microsoft Word file, by e-mail: techsci@uwm.edu.pl

Referees

Author/authors should suggest, the names, addresses and e-mail addresses of at least three potential referees. The editor retains the sole right to decide whether or not the suggested reviewers are used.

Submission declaration

After final acceptance of the manuscript, the corresponding author should send to the Editorial Office the author's declaration. Submission of an article implies that the work has not been published previously (except in the form of an abstract or as part of a published lecture or academic thesis or as an electronic preprint), that it is not under consideration for publication elsewhere, that publication is approved by all authors and tacitly or explicitly by the responsible authorities where the work was carried out, and that, if accepted, it will not be published elsewhere in the same form, in English or in any other language.

To prevent cases of ghostwriting and guest authorship, the author/authors of manuscripts is/are obliged to: (i) disclose the input of each author to the text (specifying their affiliations and contributions, i.e. who is the author of the concept, assumptions, methods, protocol, etc. used during the preparation of the text); (ii) disclose information about the funding sources for the article, the contribution of research institutions, associations and other entities.

Language

Authors should prepare the full manuscript i.e. title, abstract and the main text in English (American or British usage is accepted). Polish version of the manuscript is not required.

The file type

Text should be prepared in a word processor and saved in doc or docx file (MS Office).

Article structure

Suggested structure of the manuscript is as follows:

Title
Authors and affiliations
Corresponding author
Abstract
Keywords
Introduction
Material and Methods
Results and Discussion
Conclusions

Acknowledgements (optional)
References
Tables
Figures

Subdivision – numbered sections

Text should be organized into clearly defined and numbered sections and subsections (optionally). Sections and subsections should be numbered as 1. 2. 3. then 1.1 1.2 1.3 (then 1.1.1, 1.1.2, …). The abstract should not be included in numbering section. A brief heading may be given to any subsection. Each heading should appear on its own separate line. A single line should separate paragraphs. Indentation should be used in each paragraph.

Font guidelines are as follows:

– Title: 14 pt. Times New Roman, bold, centered, with caps
– Author names and affiliations:12 pt. Times New Roman, bold, centered, italic, two blank line above
– Abstract: 10 pt. Times New Roman, full justified, one and a half space. Abstract should begin with the word Abstract immediately following the title block with one blank line in between. The word Abstract: 10 pt. Times New Roman, centered, indentation should be used
– Section Headings: Not numbered, 12 pt. Times New Roman, bold, centered; one blank line above
– Section Sub-headings: Numbered, 12 pt. Times New Roman, bold, italic, centered; one blank line above
– Regular text: 12 pt. Times New Roman, one and a half space,full justified, indentation should be used in each paragraph

Title page information

The following information should be placed at the first page:

Title

Concise and informative. If possible, authors should not use abbreviations and formulae.

Authors and affiliations

Author/authors' names should be presented below the title. The authors' affiliation addresses (department or college; university or company; city, state and zip code, country) should be placed below the names. Authors with the same affiliation must be grouped together on the same line with affiliation information following in a single block. Authors should indicate all affiliations with a lower-case superscript letter immediately after the author's name and in front of the appropriate address.

Corresponding author

It should be clearly indicated who will handle correspondence at all stages of refereeing and publication, also post-publication process. The e-mail address should be provided (footer, first page). Contact details must be kept up to date by the corresponding author.

Abstract

The abstract should have up to 100-150 words in length. A concise abstract is required. The abstract should state briefly the aim of the research, the principal results and major conclusions. Abstract must be able to stand alone. Only abbreviations firmly established in the field may be eligible. Non-standard or uncommon abbreviations should be avoided, but if essential they must be defined at their first mention in the abstract itself.

Keywords

Immediately after the abstract, author/authors should provide a maximum of 6 keywords avoiding general, plural terms and multiple concepts (avoid, for example, 'and', 'of'). Author/authors should be sparing with abbreviations: only abbreviations firmly established in the field may be eligible.

Abbreviations

Author/authors should define abbreviations that are not standard in this field. Abbreviations must be defined at their first mention there. Author/authors should ensure consistency of abbreviations throughout the article.

Units

All units used in the paper should be consistent with the SI system of measurement. If other units are mentioned, author/authors should give their equivalent in SI.

Introduction

Literature sources should be appropriately selected and cited. A literature review should discuss published information in a particular subject area. Introduction should identify, describe and analyze related research that has already been done and summarize the state of art in the topic area. Author/authors should state clearly the objectives of the work and provide an adequate background.

Material and Methods

Author/authors should provide sufficient details to allow the work to be reproduced by other researchers. Methods already published should be indicated by a reference. A theory should extend, not repeat, the background to the article already dealt within the Introduction and lay the foundation for further work. Calculations should represent a practical development from a theoretical basis.

Results and Discussion

Results should be clear and concise. Discussion should explore the significance of the results of the work, not repeat them. A combined Results and Discussion section is often appropriate.

Conclusions

The main conclusions of the study may be presented in a Conclusions section, which may stand alone or form a subsection of a Results and Discussion section.

Acknowledgements

Author/authors should include acknowledgements in a separate section at the end of the manuscript before the references. Author/authors should not include them on the title page, as a footnote to the title or otherwise. Individuals who provided help during the research study should be listed in this section.

Artwork

General points

– Make sure you use uniform lettering and sizing of your original artwork
– Embed the used fonts if the application provides that option
– Aim to use the following fonts in your illustrations: Arial, Courier, Times New Roman, Symbol
– Number equations, tables and figures according to their sequence in the text
– Size the illustrations close to the desired dimensions of the printed version

Formats

If your electronic artwork is created in a Microsoft Office application (Word, PowerPoint, Excel) then please supply 'as is' in the native document format

Regardless of the application used other than Microsoft Office, when your electronic artwork is finalized, please 'Save as' or convert the images to one of the following formats (note the resolution requirements given below):

EPS (or PDF): Vector drawings, embed all used fonts

JPEG: Color or grayscale photographs (halftones), keep to a minimum of 300 dpi

JPEG: Bitmapped (pure black & white pixels) line drawings, keep to a minimum of 1000 dpi or combinations bitmapped line/half-tone (color or grayscale), keep to a minimum of 500 dpi

Please do not:

– Supply files that are optimized for screen use (e.g., GIF, BMP, PICT, WPG); these typically have a low number of pixels and limited set of colors
– Supply files that are too low in resolution
– Submit graphics that are disproportionately large for the content

Color artwork

Author/authors should make sure that artwork files are in an acceptable format (JPEG, EPS PDF, or MS Office files) and with the correct resolution. If, together with manuscript, author/authors submit color figures then Technical Sciences will ensure that these figures will appear in color on the web as well as in the printed version at no additional charge.

Tables, figures, and equations

Tables, figures, and equations/formulae should be identified and numbered consecutively in accordance with their appearance in the text.

Equations/mathematical and physical formulae should be presented in the main text, while tables and figures should be presented at the end of file (after References section). Mathematical and physical formulae should be presented in the MS Word formula editor.

All types of figures can be black/white or color. Author/authors should ensure that each figure is numbered and has a caption. A caption should be placed below the figure. Figure must be able to stand alone (explanation of all symbols and abbreviations used in figure is required). Units must be always included. It is noted that figure and table numbering should be independent.

Tables should be numbered consecutively in accordance with their appearance in the text. Table caption should be placed above the table. Footnotes to tables should be placed below the table body and indicated with superscript lowercase letters. Vertical rules should be avoided. Author/authors should ensure that the data presented in tables do not duplicate results described in figures, diagrams, schemes, etc. Table must be able to stand alone (explanation of all symbols and abbreviations used in table is required). Units must be always included. As above, figure and table numbering should be independent.

References

References: All publications cited in the text should be presented in a list of references following the text of the manuscript. The manuscript should be carefully checked to ensure that the spelling of authors' names and dates of publications are exactly the same in the text as in the reference list. Authors should ensure that each reference cited in the text is also present in the reference list (and vice versa).

Citations may be made directly (or parenthetically). All citations in the text should refer to:

1. Single author

The author's name (without initials, with caps, unless there is ambiguity) and the year of publication should appear in the text

2. Two authors

Both authors' names (without initials, with caps) and the year of publication should appear in the text

3. Three or more authors

First author's name followed by et al. and the year of publication should appear in the text

Groups of references should be listed first alphabetically, then chronologically.

Examples:

"... have been reported recently (ALLAN, 1996a, 1996b, 1999; ALLAN and JONES, 1995). KRAMER et al. (2000) have recently shown..."

The list of references should be arranged alphabetically by authors' names, then further sorted chronologically if necessary. More than once reference from the same author(s) in the same year must be identified by the letters "a", "b", "c" etc., placed after the year of publication.

References should be given in the following form:

KUMBHAR B.K., AGARVAL R.S., DAS K. 1981. Thermal properties of fresh and frozen fish. International Journal of Refrigeration, 4(3), 143–146.

MACHADO M.F., OLIVEIRA F.A.R., GEKAS V. 1997. Modelling water uptake and soluble solids losses by puffed breakfast cereal immersed in water or milk. In Proceedings of the Seventh International Congress on Engineering and Food, Brighton, UK.

NETER J., KUTNER M.H., NACHTSCHEIM C.J., WASSERMAN W. 1966. Applied linear statistical models (4th ed., pp. 1289–1293). Irwin, Chicago.

THOMSON F.M. 1984. Storage of particulate solids. In M. E. Fayed, L. Otten (Eds.), Handbook of Powder Science and Technology (pp. 365–463). Van Nostrand Reinhold, New York.

Citation of a reference as 'in press' implies that the item has been accepted for publication.

Note that the full names of Journals should appear in reference list.

Submission checklist

The following list will be useful during the final checking of an article prior to the submission. Before sending the manuscript to the Journal for review, author/authors should ensure that the following items are present:

– Text is prepared with a word processor and saved in DOC or DOCX file (MS Office). One author has been designated as the corresponding author with contact details: e-mail address
– Manuscript has been 'spell-checked' and 'grammar-checked'
– References are in the correct format for this Journal
– All references mentioned in the Reference list are cited in the text, and vice versa
– Author/authors does/do not supply files that are too low in resolution
– Author/authors does/do not submit graphics that are disproportionately large for the content